Texas A&M University
J. Mike Walker'66 Department of Mechanical Engineering
Turbomachinery Laboratory
Tribology Group

MEASUREMENTS OF THE DYNAMIC FORCED RESPONSE OF AN O-RINGS SEALED SQUEEZE FILM DAMPER SUPPLIED WITH A LOW SUPPLY PRESSURE

Annual Progress Report to the TAMU Turbomachinery Research Consortium

TRC-SFD-01-22

by

Bryan Rodríguez
Graduate Research Assistant

Luis San Andrés
Mast-Childs Chair Professor
Principal Investigator

June 2022

EXPERIMENTS WITH SEALED ENDS SQUEEZE FILM DAMPER & CHECK VALVE
TRC Project funded in 2019
TEES #28-258124-00136

EXECUTIVE SUMMARY

Modern SFD designs are short in axial length to limit weight and part count and supplied with a low lubricant feed pressure to reduce operating costs related to lubricant storage and pumping power. O-rings (ORs) reduce lubricant side leakage, increasing the viscous damping within a constrained physical space and provide a modest centering support stiffness to the rotor. Continuing a long-term project characterizing SFDs for air breathing engines, the work details comprehensive measurements of the forced performance of an OR sealed damper (OR-SFD), with a film land length L=25.4 mm, 127 mm in diameter (D), and a radial clearance c=0.279 mm. The damper, with a slenderness ratio L/D = 0.2. undergoes centered whirl motions with amplitudes r=0.05c to 0.45c, over ω = 10 Hz to 130 Hz (max. squeeze film velocity v_s=$r\omega$=102.5 mm/s). Lubricant ISO VG 2 supplied at 0.69 bar(g) fills an upstream oil plenum and flows through a single orifice with a check valve midway of the damper length (1/2L). Measurements of dynamic loads, along with the ensuing displacements and accelerations identify the parameters of the test structure, ORs and SFD. This research effort is the first to identify ORs force coefficients over a range of orbit amplitudes and assess its effects on the dynamic performance of the OR-SFD. The ORs force coefficients remain nearly invariant within the identification frequency range; however, they showcase significant orbit amplitude dependence. At r/c = 0.05 the OR centering stiffness (K_{OR}) doubles the static stiffness ($K_{OR,static}$), and as $r/c \rightarrow$ 0.45, K_{OR} approaches ½$K_{OR,static,}$ likely due to the extensive elastic deformation and slow recovery in the rings' polymeric structure bonds. At r=0.05c and 0.10c, the ORs viscous damping coefficient (C_{OR}) contributes to ~10% of the total in the lubricated system (C_L), while for $r/c >$ 0.25, it contributes to just 3% of C_L. For small orbit amplitudes ($r \leq$ 0.25c), the experimental SFD added mass (M_{SFD}) and viscous damping (C_{SFD}) coefficients are nearly equivalent to theoretical magnitudes for a fully sealed damper (no side leakage). However, as the orbit size grows to $r \rightarrow$ 0.45c, M_{SFD} drops nearly 75% and C_{OR} decreases

by ~40%. The reduction in force coefficients is due to the onset of both lubricant cavitation and air ingestion occurring for $v_s \geq 24.5$ mm/s. A prediction model delivers squeeze film added mass and viscous damping coefficients which are on average, 10% larger than those derived experimentally. Measured film dynamic pressures evidence both oil vapor cavitation and air ingestion, and video recordings depict a bubbly mixture in the lubricant return line and through the damper top end. Peak-peak film pressures for operation at $v_s \geq 34$ mm/s show the gas content prevents the generation of peak pressures proportional to v_s. Moreover, pk-pk pressures inside the journal oil delivery plenum follow the same trend as those in the film land, showing the mechanical check valve installed in the journal allows for lubricant backflow. A novel approach enables the estimation of the gas volume fraction (GVF), which rapidly increases with v_s. The simple procedure draws into a deflated balloon the material contents in the film, weighs the sample and identifies its volume to produce an estimation of the GVF. The research findings reveal more details on the effect of ORs to the forced performance of a damper and their limited ability to prevent air ingestion when operating at large squeeze velocities and a low lubricant feed pressure.

TABLE OF CONTENTS

NOMENCLATURE

c	Damper radial clearance [m]
$C_{\alpha,\beta,\ (\alpha,\beta= X,Y)}$	Damping coefficient [N-s/m]
C_{st}	Support structure damping coefficient [N-s/m]
C_{SFD}	SFD damping coefficient [N-s/m]
C_{st+OR}	Support structure damping coefficient with O-rings installed [N-s/m]
C^*	Theoretical SFD damping coefficient [N-s/m]
d	OR inner diameter [mm]
D	Journal diameter [m]
f	Excitation frequency [Hz]
f_n	Test system natural frequency [Hz]
H	$H=(K-\omega^2 M) + i(\omega C)$. Complex dynamic stiffness [N/m], $i=\sqrt{-1}$
h	Film thickness
$K_{\alpha,\beta,\ (\alpha,\beta= X,Y)}$	Stiffness coefficient [N/m]
K_{static}	Static stiffness coefficient [N/m]
$K_{\perp}$	OR quadrature stiffness [N/m]
K_{st}	Support structure stiffness coefficient [N/m]
K_{st+OR}	Support structure stiffness with O-rings installed [N/m]
L	Film axial length [m]
$M_{\alpha,\beta,\ (\alpha,\beta= X,Y)}$	Added mass coefficients [kg]
M_{BC}	Mass of bearing cartridge [kg]
M_{SFD}	SFD added mass coefficient [kg]
M_{st}	Structure remnant mass coefficient [kg]
M^*	Theoretical SFD added mass term [kg]
η	O-ring loss factor [-]
P	Fluid film dynamic pressure [bar]
P_S	Supply pressure [bar]
Q_S	Supply flowrate [LPM]
r	Orbit radius [m]
Re_S	$\rho\omega c^2/\mu$ Squeeze film Reynolds number [-]
t	O-Ring thickness [mm]
U	Uncertainty in the measurements [%]
V	Volume [m^3]
v_s	$r\omega$. Squeeze film velocity [m/s]
X, Y	Cartesian coordinate system
z	Axial coordinate [m]
θ	Circumferential coordinate [rad]

μ	Lubricant viscosity [mPa-s]
ρ	Lubricant density [kg/m^3]
ϕ_{in}	Feedhole orifice diameter [m]
ω	Whirl frequency [rad/s]
ζ_{st}	Support structure (dry) damping ratio [-]

VECTORS AND MATRICES

a	Vector of absolute acceleration [m/s^2]
C	Matrix of damping coefficients [N-s/m]
F	Vector of force [N]
H	Matrix of complex dynamic stiffnesses [N/m]
K	Matrix of stiffness coefficients [N/m]
M	Matrix of added mass coefficients [kg]
z	Vector of BC displacements relative to journal [m]

SUBSCRIPTS

L	Lubricated
SFD	Squeeze film damper
st	Support structure
st+OR	Structure with ORs installed

ABBREVIATIONS

BC	Bearing cartridge
CCO	Circular Centered Orbit
CCW	Counterclockwise
CV	Coefficient of Variation
CW	Clockwise
GVF	Gas Volume Fraction
ID	Inner diameter
OR	O-ring seal
OD	Outer diameter
PR	Piston Ring seal

LIST OF FIGURES

LIST OF TABLES

CHAPTER I
INTRODUCTION

Rotor-bearing systems employ squeeze film dampers (SFDs) to reduce rotor synchronous motions and aid to suppress rotordynamic instabilities. Oftentimes, SFDs installed with an elastic structural support element, are employed to adjust the location of system critical speeds and isolate a rotor from its stator or casing [1,2]. Gas turbines in aircraft engines rely on SFDs in series with rolling element bearings to safely traverse several critical speeds, secure stable operation at cruise speed, and to harmlessly endure maneuver load conditions [1]. Short length SFDs, with a slenderness ratio $L/D \leq 0.2$, are common in gas turbines to minimize weight and space.

Figure 1 presents a schematic view of a sealed ends SFD in series with a rolling element bearing supported rotor. The rotor connects to the ball bearing inner race, and the annular gap between the ball bearing outer diameter and the bearing cartridge (BC) hosts a lubricant film continuously supplied through a feedhole. Either an elastic centering support, such as a squirrel cage or an anti-rotation pin (dowel pin) prevent rotation of the ball bearing outer race. The rotor and ball bearing whirl (or precess) in response to applied forces and squeeze the lubricant film within the small clearance. The journal performs circular centered orbits of radius r and whirl frequency ω, thus generating a pressure field that produces reaction forces characterized by both damping (C) and inertia (M) force coefficients [1].

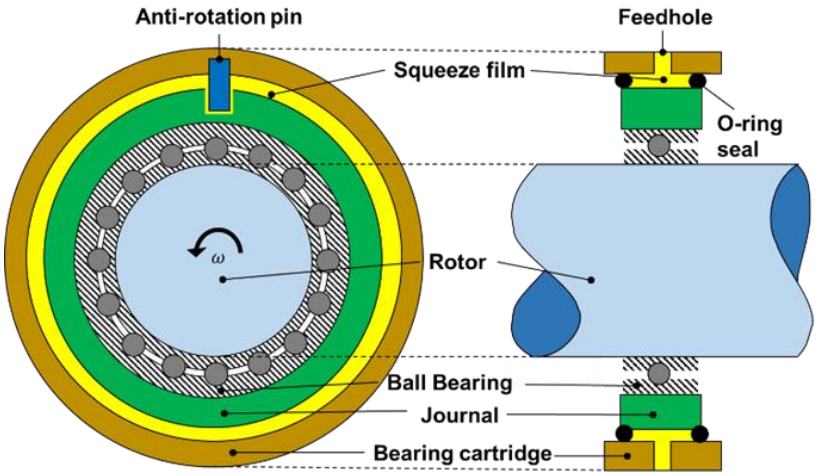

Figure 1. Schematic views (not to scale) of a one-hole-fed SFD with O-rings sealed ends. Graph adapted from an original rendition in Ref. [1].

Sealing devices, such as O-rings (ORs) and piston rings (PRs) represent a cost-effective means to reduce the lubricant supply and side leakage, while amplifying damping in SFDs amidst a limited axial length. For instance, O-rings are off-the-shelf seals that also add viscoelastic (material) damping to rotor-bearing systems [3]; and when designed properly, act as a stiffness in SFDs. However, the elastomeric rings do have limitations reducing their applicability. In general, ORs are sensitive to high and low temperatures, as their typical maximum service temperature is only 120^{o}C [3]. Moreover, this seal type deteriorates quickly when operating outside designated service conditions, and its dynamic forced performance depends on a number of factors, such as frequency, temperature, amplitude of motion and material type [3].

On the other hand, (metal) piston rings (PRs) withstand a broader operating temperature range; however, their abutted ends (slits) allow for substantial lubricant side leakage. While PRs are suitable sealing elements in SFDs for commercial aircraft engines [4], Nitrile ORs are employed in land-based turbomachinery, such as in compressors and steam turbines [5,6]. Experimental identification of force coefficients in a rotor-bearing system, namely stiffness, damping and mass,

is vital to validate SFD mechanical performance and reliability operating under both design and extreme conditions [7].

The following literature review comprises two sections. The first section summarizes up-to-the-minute experimental efforts quantifying the dynamic force response of elastomeric O-ring applicable to high performance turbomachinery systems over a span of nearly fifty years. Likewise, the second section briefly recounts landmark research efforts in the development of SFDs, accompanied by experimental results of the dynamic forced response of OR sealed SFDs since the mid 1970's to date.

CHAPTER II
LITERATURE REVIEW

Dynamic Forced Performance of O-Rings for turbomachinery systems

O-rings are circular cross-section rings typically molded from an elastomer, such as Nitrile Butadiene Rubber (NBR or Buna-N) or Fluorocarbon (Viton), primarily used for static sealing [3]. The O-ring seal assembly consists of a compressed elastomer OR and a gland. The gland constitutes the space that hosts an OR, usually a groove cut between a bore and a piston or rod. Advantages in the use of ORs as seals include their low cost, low space and weight, durability, and easily identifiable failure [3]. O-rings have a broad range of industrial applications and solutions.

O-rings are attractive means to provide a centering stiffness to SFDs installed in lightweight rotor-bearing systems, as detailed in Refs. [5, 6, 8-11]. Moreover, ORs are ubiquitous in micro turbomachinery (MTM)[1] systems due to their ability to reduce rotor synchronous motions and self-induced rotor whirl instabilities, as seen in Refs. [12-14].

An increase in the use of ORs and other viscoelastic materials to solve vibration problems prompted Nashif et al., Sun and Lu, and Ginsberg in Refs. [15-17] (among many others) to develop mathematical models describing the dynamic characteristics of ORs and other viscoelastic materials. In the case of O-rings, the energy they dissipate comes from time of relaxation and recovery (stress and strain) upon deformation in their inner polymeric structures. Measurements of harmonic stress (σ_0) and strain (ε_0) produce a complex modulus (E^*) equal to $\sigma_0 = E^* \varepsilon_0 = (E' + iE'')$, where E' *and* E'' are the storage and loss moduli, respectively, and i is the imaginary unit. Consequently, a loss factor (η) is defined as $\eta = E''/E'$ and the complex modulus becomes $E^* = E'(1+i\,\eta)$ [16]. Conversely, load and displacement measurements due to harmonic

[1] MTM rotor-bearing systems encompass a power output of 250 kW or less.

motion produce a complex dynamic stiffness $K_{OR}(1+i\eta)$. Both the complex modulus and dynamic stiffness determine analytical expressions as a function of frequency, and other factors that directly affect material motion over a particular frequency range [15].

Alternately, in a viscous damping model, a damping coefficient (C) produces a reaction force linearly proportional to the magnitude of velocity and in the opposite direction to the motion [16]. However, this is not the case for material damping characterized with $K_{OR}(1+i\eta)$, where the amount of energy dissipated per cycle is mainly a function of the amplitude of strain [15].

In 1978, Smalley et al. [18] first report OR stiffness and damping coefficients as a function of frequency and seven controlled experimental parameters. These include material, ring thickness, amplitude of motion, temperature, squeeze, stretch[2] and groove width. The authors exert dynamic load tests on elastomeric ORs over a (base) excitation frequency range (f) from 70 Hz to 1000 Hz. The study produces empirically derived non-linear curve fits to predict OR stiffness (K_{OR}) and a loss factor η. Experimental results show the OR stiffness decreases by 30% when the amplitude of motion increases 3.5 times. However, the effect of amplitude of motion on the loss factor η is less substantial. As the amplitude of motion increases nearly 17 times, η only drops by 60%. For the rest of the experimental conditions, such as stretch and ring thickness, the authors find no significant effect on the dynamic performance of the elastomeric seals.

Continuing with the work conducted in Ref. [18], Green and Etsion [19], in 1986, identify the effect of pressure and squeeze on ORs force coefficients. The base load experiments employ Buna N and Viton ORs at three different gas supply pressures and O-ring squeeze levels. The test results in Ref. [19] show the Viton ORs provide up to three times more stiffness and nearly five times more damping than their Buna N counterparts. The authors remark a pronounced effect due to

[2] The OR stretch comprises the difference between the groove diameter minus the OR inner diameter, divided by the OR inner diameter [3].

squeeze and pressure, since the highest magnitudes of both stiffness and damping increase threefold, compared to the coefficients identified with the lowest squeeze and pressure levels. The experimental results demonstrate the importance of identifying and controlling operating conditions that could significantly affect the ORs dynamic force performance.

In 1994, Aktrük and Gohar [20] identify dynamic force coefficients of a rolling element bearing-rotor system supported on pairs of Viton ORs. The experiments contemplate unbalance response measurements of a rotating system. The experimental results show the damping from the ORs considerably reduces the system amplification factor (AF) by ~ 6.5 times. Additionally, the use of the soft elastomeric supports decreases the system first critical speed by 45%, thus showing ORs may be used to adjust the location of the system critical speed. Furthermore, the authors in Ref. [20] warn that improper characterization of the elastomeric seals could lead to larger synchronous amplitudes of motion or system failure.

In practice, O-ring manufacturers [3] assign a range of operating conditions, that if not followed, diminish OR useful life, impair sealing and increase the probability of a sudden failure. For example, extended operation at high temperature, improper gland design, or the introduction of an incompatible fluid are major causes of a type of seal permanent deformation known as compression set [3]. Moreover, OR extrusion is present in dynamic applications if the seals encounter excessive pressure, an excessive shaft eccentricity, or improper gland machining. Worse yet, inappropriate installation or lubrication, or an uneven gland surface finish could provoke a spiral type failure distorting the O-ring shape.

O-ring manufacturers provide extensive guidance in handbooks, see Refs. [3, 21, 22], on the use, design, diagnostic of failure and maintenance of elastomeric O-rings under static sealing conditions. Likewise, there are many design recommendations and empirical formulas for the use

of ORs in dynamic applications. However, these handbooks provide little to no information on the dynamic forced performance of ORs, and do not report force coefficients, such as, stiffness and damping, or loss factor.

Ref. [20] was published in 1994 by Aktrük, and Gohar, and 14 years later; Belforte et al. [23], in 2008, experimentally identify the threshold speed of instability of an air-bearing rotor system supported by Buna N, Viton and silicone O-rings. The authors estimate OR stiffness and viscous damping coefficients over a frequency range from 300 Hz to 800 Hz and demonstrate the Viton O-rings produce the largest damping magnitudes, compared to their Buna N and silicone counterparts.

Also in 2008, Tomioka and Miyanaga [24] identify experimentally and analytically the onset speed of instability of a rotor mounted on a pair of herringbone gas bearings and in series supported with OR seals. Experiments without rotor speed first identify OR stiffness and viscous damping coefficients by producing base excitation loads. Next, linear and nonlinear OR force coefficients predict the system onset speed of instability. The predictions delivered using nonlinear OR coefficients lie within 2% of those found experimentally, whereas the predictions with linear OR coefficients vary by ~15%. The large discrepancies between experiments and predictions using linear coefficients demonstrates the importance of proper identification (and modeling) of OR dynamic force response in rotor-bearing systems.

Expanding the work detailed in Ref. [23], in 2017 Al-Bender et al. [25] identify stiffness (K_{OR}) and viscous damping (C_{OR}) coefficients of both Viton and Kalrez®[3] ORs with different diameters, thicknesses and squeeze levels. The authors conduct small amplitude of motion (2.5 μm) base excitations to identify K_{OR} and C_{OR} coefficients, and produce force coefficient models as a function

[3] The authors in Ref. [23] describe Kalrez® as the proprietary name of a perfluoroelastomer material.

of material hardness, squeeze, diameter and OR thickness. Ref. [25] shows the Viton ORs have the largest damping magnitudes, mainly due to their high Shore A[4] hardness, and also confirms the findings reported in Refs. [23, 19]. The models produced in Ref. [25] serve as an approximation of stiffness and damping of ORs of general size and to evaluate the rotordynamic stability of gas bearing systems employing ORs.

In 2018, Shoyama and Fujimoto [26] estimate stiffness (K_{OR}) and viscous damping (C_{OR}) coefficients of Buna-N O-rings of different sizes and squeeze levels using the same identification method as in Ref. [24]. The experimental results show slight increments in both K_{OR} and C_{OR} with OR diameter and frequency. Later, the authors present a complex shear modulus G, and produce predictions of K_{OR} and C_{OR} as a function of frequency, squeeze and ring thickness. The agreement of predictions with experimental results lead the authors to conclude that the deformation dependent high-frequency viscoelastic characteristics of NBR ORs can be modeled as a function of preload ratios due to OR squeeze and thickness.

In 2019, Bättig and Schiffmann [27] identify stiffness (K_{OR}) and viscous damping (C_{OR}) coefficients for ORs with distinct Shore hardness magnitudes and squeeze levels for their use in gas bearing-rotor systems. The experimental apparatus and identification procedure are based on those described in Ref. [18], exerting unidirectional amplitudes of motion equal to 0.5 μm and over a frequency range from 1.5 to 3,500 Hz. Analysis of the experimental results agrees with those presented in Refs. [23, 24], that show ORs with a Shore hardness significantly increase both stiffness and damping coefficients.

Table 1 summarizes relevant operating conditions and ring characteristics from the present review. Experimental identification of OR force coefficients represents a milestone towards their

[4] The Shore (A) durometer scale is the standard instrument to measure hardness in most rubber compounds [3]

reliable implementation, particularly in oil-free MTM applications. However, many of the reviewed experimental results are not applicable to other turbomachinery systems, such as O-rings sealed SFDs. First, the experimental frequency range in current research efforts are at least an order of magnitude larger than those in OR-SFDs. Actual OR-SFDs operate within a frequency up to 200 Hz, for example, see Refs. [5, 9, 10]. Likewise, Refs. [25-27] demonstrate the OR amplitudes of motion in the experiments extend to just a few microns, while OR-SFDs sustain whirl orbits in the range of r=13 μm to 125μm.

Table 1. Relevant experimental conditions of research efforts characterizing the dynamic forced performance of O-rings.

Ref. #	First Author Last Name	Year	Frequency Range [Hz]	*D* [mm]	Mean OR thickness (*t*)[mm]	*D/t* [-]	Amplitude of motion [μm]	Material
[18]	Smalley	1978	50-1,000	76.2	3.6	3.2	25.4-127.0	Buna N, Viton
[19]	Green	1986	10-300	76.2	3.6	3.2	10.0	Buna N, Viton
[20]	Aktrük	1994	100-1,000	68.0			8.0	Viton
[23]	Belforte	2008	166-1,250	37.0	1.8	20.8	1.0-6.0	Buna N, Viton, Silicone
[24]	Tomioka	2008	0.5-4,000	11.0	2.4	4.6	-	Buna N
[25]	Al-Bender	2017	40-1,000	26.0	2.2	11.8	2.5	Viton
[26]	Shoyama	2018	1,500-4,000	17.0	1.5	11.3	1.5-2.0	Buna N
[27]	Battig	2019	1.5-3,750	16.0	2.0	8.0	0.5	Buna-N
Current	Rodríguez	2021	10 -120	126.0	3.5	30.5	0-125.0	Buna N

Background on SFDs

The earliest versions of a SFD date back to 1889, when C. A. Parsions [28] employed a number of concentric sleeves separated by a radial gap filled with lubricant to provide damping to the rotor installed in the first steam turbine. Already in the 20th century, in 1933 and 1948, Birmann [29, 30] patented concepts of SFDs for their use in steam turbines and compressors. Next, in 1963, Cooper [31] presented the first experimental investigation of a SFD in an aircraft gas turbine to ameliorate rotordynamic instabilities. By the 1970's, SFDs were commonly employed in gas turbines, centrifugal compressors, and semi-floating ring bearings in turbochargers. A milestone two-part paper, by Della Pietra and Adiletta in 2002, [32, 33] summarize forty years of vast research (experimental and analytical) on SFDs since their inception.

A SFD is not a ready-made mechanical element, because its design and operating conditions must suit a particular rotor-bearing system. If damping is too large, the SFD may lock and transmit large forces to its support structure [1]. Conversely, if damping is too low, the damper becomes ineffective, thus permitting large amplitudes of motion [1]. Additionally, for the damper to be functional, the location and flexibility of its structural support element must be sufficient to allow rotor motion in the modes of vibration of interest.

To advance aircraft gas turbine engine design, a gas engine manufacturer funds an extensive research effort at the Turbomachinery Laboratory of Texas A&M in 2008. The experimental campaign characterized the forced response of novel SFD configurations and operating conditions implemented in aircraft jet engines. The program included a variety of lubricant supply pressures and damper clearances, with ends open to ambient or sealed with either PRs or ORs. In 2016, San Andrés et al. [34] summarize the decade-long effort and showcase benchmark experimental data, ready for integration to standard engineering practice.

Parameter Identification of OR Sealed SFDs

Pioneer experimental results in the 1970's detailed in Refs. [35, 36, 8] quantify large amplitude squeeze film radial forces from operation at whirl orbits over a range of frequencies (ω). In the experiments, OR seals prevent lubricant side leakage and an axial pressure gradient, and sufficiently high lubricant supply pressures (up to 5.5 barg) reduce the incidence of oil cavitation in the damper film land. Alas, the authors disregard fluid inertial effects, leading to large discrepancies between theory and practice. Furthermore, the contribution of the OR seals to the test system reaction forces are also omitted.

Two decades later, in 1995 [9] Leader et al. implement an OR-SFD in series with a tilting pad journal bearing (TPJB) to diminish large amplitudes of rotor synchronous motion in a multistage steam turbine. First, static load tests establish an equivalent OR stiffness that provides a soft centering support to the rotor. Next, rotor mass unbalance displacement measurements estimate damping coefficients, and demonstrate the OR-SFD diminishes the system AF by nearly 3.5 times.

In 1996, Kuzdzal and Hustak [37] present experimental results comparing the performance of several SFD configurations with different centering support mechanisms, and five distinct OR configurations in a test rotor representative of a ten-stage centrifugal compressor. The authors estimate OR stiffness coefficients with static load tests, and squeeze film damping terms from displacement measurements of rotor synchronous unbalance response. Experimental results demonstrate that both mechanical spring and OR centered dampers suppress whirl motions, synchronous and subsynchronous, thus outperforming the eccentric centering spring mechanisms.

In the same year, Zeidan et al. [38] review 25 years of SFD experimental data and numerical predictions applied to high performance turbomachinery. The authors showcase OR supported dampers for their simple design and inherent resilience to provide a centering stiffness within a

limited axial length. Ref. [38] emphasizes the importance of fluid inertia effects which may introduce added mass coefficients and dramatically change the dynamic forced response of rotor SFD systems.

In 1999, Jei et al. [39] present a novel damper design for high-speed, lightweight turbomachines. Six sets of leaf springs positioned around an inner ring provide a centering support to the structure, and two side covers sealed with ORs contain the lubricant in the damper housing. Relative motion of the inner ring squeezes the lubricant against the bearing housing and displaces the spring structures to provide both viscous and friction damping to the system.

Unbalance response rotordynamic measurements with both a dry (unlubricated) and lubricated test structure serve to identify the system force coefficients. The experiments reveal a constant stiffness magnitude for both the dry and lubricated systems denoting a nil added mass term in the squeeze film, and damping terms that quickly decay with an increase in whirl frequency. Interestingly, the system damping arises mainly due to friction from the springs sliding against the damper inner ring and the ORs sliding against their sealing covers.

In 2006, Kanki et al. [40] present an experimental investigation of an OR-sealed SFD installed in a brake system of an electrical passenger train presenting large acceleration amplitudes and noise levels. With the damper installed in the brake mechanism, a series of deceleration experiments identifies the dry (unlubricated) equivalent stiffness that demonstrates a drop the system natural frequency by 75%. Next, experiments with a lubricated system identify the system damping ratio and maximum pressure noise levels. Measurements with a lubricated damper show a dramatic decrease in the magnitude of acceleration, 20 times lower than the original measurements. Likewise, the peak noise level, decreases by nearly 1.5 times compared to the

measurements without the damper installed, thus demonstrating the wide applicability and effectiveness of a sealed SFD.

In 2008, Kim et al. [41] introduce a sealed SFD fed with a magnetorheological (MR) lubricant engineered to increase its viscosity by applying an electric current. First, the paper describes the experimental facility and the magnetic field circuit designed to uniformly deliver an electric current to the MR fluid. Next, to contain the lubricant within the damper film land, the authors detail the design process of a pair of silicone bellows-shaped seals replacing ORs. Whirl orbit load measurements with an unlubricated system show the peak reaction force from the silicone seals only represents 2.4% of the total force measured with ORs.

The authors conduct a series of periodic loads with a lubricated system over a range of excitation frequencies and applied electrical currents to identify the damper force coefficients. The experimental results show the magnitude of the added mass (M_{SFD}) and damping (C_{SFD}) coefficients decrease with an increasing orbit radius. Additionally, the authors identify the onset of nonlinear SFD response at the largest applied electrical current in the form of hysteresis reaction force loops due to the MR lubricant.

In 2010, Memmot [42], representing an original equipment manufacturer (OEM), distinguishes the prevalence of OR-SFDs in turbomachinery systems and recounts the production of 460 lightweight rotor (~400 kg) compressors by the author's company. Furthermore, the use of mechanical arc springs in an OR-SFD enable their use in an additional 400 compressors with large rotors (~6000 kg) by the date of publication. The mechanical springs typically produce a centering support stiffness one order of magnitude greater than that of the ORs, thus allowing for permissible OR squeeze levels.

In 2018, Shoyama and Fujimoto [43] identify force coefficients of four double clearance squeeze film dampers (DCSFDs) along with two single clearance squeeze film dampers (SCSFDs). The O-ring supported dampers, designed for their implementation in a water-lubricated compressor, feature a cylindrical (floating) ring to provide a double clearance. Experimental results from unidirectional load tests over a frequency range from 200 Hz to 1,600 Hz with a dry (unlubricated) system show that both magnitudes of OR stiffness (K_{OR}) and damping (C_{OR}) steadily increase with frequency. Next, squeeze film experimental damping coefficients (C_{SFD}) increase with frequency and then decrease for operation at frequencies higher than ~1,100 Hz. Overall, damping coefficients in the DCSFDs are four times larger than those produced with SCSFDs for the same amount of total clearance.

Stemmed from the research program in Ref. [34], San Andrés and Koo in 2018 [44] and in 2019 [45] compare a piston ring sealed (PR-SFD) with an OR-SFD, supplied with a range of lubricant pressures either through one or three equally spaced feedholes. Ref. [44] demonstrates the elastomeric seals produce an increase in the system structure stiffness by 20%, while the identified OR damping coefficients are not viscous, but rather of structural type. Experiments in both Refs. [44, 45] with orbit radii ranging from r/c=0.05 to 0.15, and 0.30, reveal that the OR-SFD produces 20% more damping than the PR-SFD, mainly due to lubricant leakage and air ingestion through the PRs. In actuality, the OR-SFD offers an additional 10% damping due to the addition of the elastomeric damping from the seals.

In the same year (2020), Li et al. [10] introduce a double-ended beam design spring to provide a centering stiffness to an O-rings sealed SFD. In an accompanying paper [11], the authors show that the springs provide ~60% of the damper total structure static stiffness, while the elastomeric rings provide the remaining 40%. Next, supported by two tilting pad journal bearings (TPJB), a

series of unbalance load tests identify the rotor-bearing system synchronous response. Finally, with two OR-SFDs in place, experimental results demonstrate the damper forces are too high, making the system overly stiff, a condition which could deteriorate the rotor-bearing system.

In 2021, San Andrés and Rodríguez [46] detail measurements of a short length (L/D = 0.2) OR-SFD. Lubricant supplied at 0.7 bar(g) flows through a single feedhole into the midplane of the damper film land. Dynamic loads produce circular centered orbits with radius r/c= 0.10, 0.15 and 0.20 to deliver force coefficients representing O-rings and the SFD. One set of dynamic loads without lubricant supplied identify ORs force coefficients and show a direct stiffness (K_{OR}) with magnitude nearly half of the test apparatus structural stiffness. The ORs also reveal a quadrature stiffness $K_{\perp}$, indicative of a significant material loss factor as $\omega \rightarrow 0$. Measurements with a lubricated system demonstrate nearly constant damping and mass coefficients that agree reasonably well with a prediction model developed in Ref. [47].

From the literature reviewed, Table 2 summarizes the operating conditions characterizing OR-SFD force response in the research efforts described, such as damper clearance, slenderness ratio (L/D), journal whirl frequency range, lubricant type and supply pressure. Overall, the experimental efforts present a thorough investigation of the dynamic force performance of SFDs sealed with ORs. However, persistent industry needs seek to achieve higher efficiency turbomachines with reduced operating costs and a low environmental footprint. For instance, certain engine manufacturers employ sealed ends dampers and operate them along with a low lubricant supply pressure (P_S < 1 barg) to reduce lubricant storage volume and pumping energy costs. Furthermore, many of the research efforts reviewed to date simply neglect OR force coefficients (i.e., stiffness and damping), or deliver (constant) OR dynamic parameters for a wide range of damper operating conditions.

Table 2. Relevant experimental conditions of research efforts characterizing OR-SFD dynamic forced performance.

Ref. #	First Author Last Name	Year	Frequency Range [Hz]	Lubricant Type	Viscosity @ testing temperature [cP]	Supply Pressure [barg]	L/D [-]	Mean *c* [mm]	*r/c* [-]
[37]	Vance	1974	30	SAE 10, 50	40.0, 360.0	3.10	0.96	1.570	0.25-0.75
[38]	Feder	1978	17	-	144.0	5.50	0.31	0.508	0.20-0.62
[8]	Marmol	1978	8-33	-	11.0- 39.0	0.69 - 5.5	0.31	0.508	0.20-0.80
[9]	Leader	1995	0-66	-	-	1.37 - 2.76	0.75	0.254	0-0.04
[38]	Kuzdzal	1996	0-63	-	52.2	-	0.25	-	-
[39]	Jei	1996	0-66	-	-	2.60, 6.89	-	-	-
[40]	Kanki	2006	0-10,000	ISO VG 2, 32, 46	21.0	0, 1.0, 2.0	1.0	0.100	-
[41]	Kim	2008	0-50	-	7.0	-	-	0.900	0.05-0.15
[42]	Memmott	2010	0-83	ISO VG 32	21.0	1.38	1.0	0.165	0.10
[43]	Shoyama	2018	250-1,750	Water	1.0	1.0	0.4	0.480	0.004
[44]	San Andrés	2018	50-100	ISO VG 2	2.7	0.70	0.2	0.373	0.10-0.25
[45]	San Andrés	2019	30-100	ISO VG 2	2.6	0.70 - 6.2	0.2	0.373	0.10, 0.30
[11]	Li	2020	16-200	ISO VG 32	21.0	0.35	0.3	0.160	0.05
[46]	San Andrés	2021	10-70	ISO VG 2	3.1	0.70	0.2	0.279	0.10-0.20
Current	Rodríguez	2021	10-70	ISO VG 2	3.1	0.69	0.2	0.279	0.05-0.45

CHAPTER III

DESCRIPTION OF EXPERIMENTAL FACILITY AND TEST DAMPER[5]

Figure 2 depicts the SFD test rig comprising a rigid pedestal, a journal support, four support rods, a test journal, and a bearing cartridge (BC); and Table 3 lists the journal dimensions and measured ISO VG2 lubricant physical properties[6]. The elastic rods support the BC to provide a structural stiffness (K_{st}) and simulate an elastic squirrel cage. For a more complete description of the experimental apparatus, please refer to Refs. [34, 44-46]

Two orthogonally placed electromagnetic shakers, connected to the BC via stingers, apply single-frequency dynamic loads along axes X and Y to produce whirling motions of the BC with amplitude of radius r. Installed in the BC, pairs of Eddy current displacement sensors, piezoelectric accelerometers and load cells deliver measurements of the BC along the X and Y axes.

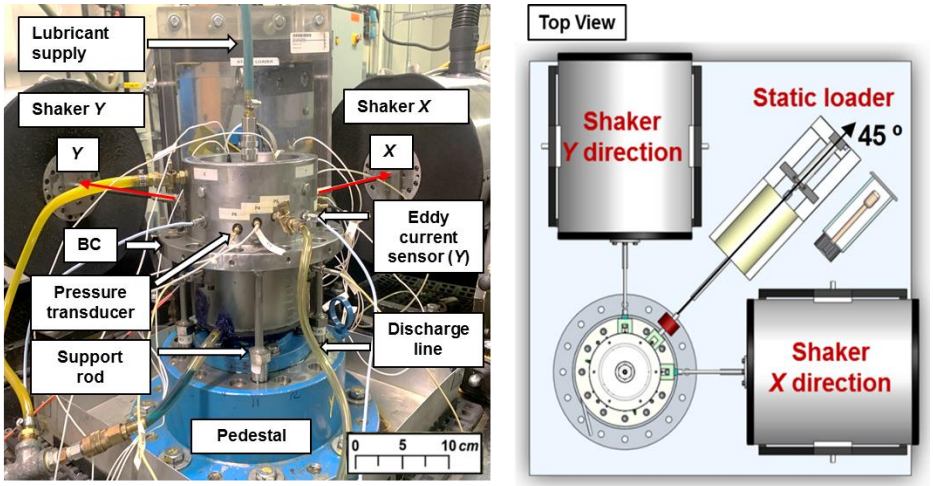

Figure 2. (a) Photograph and (b) schematic top view of SFD test rig with electromagnetic shakers and static loader [28].

Figure 3 shows (a) a top view and (b) cross-section view of the journal and BC exhibiting its main components. The short length SFD has a film axial length L = 25.4 mm, with diameter D =

[5] This section reproduces information presented in Ref. [46]
[6] Appendix A details the estimation process of the lubricant physical properties

127 mm and radial clearance c = 0.279 mm. See Appendix B for details on the identification of the journal clearance *c.* The journal comprises a base affixed to the journal support, and a sleeve connected to the lubricant supply. Additionally, the journal hosts a *dead* volume between the base and sleeve filled with lubricant, to accommodate an oil delivery plenum. A pump supplies lubricant through the center of journal, fills the plenum, flows through the mechanical check valve and into the middle plane of the film land.

Upstream of the journal, a pressure gauge and flow meter measure the inlet pressure (P_S) and lubricant flowrate into the journal. One piezoelectric transducer records the lubricant pressure inside the plenum, and another one records dynamic pressures in the squeeze film land; see Fig. 3. Finally, the lubricant exits through one discharge orifice (240^o away from X) into to a suction line and return pump that routes the oil through a bubble eliminator and into a storage tank. Figure 4 displays (a) a photograph of the journal and (b) a cross-section schematic view of the journal with its grooves. The grooves host elastomeric, off-the-shelf Buna-N O-rings, with an outer diameter of 114.6 mm and a thickness t=3.53 mm; nearly 12 times larger than the radial clearance (c).

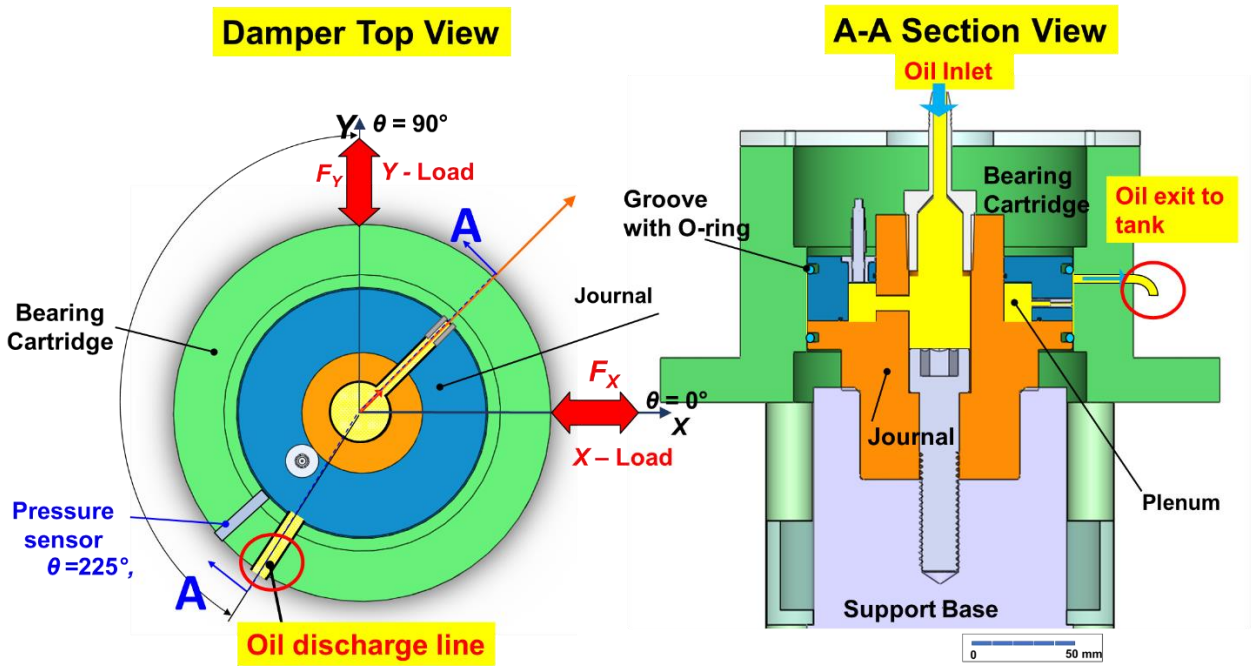

Figure 3. Schematic views (a) from top to feature one lubricant feedhole (θ_{in} = 45º, z = 0) and a discharge hole (θ_{out} = 240º, z = +¼ L) location, (b) cross-section of journal and BC showing ORs installed. (Drawings not to scale and with exaggerated features).

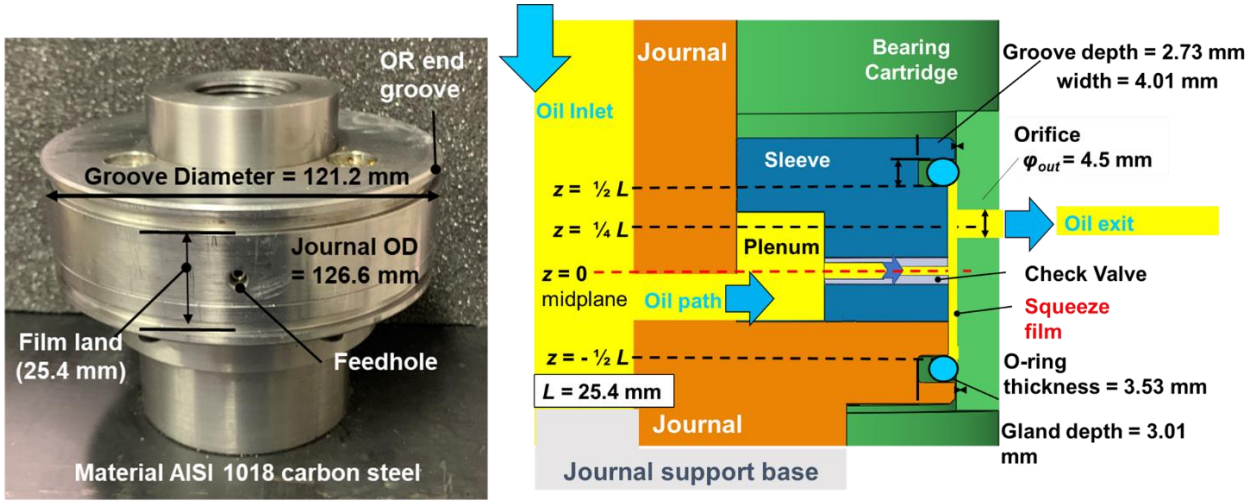

(b) Photograph of test journal **(b) Journal cross-section schematic view**

Figure. 4. (a) Photograph of test journal showcasing end grooves and a feed hole, and (b) detail of cross-section view of assembly with dimensions for grooves housing O-rings. (Drawings not to scale and with exaggerated features).

Table 3. Dimensions of SFD test section and lubricant properties.

Journal diameter, D	126.6± 0.004 mm
Axial film land length, L	25.4± 0.01 mm
Radial clearance, c	0.279 ± 0.006 mm
Feedhole diameter, ϕ_{in}	3.81± 0.01 mm
Location, z=0 and θ_{in}	45º
Discharge hole diameter, ϕ_{out}	4.50 ± 0.01 mm
Location, z= ¼ L and θ_{out}	240º
ISO VG 2 oil	
Viscosity @25ºC, μ	2.81 ± 0.01 mPa-s
Density @25ºC, ρ	800 ± 0.02 kg/m^3
O-rings [4]	**Buna-N AS568 #244**
Outer diameter	114.56 ± 0.10 mm
Inner diameter	107.54 ± 0.76 mm
Ring thickness t	3.53 ± 0.10 mm

CHAPTER IV
IDENTIFICATION OF PHYSICAL PARAMETERS OF THE TEST RIG STRUCTURE

This chapter presents the identification process of the support structure parameters, namely the structure stiffness (K_{st}), physical mass of the rig (M_{BC}), system remnant mass (M_{st}) and structure damping (C_{st}). The experiments comprise of static loads and circular centered orbit (CCO) motions (static eccentricity $e_s/c = 0$) to the test rig without oil delivered to the film land and no O-rings installed. Figure 5(a) depicts a schematic top view of experimental test rig for the measurements, and Fig. 5(b) shows a schematic cross-section view of the test rig depicting the axial location of the static load and displacement measurements. Prior to the tests, a scale measures the bearing cartridge mass (M_{BC}) by disassembling the testing apparatus, as M_{BC} = 15.6 ± 0.05 kg. Additionally, the rods supporting the BC (0.3 kg each), act like cantilever beams, and their equivalent mass is nearly one quarter [48] of the total mass of the four rods (4×0.09 kg), hence M_{BC} = 15.6 kg.

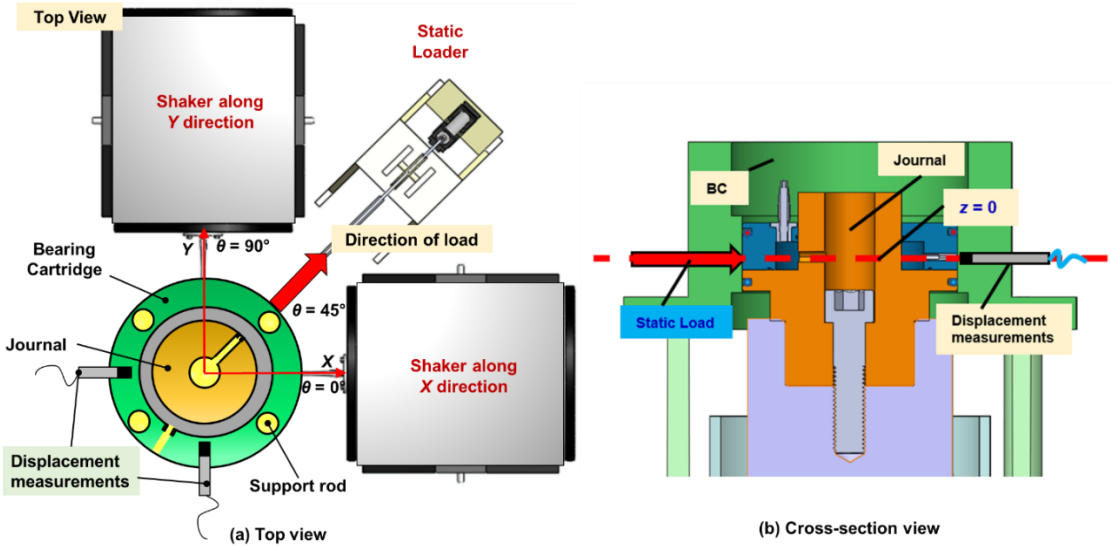

Figure 5. (a) Schematic top view of test apparatus and setup for displacement measurements. Modified from original rendition in [45]. (b) Test rig section view depicting static load and displacement axial locations.

A pneumatic piston displaces the BC relative to the journal and a pair of eddy current sensors record the BC displacements along the midplane of the film land (z = 0). Next, a linear regression curve fit to the measured load vs. displacement delivers the static stiffness coefficient of the rig structure ($K_{st,static}$). Figure 6 displays displacement (d) vs. load measurements of the test structure, along with the identified static stiffness coefficient ($K_{st,static}$=6.6 MN/m). and a coefficient of determination of R^2=0.99, establishing the model accurately characterizes the support structure. Additionally, Fig. 6 shows the BC relative displacement relative to the damper clearance (d/c). Note the estimated uncertainty in the static stiffness $U_{K,static}$= 6.6 ±0.2 MN/m (3.6%). Refer to Appendix C for a detailed description of the quantification of uncertainty from the static load measurements.

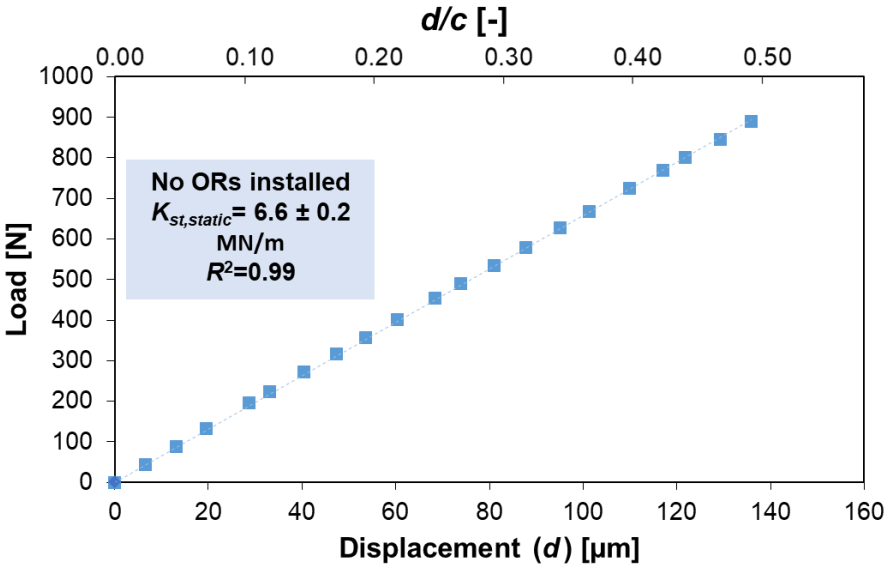

Figure 6. Static load versus BC displacement. Measurements conducted on the support structure without O-rings installed

One set of dynamic loads over a frequency range from ω=10 Hz to 130 Hz and an orbit radius r/c = 0.05 determines the complex dynamic stiffness ($\mathbf{H}_{st}$) to estimate test system force coefficients. Note the identification process employs the same frequency range as the experiments conducted with ORs installed.

For the dynamic load measurements, Figure 7 presents the measured real and imaginary parts of the direct complex dynamic stiffness ($\mathbf{H}_{st}$). The graphs also include curve fits to the physical model $\mathrm{Re}(H_{st}) = (K_{st} - \omega^2 M_{st})$ and $\mathrm{Im}(H_{st}) = (\omega C_{st})$. Table 4 lists the dry system identified force coefficients, the dry system natural frequency (f_n) and damping ratio (ζ_{st}), using the bearing cartridge mass (M_{BC}).

The inset table in Fig.78 shows a high correlation factor ($R^2 > 0.90$) between the magnitudes of $\mathrm{Re}(H_{st})$ and the physical model $(K_{st} - \omega^2 M_{st})$. Hence, the model accurately represents the test structure support stiffness (K_{st}) and remnant mass (M_{st}). However, the magnitudes of $\mathrm{Im}(H_{st})$ shown in Fig. 7 are small, along with low correlation factors ($R^2 < 0.10$) to the model $\mathrm{Im}(H_{st}) = (\omega C_{st})$, denoting the support structure damping (C_{st}) is not of viscous type. The identified parameters produce an estimated viscous damping ratio (ζ_{st}) of just ~1%, and a natural frequency $f_n = 100.5$ Hz.

Incidentally, an impact load test conducted with an accelerometer attached to the BC 45° between the X and Y axes verifies closely the system natural frequency at $f_n = 98$ Hz.

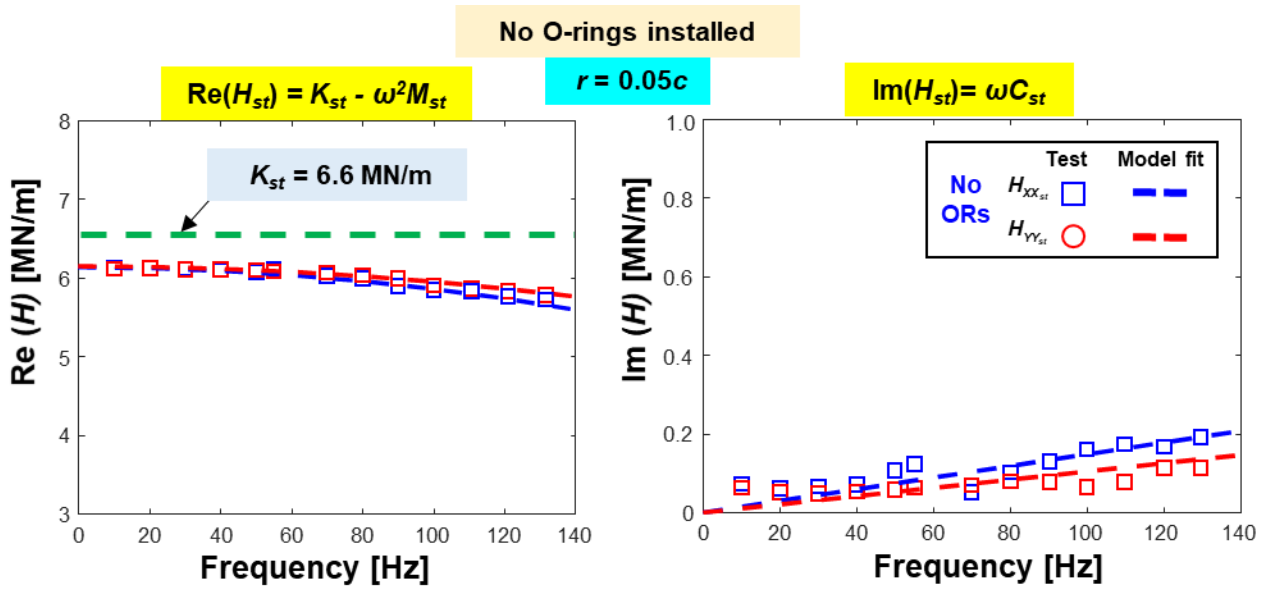

R^2 (Correlation factor)			
Re(H_{XX})	Re(H_{YY})	Im(H_{XX})	Im(H_{YY})
0.95	0.92	0.07	0.08

Figure 7. Test rig system (without lubricant and no O-rings). Real and imaginary parts of system direct complex dynamic stiffness versus excitation frequency. Circular orbits with radius $r = 0.05c$ and bearing centered ($e_s/c = 0.0$). Frequency range ω = 10 Hz to 130 Hz.

The experimental results show that the system is slightly orthotropic ($K_{XX} < K_{YY}$, $C_{XX} < C_{YY}$, $M_{XX} < M_{YY}$) since the experimental apparatus includes several lubricant lines and connections to the various sensors. The identification reveals the rig support stiffness $K_{st,YY}$ is ~2% larger than $K_{st,XX}$, and $M_{st,XX}$ is nearly 10% larger than $M_{st,YY}$. Similarly, $K_{st,static}$ is different by ~5% to the arithmetic mean of $K_{st,XX}$ and $K_{st,YY}$ ($K_{st,avg}$=6.25 MN/m) estimated from the periodic loads. Additionally, please refer to Appendix C for details of the estimation of the uncertainty in the measurements. The orthotropy in M_{st} and K_{st}, and the discrepancy between K_{st} and $K_{st,static}$, fall within the range of total uncertainty (SFD + ORs + structure) in the measurements, U_K=7.2%, U_M=11.1% of the physical parameters estimated at a selected nominal condition, see Appendix C. While the magnitudes of uncertainty in the measurements are sizeable their proportion is rather

common in the identification of SFD force coefficients in the present experimental facility; see for example refs. [34, 44, 45 and 47].

Table 4. Structure physical parameters obtained from circular orbit tests. Parameters identified over a frequency range from ω=10 to 130 Hz. Orbit amplitude r/c = 0.05 and static eccentricity e_s/c = 0.0. M_{BC}=15.6 kg.

Physical parameter		Structure (no ORs)			
		XX	*YY*	*XY*	*YX*
Stiffness	K_{st} [MN/m]	6.2 ± 0.3	6.3 ± 0.3	-0.02	-0.05
Remnant Mass	M_{st} [kg]	1.7 ± 0.7	1.9 ± 0.7	0.20	0.30
Damping	C_{st} [kN-s/m]	0.2 ± 0.1	0.3 ±0.1	0.01	0.02
Natural Frequency	f_n [Hz] $= \sqrt{K_{st} / M_{BC}}$	100 ± 3.0	101 ±3.0		
Damping Ratio	ζ_{st} [-] $= C_{st} / (2\sqrt{K_{st} M_{BC}})$	0.01	0.01		

CHAPTER V
IDENTIFIED STATIC STIFFNESS COEFFICIENT OF A PAIR OF O-RING SEALS WITH A PRESSURIZED JOURNAL CLEARANCE

This chapter presents the identification of the O-ring stiffness ($K_{OR,static}$). First, a series of static loads displace the BC with O-ring seals installed in the test journal to identify $K_{OR,static}$ without any external pressurization (P_S = 0.0 barg). Next, still with ORs installed, and while supplying pressurized air into the damper clearance, three sets of static load measurements clearance follow to estimate $K_{OR,static}$. All the experiments comprise a static load range over 0 N to ~900 N and the selected air supply pressures are: P_S=0.69, 3.45 and 6.9 bar(g). The aim of the measurements is to impose a preload to the ORs by pressurizing the system, and to identify any effect of the pressurized gas supply to the ORs' stiffness. Prior to the experiments, a verification test with air supplied at P_S= 7 bar(g) demonstrates the ORs perfectly seal the film land by not allowing air through flow.

Figure 8 displays displacement (d) and relative displacement (d/c) vs. load measurements of the sealed journal and identified structure and O-rings static stiffness coefficients ($K_{st+OR,static}$). The correlation coefficient R^2=0.99 to the data in Fig. 8 indicates a static stiffness accurately characterizes the structure stiffness with ORs installed for all experimental conditions.

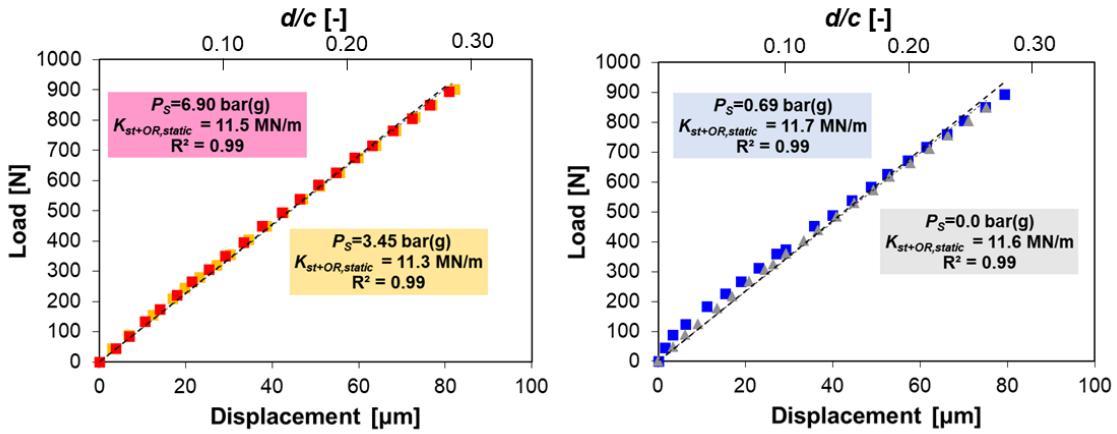

Figure 8. Static load versus BC displacement with OR sealed journal: (a) Measurements conducted at P_S = 0.69 bar(g) and P_S = 0.0 bar(g), (b) Measurements conducted at P_S = 3.45 bar(g) and P_S = 6.90 bar(g)

Table 5 summarizes the static stiffness coefficients identified from data in Fig. 6 and Fig. 8. Table 5 indicates the support structure (no ORs installed) is $K_{st,static}$=6.6 MN/m, and $K_{st+ORs,static}$=11.6 MN/m (P_S=0.0 barg), showing an increase in the system static stiffness by ~45%. Moreover, the magnitudes of $K_{st+OR,static}$ from measurements with pressurized air delivered to the journal clearance, are almost identical to $K_{st+OR,static}$ estimated at P_S=0.0 bar(g). The ORs' equivalent static stiffness coefficient ($K_{ORs,static}$) equals to the identified stiffness coefficients of the structure with ORs installed ($K_{st+OR,static}$) minus the contribution of the test structure ($K_{st,static}$). Hence, for the two O-rings:

$$K_{OR,static}=K_{st+OR,static}-K_{st,static} \tag{11}$$

Note, the stiffnesses in Eq. (11) represent arithmetic means, that is K= ½(K_{XX}+K_{YY}). Table 5 shows the equivalent static stiffness for the ORs, $K_{OR,static}$ = 5.0 MN/m. Experimental results reported by Green and Etsion in Ref. [19] describe the effects of squeeze and pressure on the dynamic force coefficients of elastomeric ORs. The experimental results in Ref. [19] demonstrate an increase in stiffness by nearly three times by pressurizing the ORs to P_S=4.0 bar(g).

Nevertheless, the current measurements show that pressurizing the system with air up to P_S=6.90 bar(g) does not modify the ORs static stiffnesses.

Table 5. Test structure and ORs physical parameters obtained from static load tests and with three supply pressures (P_S). Parameters identified over a load range from 0 to ~900 N.

Experimental Condition	P_S [barg]	Static Stiffness $K_{st,static}$ [MN/m]
Structure alone	-	6.6 ± 0.4
Structure + ORs	0.0	11.6 ± 0.4
	0.69	11.7 ± 0.4
	3.45	11.3 ± 0.4
	6.90	11.5 ± 0.4
Equivalent of two ORs alone	-	5.0 ± 0.4

CHAPTER VI
IDENTIFIED PARAMETERS OF A PAIR OF O-RING SEALS UNDERGOING CIRCULAR CENTERED WHIRL ORBITS

This chapter details the identification of the O-ring seals dynamic force coefficients (K_{OR}, $K_{\perp}$, C_{OR}) by exerting periodic loads on the dry (unlubricated) system. Figures 9 and 10 present (a) contour plots of the measured real and imaginary parts of the complex dynamic stiffnesses for the dry system with ORs installed, $\mathrm{Re}(H_{st+OR})_{XX,YY}$ and $\mathrm{Im}(H_{st+OR})_{XX,YY}$, respectively, versus whirl frequency (ω) and increasing orbit radii (r/c). Figures 9 and 10 (b) show 3D plots of $\mathrm{Re}(H_{st+OR})_{XX,YY}$ and $\mathrm{Im}(H_{st+OR})_{XX,YY}$, against the squeeze velocity $v_s=(r\omega)$ and r/c. The experimental data in Figs. 9 and 10 span a whirl frequency range from ω=10 Hz to 130 Hz, orbit amplitudes r = 0.05c to 0.45c, hence v_s=0.9 mm/s to 102.5 mm/s. Experiments conducted at ambient pressure; without any external pressurization (P_S=0.0 barg).

Figure 9 (a) shows the magnitudes of $\mathrm{Re}(H_{st+OR})_{XX,YY}$ start at nearly 14 MN/m, at r/c = 0.05 for both $(H_{st+OR})_{XX,YY}$ and increase with whirl frequency (ω) up to ~16.5 MN/m as $\omega \rightarrow$ 130 Hz (v_s=11.4 mms/s). Additionally, for r/c = 0.05, 0.10, 0.15 and 0.20, the magnitudes of $\mathrm{Re}(H_{st+OR})_{XX,YY}$ are larger than the structure and ORs static stiffness coefficient ($K_{st+OR,static}$ = 11.5 MN/m), see Table 5, and denoted as a fixed horizontal blue plane in Fig. 9. However, as the orbit radius increases beyond r = 0.25c, $\mathrm{Re}(H_{st+OR})_{XX,YY}$ decreases below $K_{st+OR,static}$. For the largest orbit radii ($r \geq 0.25c$) the magnitude of $\mathrm{Re}(H_{st+OR})_{XX,YY}$ is so low that it approaches to that of structure stiffness alone, K_{st} = 6.3 MN/m. Thus, the measurements show that for amplitudes of motion r<0.25c, there is a stiffening effect in the ORs, but as (r/c) increases, the ORs stiffness (K_{OR}) decreases. Regarding the effects of whirl frequency on the dry test system stiffness, $\mathrm{Re}(H_{st+OR})_{XX,YY}$ increases from ω=10 Hz to 40 Hz (v_s=0.9 mm/s to 7.0 mm/s), particularly at r/c = 0.05 and 0.10. Then, as r/c grows, the increase in $\mathrm{Re}(H_{st+OR})_{XX,YY}$ with whirl frequency becomes less prominent.

Do note the experimental data in Fig. 9 has accounted for the effects of the BC mass by removing M_{BC}=15.6 kg during the postprocessing of the dynamic load measurements. However, the (small) magnitude of a BC remnant mass, $M_{st=}$1.8 kg, is still present in Re$(H_{st+OR})_{XX,YY}$. Hence, Fig. 9 displays $(K_{st} - \omega^2 M_{st})$ as a green horizontal plane and shows the effect of the remnant mass is too small to affect the measurements conducted with the ORs installed.

Figure 9 (b) displays Re$(H_{st+OR})_{XX,YY}$ vs. increasing (r/c) and the corresponding magnitude of $v_s=(r\omega)$, and shows with more clarity the ORs' stiffness amplitude dependence. In particular, for r/c=0.05, Re$(H_{st+OR})_{XX,YY}$ increases within a short range of squeeze velocities, from v_s =0.9 mm/s to 4.4 mm/s. However, for r=0.05c, Re$(H_{st+OR})_{XX,YY}$ remains fairly constant at ~15 MN/m as $v_s \rightarrow$ 8.9 mm/s. At r = 0.10c, there is only a noticeable increase in Re$(H_{st+OR})_{XX,YY}$, from v_s= 3 mm/s to 7.0 mm/s, and then remains constant as $v_s \rightarrow$ 23 mm/s. For all the other orbit amplitudes (r/c = 0.15 to 0.45), Re$(H_{st+OR})_{XX,YY}$ does not increase significantly with an increasing v_s. Hence, Fig. 9 (b) shows the ORs stiffness is mainly a function of the orbit amplitude.

The imaginary parts of the complex dynamic stiffnesses depicted in Fig. 10 show similar trends as their real counterparts. First, Im$(H_{st+OR})_{XX,YY}$ suddenly decreases as the orbit radius increases. In this case, Im$(H_{st+OR})_{XX,YY}$ for r= 0.05c and 0.10c have nearly identical magnitudes, for both H_{XX} and H_{YY}, and then decay to ~2MN/m as $r \geq$ 0.10c. Next, there is a steady increase in Im$(H_{st+OR})_{XX,YY}$ as ω grows, for measurements recorded at all orbit amplitudes. However, this increase becomes less pronounced as (r/c) increases. Incidentally, the magnitudes of Im$(H_{st+OR})_{XX,YY}$ as $\omega \rightarrow$ 0 Hz are sizeable, thus showing the effect of a quadrature stiffness ($K_{\perp}$) as $\omega \rightarrow$ 0 Hz, indicative of a structural-like damping.

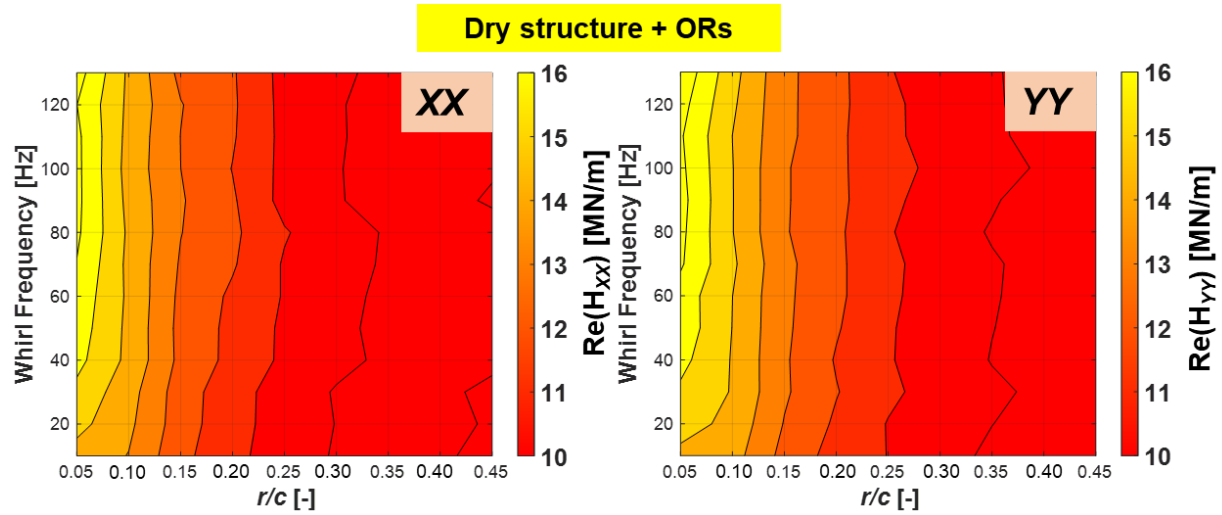

(a) Contour plots of Re(H_{st+OR})$_{XX,YY}$ vs. whirl frequency (ω) and orbit radius (r/c)

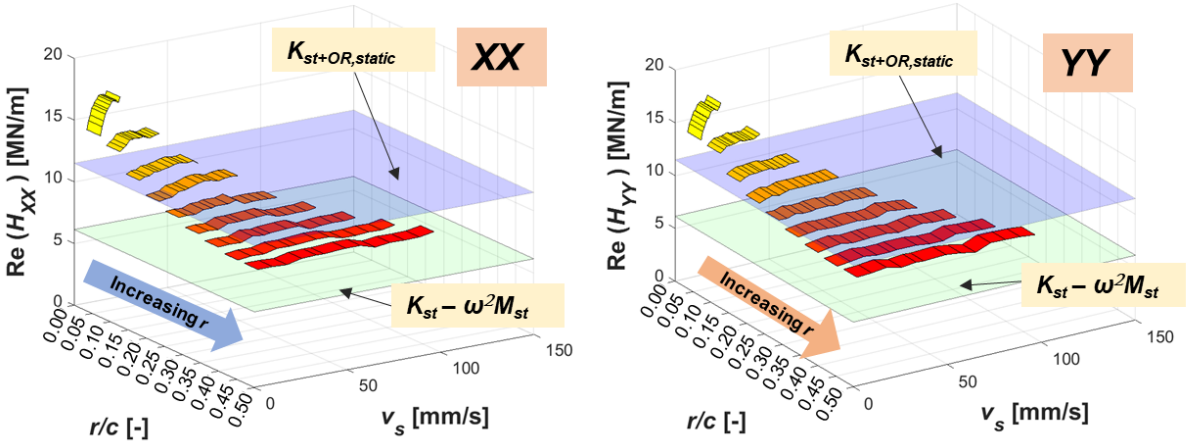

(b) Re(H_{st+OR})$_{XX,YY}$ vs. squeeze velocity (v_s) and orbit radius (r/c)

Figure 9. Dry structure + ORs. (a) Contour plots of (H_{st+OR})$_{XX,YY}$ vs. whirl frequency (ω) and orbit radius (r/c). (b) Re(H_{st+OR})$_{XX,YY}$ vs. squeeze velocity (v_s) and r/c. CCOs with radius r = 0.05c to 0.45c. Frequency range ω = 10 Hz to 130 Hz. P_S=0.0 bar(g).

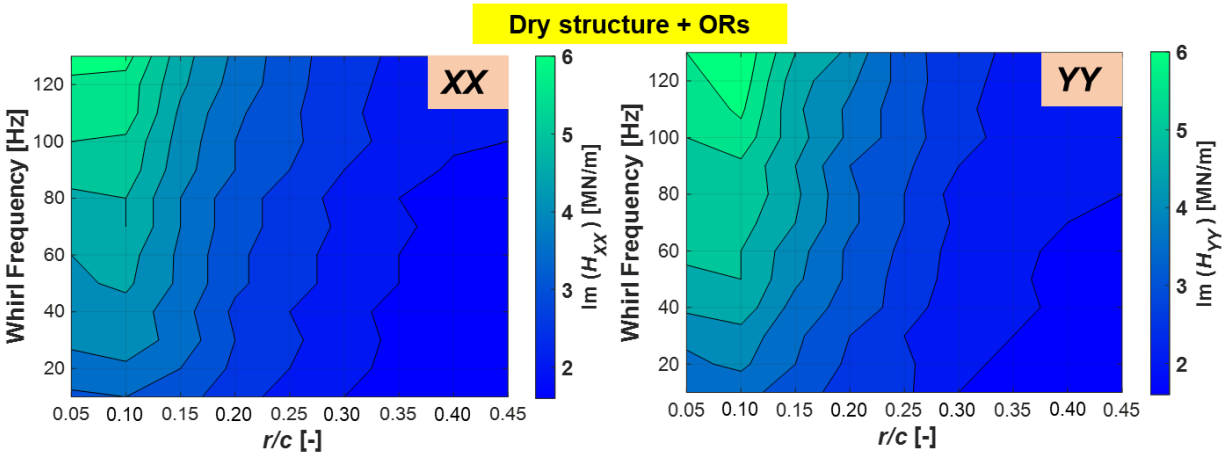

(a) Contour plots of Im(H_{st+OR})$_{XX,YY}$ vs. whirl frequency (ω) and orbit radius (r/c)

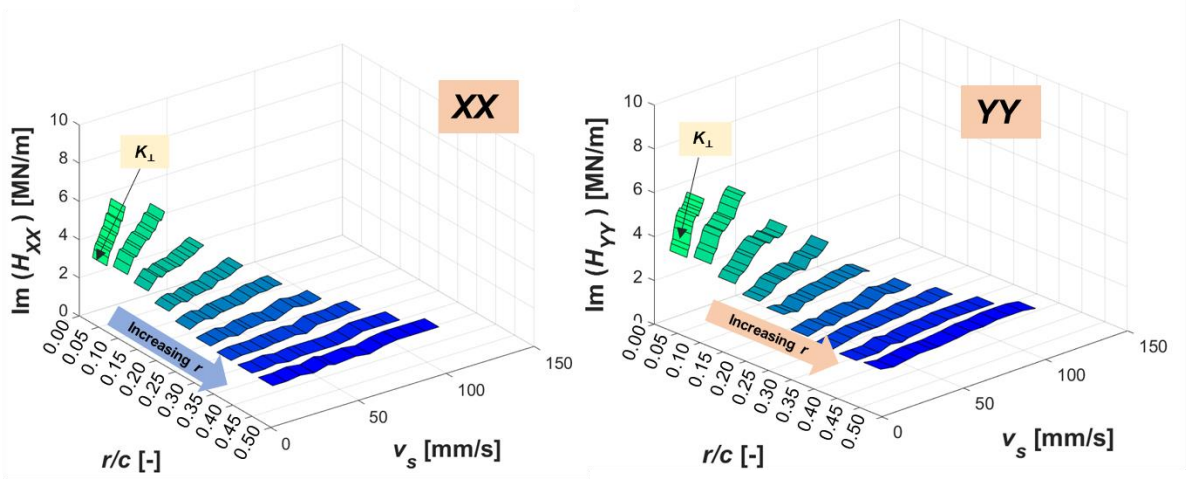

(b) Im(H_{st+OR})$_{XX,YY}$ vs. squeeze velocity (v_s) and orbit radius (r/c)

Figure 10. Dry structure + ORs. (a) Contour plots of (H_{st+OR})$_{XX,YY}$ vs. whirl frequency (ω) and orbit radius (r/c). (b) Im(H_{st+OR})$_{XX,YY}$, vs. squeeze velocity (v_s) and r/c. CCOs with radius r = 0.05c to 0.45c. Frequency range ω = 10 Hz to 130 Hz. P_S=0.0 bar(g).

Figure 11 shows the real parts of the ORs complex dynamic stiffness (contribution from the test structure removed), vs. (a) whirl frequency and vs. (b) squeeze velocity, that is, [Re($\mathbf{H}_{OR}$)= Re($\mathbf{H}_{st+OR}$) - Re($\mathbf{H}_{st}$)], to identify the O-rings complex stiffnesses. Note Fig. 11 shows the magnitude of the OR static stiffness $K_{OR,static}$= 5.0 MN/m for comparison with the results obtained from the dynamic loads. Figure 11 also reveals with more clarity that the magnitudes of

Re(H_{OR})$_{XX,YY}$ quickly drop as the whirl amplitude increases. Moreover, for small orbit amplitudes, from r = 0.05c to 0.20c, the magnitudes of Re(H_{OR})$_{XX,YY}$ > $K_{OR,static}$, whereas Re(H_{OR})$_{XX,YY}$ < $K_{OR,static}$ for larger orbit radii.

Even though Re(H_{OR})$_{XX,YY}$ quickly grows at r = 0.05c and 0.10c, from v_s= 0.9 to 7.0 mm/s (ω = 10 to 40 Hz), there are small differences in Re(H_{OR})$_{XX,YY}$ as the orbit amplitudes and frequency increase beyond ω > 40 Hz and r > 0.10c. Hence, establishing frequency independent ORs stiffness coefficients with the model Re(H_{OR}) → (K_{OR})

Figure 12 presents the imaginary part of the dry ORs dynamic stiffness, [Im($\mathbf{H}_{OR}$)= Im($\mathbf{H}_{st+OR}$)- Im($\mathbf{H}_{st}$)], vs. (a) whirl frequency and (b) squeeze velocity (v_s). The measurements in Fig. 12 are nearly identical to Im(H_{st+OR})$_{XX,YY}$, since Im(H_{st})$_{XX,YY}$ is at least an order of magnitude lower than the measurements with ORs installed. Thus, the trends in Fig. 12 show Im(H_{OR})$_{XX,YY}$ quickly decays with an increasing orbit radius, and steadily rises as the whirl frequency grows. Correspondingly, Fig. 12 shows the presence of a quadrature stiffness ($K_{\perp}$), indicative of a structure-like damping coefficient in the O-rings.

Employing the model Im(H_{OR}) =($K_{\perp}$+ ωC_{OR}) to the measurements in Fig. 12 results in the identification of OR damping (C_{OR}) and quadrature stiffness ($K_{\perp}$) coefficients *strictly* valid over the frequency range ω = 10-130 Hz and representative of the pair of ORs used in the experiments. Presently, the estimation of viscous-like **equivalent** OR damping coefficients enables the identification of the film damping coefficients (C_{SFD}) by simply removing C_{OR} from the lubricated system damping, C_L. By employing C_{OR}, the distinction from the support structure and the squeeze film in the lubricated system experiments is evident, that is C_L = (C_{OR} + C_{SFD}), as discussed in the following section. Additionally, the current method utilizes the OR loss factor as $\eta = K_{\perp}/K_{OR}$, to identify structural-like damping coefficients occurring as ω → 0 Hz.

Figure 13 summarizes the identified OR force coefficients (C_{OR}, $K_{\perp}$, K_{OR}) vs. orbit radius (r/c). and includes error bars denoting the uncertainty for each parameter. Additionally, Figure 13 shows the loss factor $\eta = K_{\perp}/K_{OR}$ vs. (r/c), as a measure of the ratio between OR material-like structural damping over stiffness. The O-ring parameters (C_{OR}, $K_{\perp}$, K_{OR}) show an abrupt decrease as $r \rightarrow 0.20c$, and then show a less pronounced reduction as the orbit radius $r \rightarrow 0.45c$. Incidentally, the ORs' loss factor remains relatively constant throughout the experimental orbit amplitudes. Only at $r = 0.05c$, $\eta = 0.35$. For the rest of the orbit amplitudes, the ratio remains at $\eta = 0.5$, showing the whirl orbit amplitudes have nearly the same effect on both OR stiffness and damping.

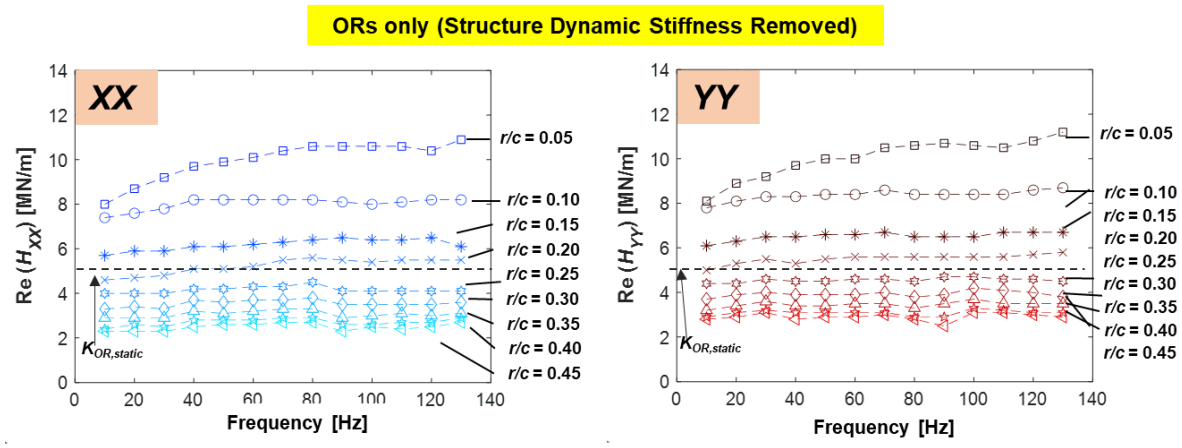

(a) Re(H_{OR})$_{XX,YY}$ vs. whirl frequency (ω) and orbit radius (r/c)

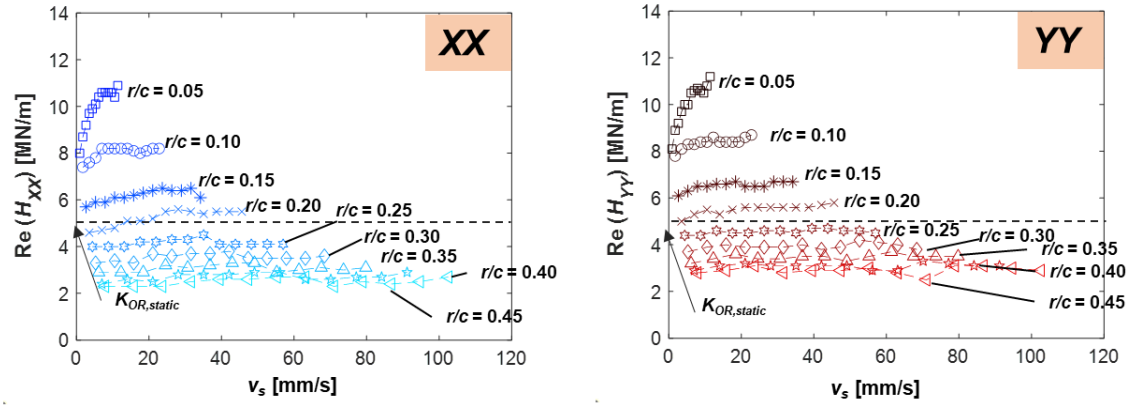

(b) Re(H_{OR})$_{XX,YY}$ vs. squeeze velocity (v_s) and orbit radius (r/c)

Figure 11. ORs force coefficients only (structure removed). (a) Real part of direct complex dynamic stiffnesses Re(H_{OR})$_{XX,YY}$ vs. whirl frequency (ω) and orbit radius (r/c). (b) Re(H_{OR})$_{XX,YY}$, vs. squeeze velocity (v_s) and orbit radius (r/c). CCOs with radius r = 0.05c to 0.45c. Frequency range ω = 10 Hz to 130 Hz (v_s = 0.9 mm/s to 102.5 mm/s). P_S= 0.0 bar(g).

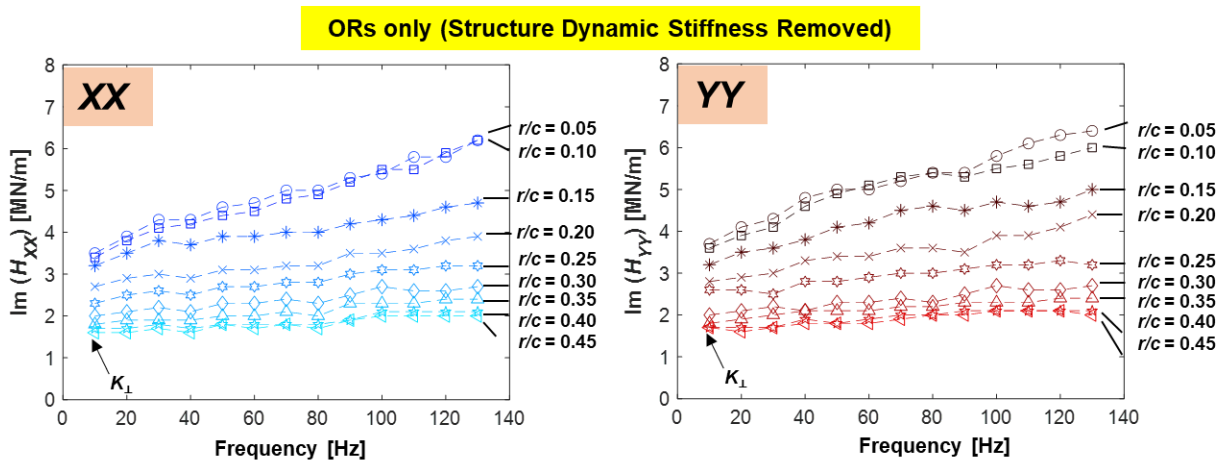

(a) Im(H_{OR})$_{XX,YY}$ vs. whirl frequency (ω) and orbit radius (r/c)

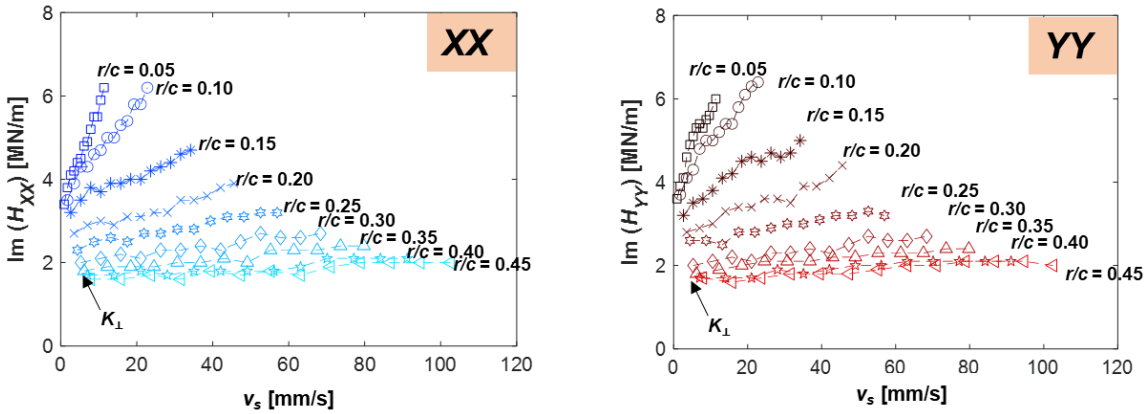

(b) Im(H_{OR})$_{XX,YY}$ vs. squeeze velocity (v_s) and orbit radius (r/c)

Figure 12. ORs force coefficients only (structure removed). (a) Imaginary part of direct complex dynamic stiffnesses Im(H_{OR})$_{XX,YY}$ vs. whirl frequency (ω) and orbit radius (r/c). (b) Im(H_{OR})$_{XX,YY}$, vs. squeeze velocity (v_s) and orbit radius (r/c). CCOs with radius r = 0.05c to 0.45c. Frequency range ω = 10 Hz to 130 Hz (v_s = 0.9 mm/s to 102.5 mm/s). P_S= 0.0 bar(g).

For the lowest orbit amplitude (r =0.05c), the estimated OR stiffness coefficients (K_{OR}) are twice the stiffness identified with static loads ($K_{OR,static}$) and then abruptly decline as the orbit radius increases. The measurements show (K_{OR}) estimated from dynamic loads are larger than the static stiffness ($K_{OR,static}$) only for orbit amplitudes from r=0.05c to 0.20 c. For larger orbit radii, K_{OR} continues to decrease below $K_{OR,static}$; and for the largest orbit radius (r = 0.45 c), K_{OR} drops to

~0.5$K_{OR,static}$. The measurements show the significant effect of whirl motion amplitudes on the OR stiffness; that is, a stiffening effect for small amplitudes of motion (r = 0.05c to 0.20c), and a softening effect for large amplitude of motion (r = 0.25c to 0.45c). The trend with these findings correlates with those reported in Ref. [18]. However, the current measurements show a more pronounced reduction in K_{OR} as the orbit radius (r/c) increases.

In addition, Figure 13 presents the estimated OR quadrature stiffness ($K_{\perp}$) and OR damping (C_{OR}) coefficients. In this case, $K_{\perp}$ decreases by nearly 75% and C_{OR} drops by ~80% as the orbit radius increases from r=0.05c to r=0.45c. Additionally, the steep decrease in damping as amplitude of motion increases agrees with the trend observed in the experimental results by Smalley et al. [18]. The derived material loss factor $\eta = K_{\perp}/K_{OR}$ ~0.50 for most orbit amplitudes.

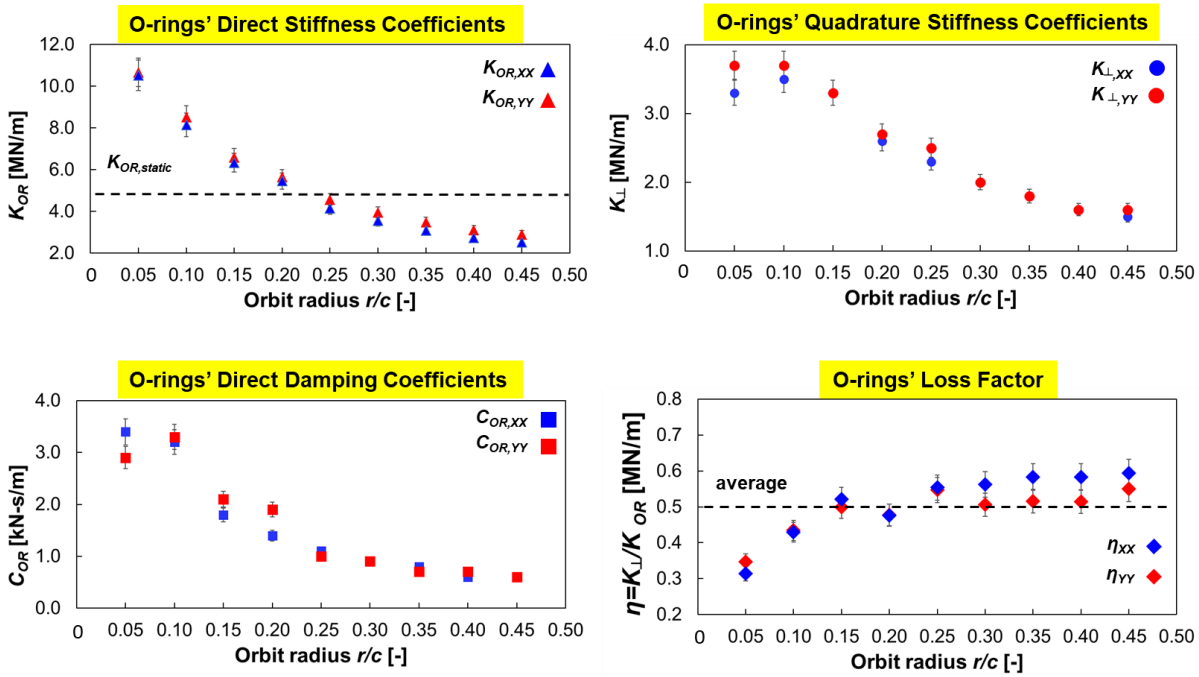

Figure 13. Pair of ORs' stiffness (K_{OR})$_{XX,YY}$, quadrature stiffness ($K_{\perp}$)$_{XX,YY}$, damping (C_{OR})$_{XX,YY}$ and loss factor (η)$_{XX,YY}$ vs. orbit radius (r/c). Estimated parameters from circular whirl orbits (e_s/c = 0) and frequency range ω = 10 – 130 Hz. P_S=0.0 bar(g).

The estimated parameters show a slight orthotropy in the identified coefficients ($K_{XX,OR}$ < $K_{YY,OR}$, $C_{XX,OR}$ < $C_{YY,OR}$, $K_{\perp,XX}$ < $K_{\perp,YY}$). Note, the difference between the coefficients along the X and

Y axes lies within the uncertainty range of the measurements (see Appendix C). Importantly enough, the magnitudes of the measurements with a dry system and ORs installed are at least an order of magnitude larger than their cross-coupled counter parts. See Appendix D for details on the test system identified cross-coupled coefficients.

Table 6 shows the correlation coefficients (R^2) used to quantify the goodness of fit of the model [$\mathrm{Re}(H_{OR})=K_{OR}$, $\mathrm{Im}(H_{OR})=(K_{\perp} + \omega C_{OR})$] to the data. Importantly enough, the magnitudes of $R^2 >$ 0.90 for $\mathrm{Re}(H_{OR})=K_{OR}$, showing that even with a noticeable increase in $\mathrm{Re}(H_{OR})_{XX,YY}$ at $r = 0.05c$ and $0.10c$ and from v_s= 0.9 mm/s to 7.0 mm/s, the model accurately represents the measurements. Similarly, the magnitudes of $R^2 > 0.90$ for [$\mathrm{Im}(H_{OR})=(K_{\perp} + \omega C_{OR})$], validate the identification of frequency independent damping coefficients over the experimental frequency range.

Table 6. Goodness of fit in the identified physical parameters. Coefficients of determination (R^2) vs. orbit radius from r= 0.05c to 0.45c, ω = 10 to 130 Hz.

r/c	$\mathrm{Re}(H_{OR})=K_{OR}$		$\mathrm{Im}(H_{OR})=K_{\perp} + \omega C_{OR}$	
[-]	R^2 [-]		R^2 [-]	
	XX	*YY*	*XX*	*YY*
0.05	0.93	0.92	0.99	0.92
0.10	0.99	0.99	0.98	0.98
0.15	0.98	0.99	0.95	0.91
0.20	0.99	0.99	0.95	0.95
0.25	0.96	0.96	0.96	0.93
0.30	0.96	0.98	0.93	0.93
0.35	0.94	0.99	0.94	0.95
0.40	0.99	0.95	0.90	0.94
0.45	0.99	0.97	0.91	0.90

The experimental results show similar amplitude of motion ORs affects the ORs' force coefficients. However, other published experimental efforts are scarce. For example, Ref. [18]. Nevertheless, there are numerous experimental efforts showing the effects of periodic strain amplitude on different types of polymeric structures, such as beams, cylinders and plates. As early as 1962, experimental efforts by Payne [49], consisted of a series of periodic loading tests conducted on filler reinforced rubber specimens, showed that the elastomer modulus (E) declines as the strain amplitude (ε) increases. More recent experimental results, see García et al. [50] (in 2007), identify direct stiffness (K) and loss factor (η) coefficients of a filler-reinforced rubber bushing employed in automotive suspensions. The experiments consist of a frequency range from ω=0 Hz to 50 Hz and unidirectional amplitudes of motion up from 0.04 mm to 0.50 mm. The results reported in Ref. [50] shows similar trends as those found in Fig. 11; a decrease in the direct stiffness (K) as the amplitudes of motion grow, along with slight increments in stiffness as $\omega \rightarrow$50 Hz.

Additionally, experiments conducted by Rendek and Lion [51] in 2010, report the amplitude dependence of numerous rubber compounds by conducting unidirectional dynamic loads. The experiments, consisting of periodic strain (ε) amplitudes of up to 30% at excitation frequencies from 0.5 Hz to 50 Hz. Rendek and Lion, in Ref. [51] document a decrease in stiffness in the rubber specimen, in the form of a storage (E') modulus of ~65% as the strain amplitude increases from 0.001% to 10%. Moreover, the test specimen shows a substantial decrease in damping in the form of a loss modulus (E'') of nearly 85%, given the same increase in strain amplitude. Incidentally, the drop in the complex modulus E with growing amplitudes of motion reported in Ref. [51] is of the same magnitude as the decrease in K_{OR} and C_{OR} with increasing orbit radius shown in Figs. 11 and 12. The authors in Refs. [49-51] attribute the decrease in material moduli to dynamic

breakdown and recovery in the polymer inner structure, and to the interaction of rubber with filler structures embedded in the test articles' polymeric compounds.

For small amplitudes of motion, the complex modulus of filler reinforced polymers is large as the reformation of the structure occurs rapidly [52]. For large amplitudes of periodic loads, the polymeric inner structure bonds break down so extensively, that its reformation is much slower than the strain cycle time, leading to both low stiffness and damping characteristics [52]. It is worth noting that the composition of the test O-rings used in the current experiments is similar to the polymeric test articles tested in Refs. [49-51]. The ORs, contain 50% to 60% base polymer (nitrile butadiene rubber), along with various fillers, vulcanizing agents, aging retardants, and other chemicals [3]. Hence, the reduction in OR stiffness and damping with increasing orbit amplitudes should be expected.

Note the identification assumes both O-rings' force coefficients (top and bottom) have the same magnitude, both under static and dynamic loads. Please see Appendix E for an assessment of the reaction forces of each O-ring.

CHAPTER VII
IDENTIFIED PARAMETERS OF AN O-RINGS SEALED SQUEEZE FILM DAMPER UNDERGOING CIRCULAR CENTERED ORBITS

This chapter presents measurements conducted both with ORs installed and a lubricated system, along with the identification of SFD dynamic force coefficients (C_{SFD}, M_{SFD}). The experiments comprise a series of circular centered orbits (e_s/c=0.0) over a frequency range from ω = 10 Hz to 70 Hz (v_s=0.9 mm/s to 55.2 mm/s), and nine orbit radii, r/c = 0.05, 0.10, 0.15…, to 0.45. The lubricant, ISO VG 2, enters the film land with a supply pressure P_S=0.69 bar(g) (10 psig) and a lubricant flow rate[7] Q_S= 0.8 LPM. Installed in the journal end grooves, two elastomeric O-rings seal the film land and prevent lubricant through flow.

Figures 14 and 15 (a) present contour plots of the real and imaginary parts of $(H_L)_{XX,YY}$ vs. whirl frequency (ω) and orbit radius (r/c). Figures 14 and 15 (b) show magnitudes of $(H_L)_{XX,YY}$ vs. squeeze velocity ($v_s=r\omega$) and (r/c). In Fig. 16, the intercept of Re$(H_L)_{XX,YY}$ with the vertical axis produces the direct stiffnesses K_{XX} and K_{YY}, with a magnitude approximately equal to that of the dry test system (K_{st+ORs}). Additionally, the measurements depict the amplitude dependence in K_{OR} as (r/c) increases, shown as a reduction in the magnitude of the intercept of Re$(H_L)_{XX,YY}$ with the vertical axis. Next, Re$(H_L)_{XX,YY}$ quickly decays with an increasing whirl frequency, to reveal a downward parabolic trend characteristic of fluid inertia. However, this trend is only noticeable throughout the entire whirl frequency range for small amplitudes, namely r = 0.05c to 0.20c, or up to v_s=24.5 mm/s. For $r \geq$ 0.25c, Re$(H_L)_{XX,YY}$ increases as $\omega \rightarrow$ 70 Hz (v_s=31 mm/s). More noticeably, for r = 0.30c, where Re$(H_L)_{XX,YY}$ abruptly increases at ω = 55 and 70 Hz (v_s =37 mm/s and 29 mm/s, respectively). This effect continues until Re$(H_L)_{XX,YY}$ produces an upward trend as

[7] See Appendix F for measurements of the lubricant flow vs supply pressure under static conditions.

frequency increases, see Fig. 14 (b), and thus resulting in a dramatic decrease in the squeeze film inertia as $r \rightarrow 0.45c$.

Conversely, in Fig. 15, the sizeable magnitude of $\mathrm{Im}(H_L)_{XX,YY}$ as $\omega \rightarrow 0$ Hz indicates the presence of a quadrature stiffness, ($K_\perp$) representative of the ORs structural-like damping effects in the lubricated system. Just as in the experiments without lubricant, the intercept of $\mathrm{Im}(H_L)_{XX,YY}$ with the vertical axis quickly drops as (r/c) grows. Subsequently, $\mathrm{Im}(H_L)_{XX,YY}$ shows a linear increase as $\omega \rightarrow 70$ Hz, typical of viscous damping (C_{SFD}) generated by the squeeze film. However, for whirl amplitudes larger than $r = 0.35c$, at $\omega = 55$ Hz and 70 Hz, corresponding to v_s=34 mm/s and 43 mm/s, $\mathrm{Im}(H_L)_{XX,YY}$ substantially reduces its magnitude.

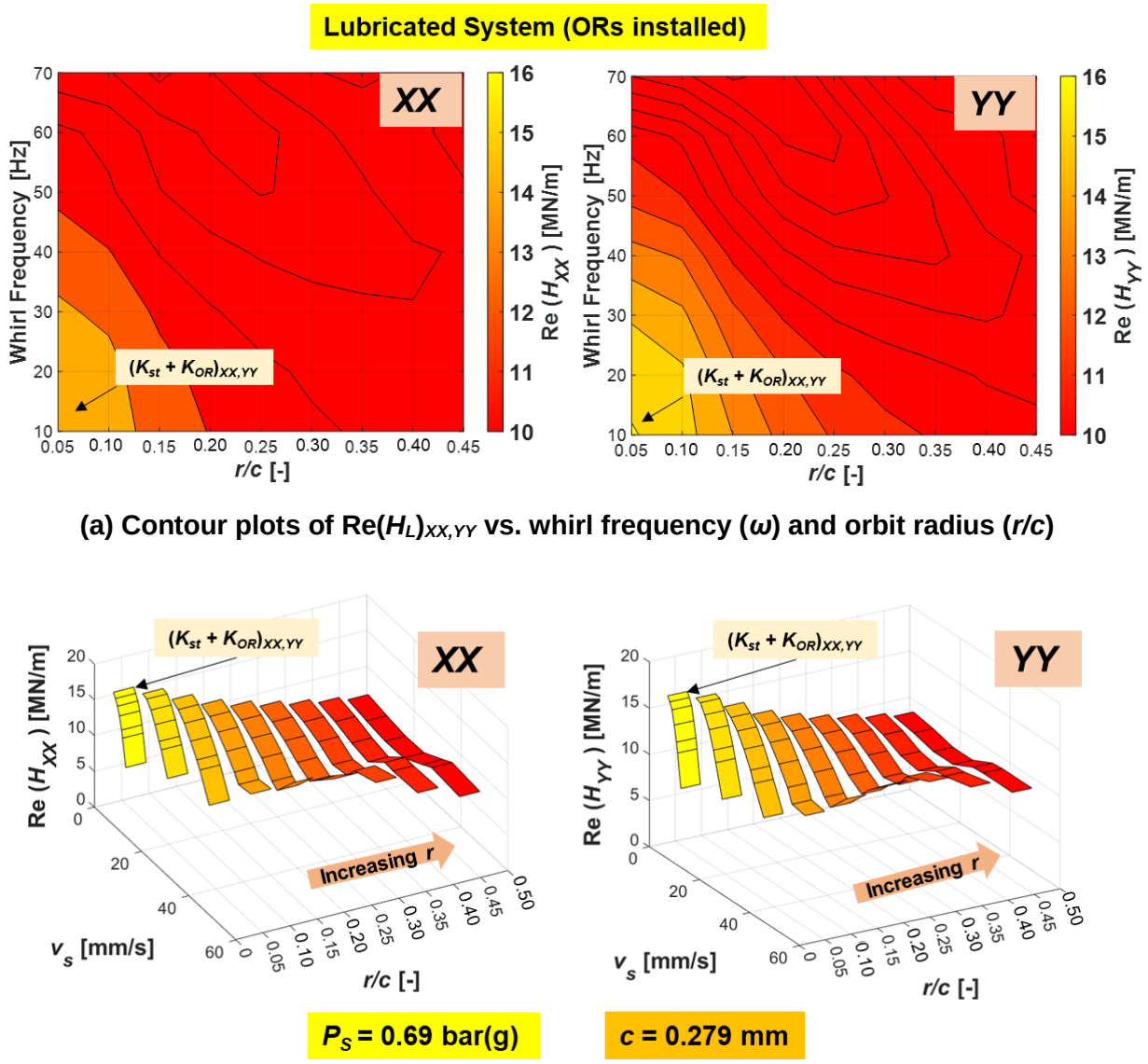

(a) Contour plots of Re(H_L)$_{XX,YY}$ vs. whirl frequency (ω) and orbit radius (r/c)

(b) Re(H_L)$_{XX,YY}$ vs. squeeze velocity (v_s) and orbit radius (r/c)

Figure 14. Lubricated structure + ORs. (a) Contour plots of (H_L)$_{XX,YY}$ vs. whirl frequency (ω) and orbit radius (r/c). (b) Re(H_L)$_{XX,YY}$ vs. squeeze velocity (v_s) and orbit radius (r/c). CCOs with radius r = 0.05c to 0.45c. Frequency range ω = 10 Hz to 70 Hz. P_S=0.69 bar(g).

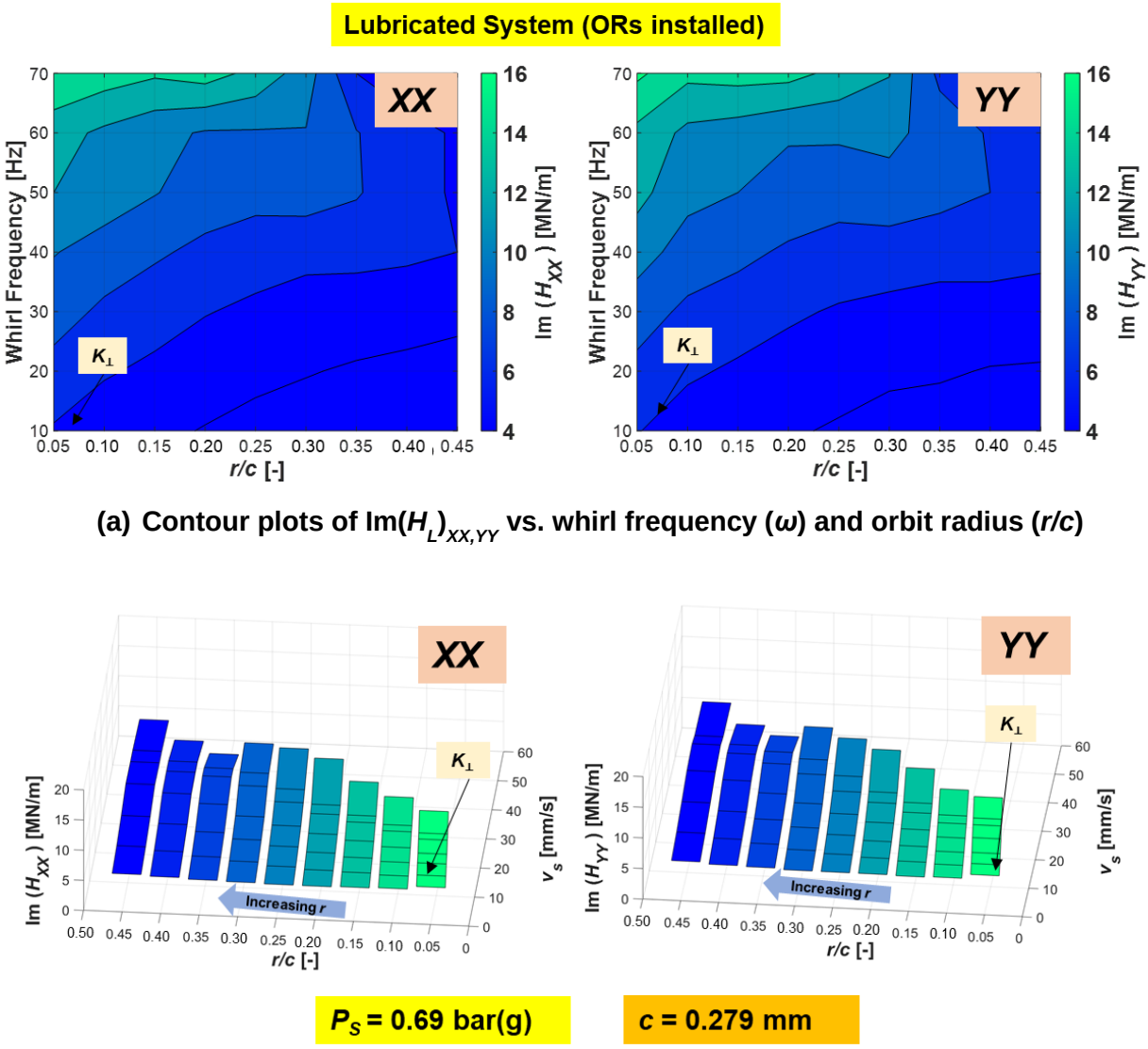

(a) Contour plots of Im(H_L)$_{XX,YY}$ vs. whirl frequency (ω) and orbit radius (r/c)

(b) Im(H_L) $_{XX,YY}$ vs. squeeze velocity (v_s) and orbit radius (r/c)

Figure 15. Lubricated structure + ORs. (a) Contour plots of (H_L)$_{XX,YY}$ vs. whirl frequency (ω) and orbit radius (r/c). (b) Im(H_L)$_{XX,YY}$ vs. squeeze velocity (v_s) and orbit radius (r/c). CCOs with radius r = 0.05c to 0.45c. Frequency range ω = 10 Hz to 70 Hz. P_S=0.69 bar(g).

Figures 16 and 17 depict the squeeze film direct complex dynamic stiffness, $\mathbf{H}_{SFD}$=($\mathbf{H}_L$-$\mathbf{H}_{st+OR}$). The symbols (squares and circles) denote test data, whereas the dotted lines represent the curve built with the estimated parameters using the physical model [Re(H_{SFD}) = ($K_{SFD} - \omega^2 M_{SFD}$), Im($H_{SFD}$)=($\omega C_{SFD}$)]. The estimation of the SFD stiffnesses spans a frequency range from ω=10 to

40 Hz, due to the decrease in the film added mass and viscous damping effects beyond v_s>24.5 mm/s.

Figure 16 shows the intercept of $\mathrm{Re}(H_{SFD})_{XX,YY}$ approaches 0 MN/m, confirming the squeeze film cannot generate a true static stiffness [1]. The decrease in $\mathrm{Re}(H_{SFD})_{XX,YY}$ as frequency increases shows significant SFD added masses for orbit radii from $r = 0.05c$ to $0.20c$. However, there is an increase in the magnitudes of $\mathrm{Re}(H_{SFD})_{XX,YY}$ at v_s=24.5mm/s, revealing a decrease in the film added mass effects. At the largest experimental squeeze velocities ($v_s \geq 34$ mm/s) $\mathrm{Re}(H_{SFD})_{XX,YY}$ ceases to decrease, reaching a nil magnitude as $\omega \rightarrow 70$ Hz.

Figure 17 shows $\mathrm{Im}(H_{SFD})_{XX,YY} = 0$ as $\omega \rightarrow 0$ Hz and later increasing as $\omega \rightarrow 70$ Hz for $r < 0.35c$, evidencing the dominant effects of viscous damping. Incidentally, Fig. 17 shows the magnitudes of $\mathrm{Im}(H_{SFD})_{XX,YY}$ drop at v_s>35 mm/s, denoting a rapid reduction in the film viscous damping effects. This reduction also contributes to selecting a shorter frequency range to identify the squeeze film damping coefficients.

Note the experimental cross-coupled complex dynamic stiffnesses have magnitudes at least one order lower than those reported in Figs. 16 and 17. See Appendix D for details on the measurements of $(H_L)_{XY,YX}$.

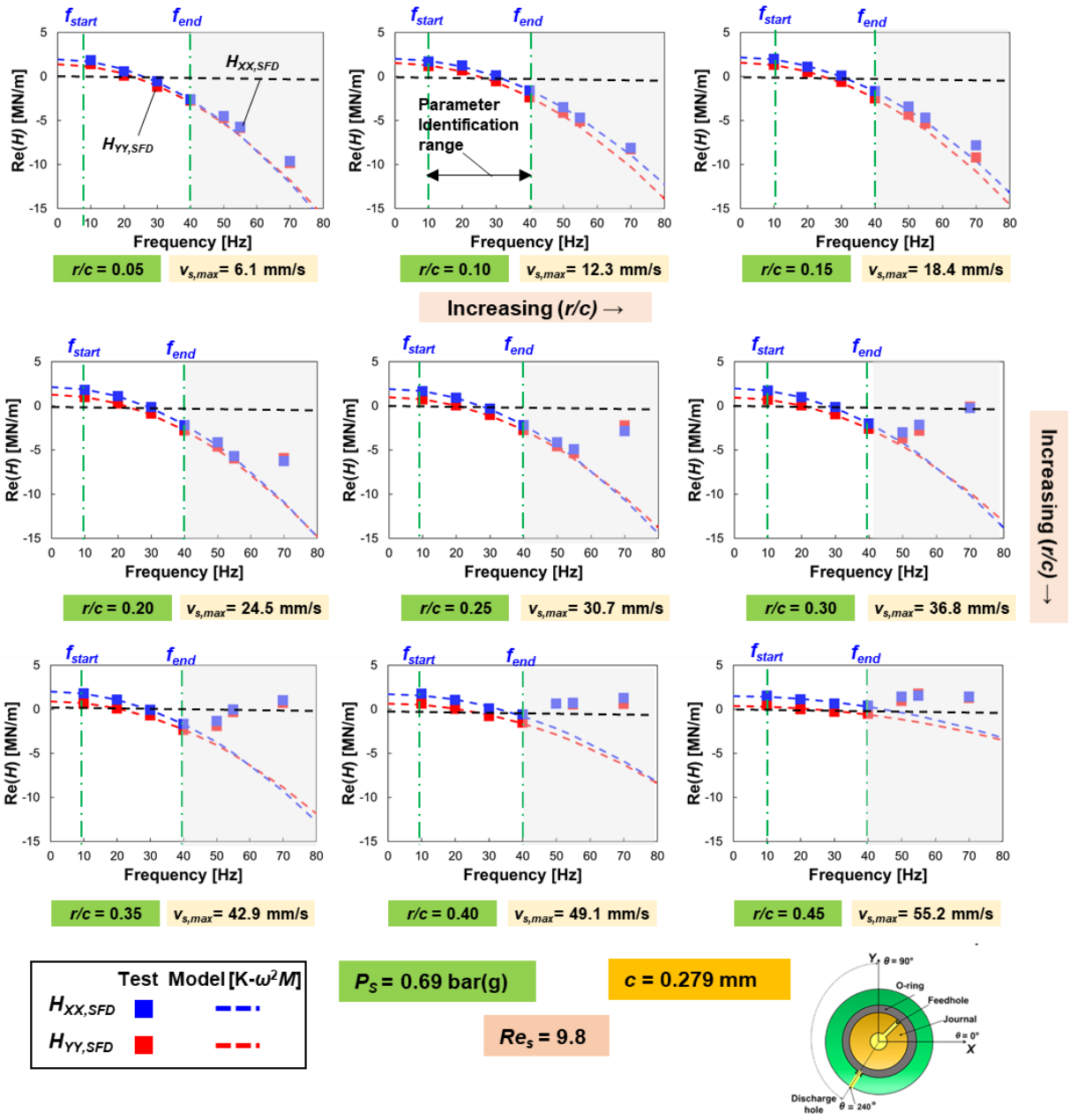

Figure 16. Real part of SFD $(H_{SFD})_{XX,YY}$ vs. whirl frequency (ω) for nine (r/c = 0.05 to 0.45) CCOs. P_S = 0.69 bar(g). Identification of parameters $(K,M)_{SFD}$ from ω= 10 – 40 Hz.

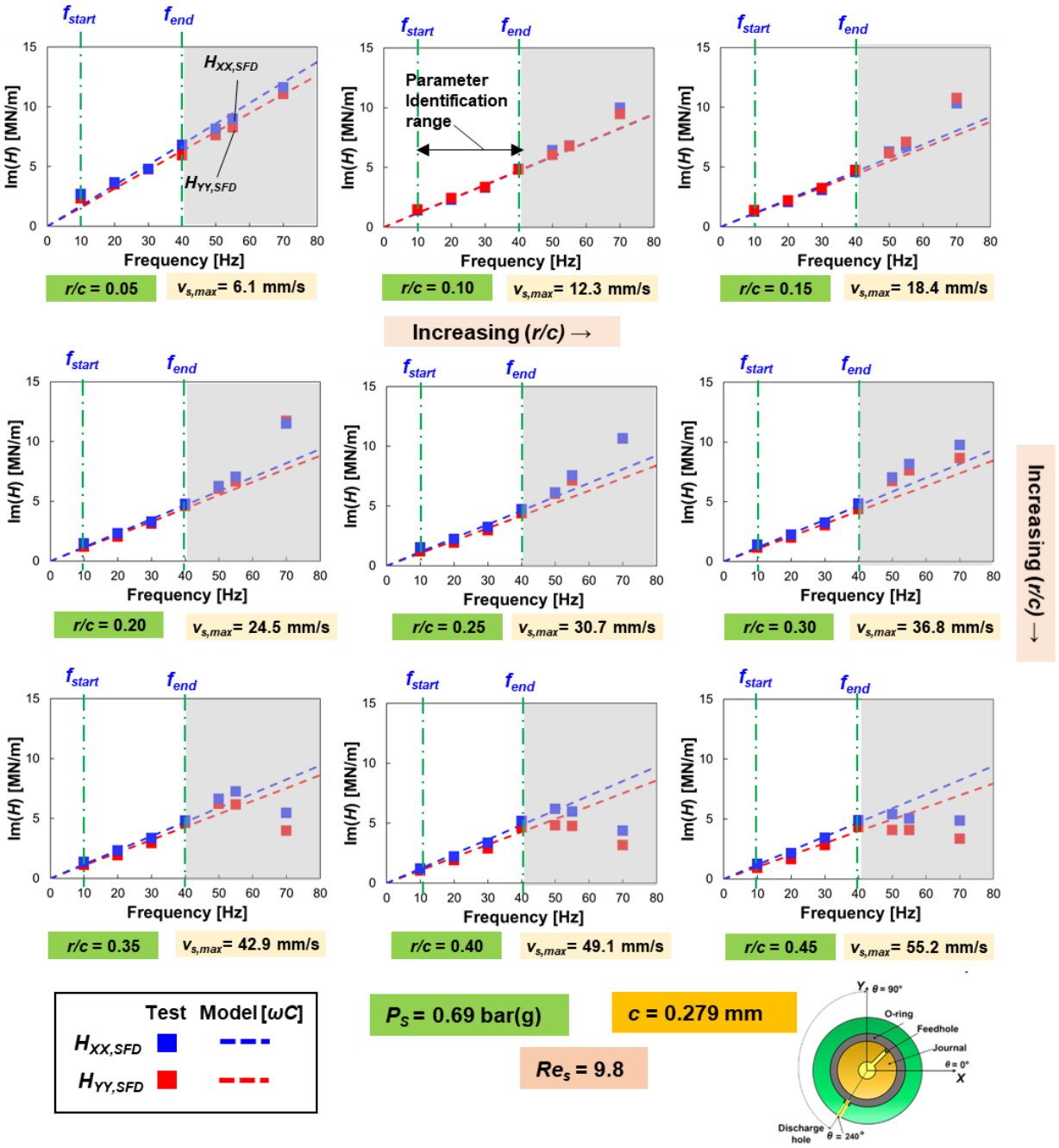

Figure 17. Imaginary part of SFD $(H_{SFD})_{XX,YY}$ vs. whirl frequency (ω) for nine (r/c = 0.05 to 0.45) CCOs. P_S = 0.69 bar(g). Identification of parameters $(C)_{SFD}$ from ω= 10 – 40 Hz.

Table 7 summarizes the squeeze film damping (C_{SFD}) and added mass coefficients (M_{SFD}) obtained from curve fits of the physical models [Re(H_{SFD}) →(K_{SFD} – $\omega^2 M_{SFD}$), Im(H_{SFD})→(ωC_{SFD})] to the measurements depicted in Figs. 16 and 17. Additionally, Table 7

presents magnitudes of R^2 from the identification of parameters. Do note the parameters in Table 7 are only valid over the frequency range ω = 10 Hz to 40 Hz.

The experimental parameters are slightly orthotropic with $C_{XX} \sim 1.05\ C_{YY}$ and $M_{XX} \sim 1.1\ M_{YY}$. The orthotropy is due to the location of the oil supply and discharge lines, which produce sources and sinks of flow, that likely distort the film dynamic pressure field and consequently, the SFD reaction forces [45].

As a reference to compare the identified SFD force coefficients, a tightly sealed SFD operating with small amplitude ($r \rightarrow 0$) circular centered orbits and no oil cavitation, produces viscous damping (C^*) and added mass (M^*) coefficients [1] equal to:

$$C^* = 12\pi\mu L\left(\frac{D}{2c}\right)^3 = 31.4\,\text{kN}\cdot\text{s/m};\ M^* = \rho\frac{\pi L}{c}\left(\frac{D}{2}\right)^3 = 58\,\text{kg} \tag{12}$$

The theoretical coefficients C^* and M^* are valid only for squeeze Reynolds numbers ($Re_S = (\rho\omega c^2)/\mu$) lower than 10 and operation with a full film (no oil cavitation or air ingestion). Presently, the maximum squeeze Reynolds number in the experiments Re_S = 9.8.

Figure 18 summarizes the normalized squeeze film damping ($\underline{C}=C_{SFD}/C^*$) and added mass coefficients ($\underline{M}=M_{SFD}/M^*$) showing error bars denoting the uncertainty in each parameter. Regarding the film damping coefficients shown in Fig. 19, their largest magnitudes occur at r = 0.05c, and $C_{SFD,avg} = \frac{1}{2}(C_{XX}+C_{YY})_{SFD}$, remains at nearly 90% of the theoretical magnitude C^* as the orbit radius grows to r = 0.25c. While C_{SFD} is constant for orbit radii r<30c, their magnitudes also reduce to $C_{SFD} \sim 0.6C^*$, as $r \rightarrow 0.45c$.

The test derived added mass coefficients presented in Fig. 18 are nearly equal to the theoretical inertia coefficient, $(M_{SFD})_{XX,YY} \sim M^*$ for r = 0.05c and 0.10c, as expected. In the range r = 0.05c to 0.25c M_{SFD} presents small changes with orbit size and within the uncertainty range in the

measurements. Hence the arithmetic mean of the added mass coefficients, $M_{SFD,avg}$= ½(M_{XX}+M_{YY})$_{SFD,}$ is constant as $r \rightarrow 0.25c$. Moreover, the SFD added masses for $r \leq 0.25c$, represent up to four times of the BC mass (15.6 kg). Next, the direct inertia coefficients for r = 0.30c reduce to ~0.8M^* and continue to decrease with increasing orbit amplitudes, a well-known effect predicted as early as 1985 in Ref. [53]. At the largest orbit radius (r = 0.45c) the added mass coefficients represent a mere 30% of the theoretical magnitude for a fully sealed damper (M^*) and nearly equal the BC mass.

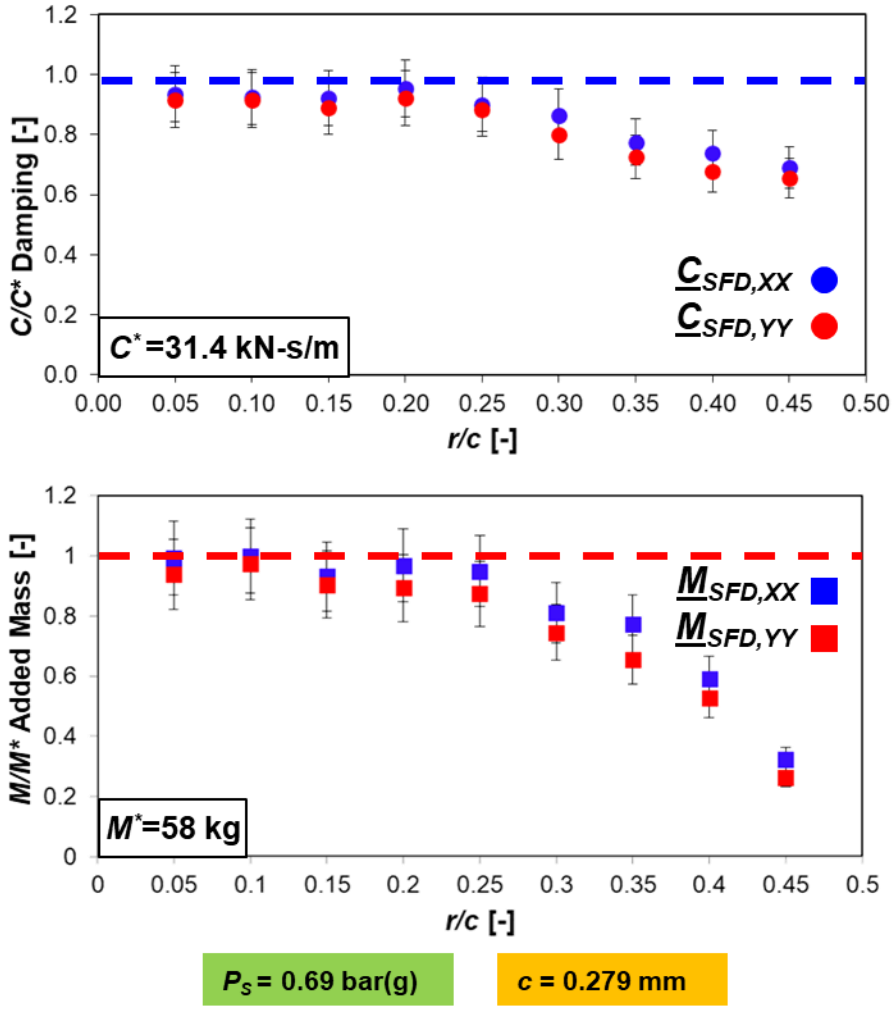

Figure 18. Experimentally identified normalized SFD force coefficients ($\underline{C}_{SFD}$, $\underline{M}_{SFD}$)$_{XX,YY}$ vs. orbit radius (r). Parameters estimated from CCOs and frequency range ω = 10 – 40 Hz. Supply pressure P_S=0.69 bar(g)

Table 7. Identified SFD physical parameters obtained from circular orbit tests. Direct parameters identified over the frequency range ω = 10 – 40 Hz. Orbit amplitudes from r = 0.05c to 0.45c

Orbit Radius r/c [-]	Added Mass M_{SFD} [kg]		R^2 [-]		Damping C_{SFD} [kN-s/m]		R^2 [-]	
	XX	*YY*	*XX*	*YY*	*XX*	*YY*	*XX*	*YY*
0.05	57.6 ± 6.4	54.4 ± 6.0	0.99	0.99	29.4 ± 2.2	28.8± 2.2	0.99	0.97
0.10	58.0± 6.5	56.5 ± 6.3	0.99	0.99	29.0 ± 2.1	28.7 ±2.2	0.98	0.99
0.15	54.0 ± 6.0	52.5 ± 5.9	0.99	0.99	28.9 ± 2.1	27.9 ± 2.2	0.98	0.98
0.20	56.2 ± 6.3	51.8 ± 5.7	0.99	0.99	29.9 ± 2.1	28.9 ± 2.2	0.98	0.98
0.25	55.1 ± 6.2	50.7 ± 5.6	0.99	0.99	28.3 ± 2.1	27.7 ± 2.2	0.98	0.97
0.30	47.1 ± 5.3	43.2 ± 4.8	0.99	0.99	27.2 ± 2.0	25.1 ± 2.0	0.99	0.98
0.35	44.9 ± 5.0	38.4 ± 4.3	0.99	0.99	24.2 ± 1.8	22.8 ± 1.8	0.97	0.99
0.40	34.3 ± 3.8	30.6 ± 3.4	0.98	0.96	23.2 ± 1.7	21.2 ± 1.7	0.97	0.98
0.45	18.7 ± 2.1	15.3 ± 1.7	0.90	0.92	21.7 ± 1.6	20.6 ± 1.6	0.99	0.99
Theoretical Coefficients	M^*=58 kg		N/A		C^*= 31.4 kN-s/m		N/A	

As a comparison between the damping coefficients in the pair ORs and the lubricated system (C_L=C_{OR}+C_{SFD}), Figure 19 presents the magnitudes of C_{OR}/C_L vs. orbit radius. Note C_{OR} and C_L depicted in Fig. 19 represent the arithmetic mean $C_{OR,\text{avg}}$= ½ ($C_{OR,XX}$+$C_{OR,YY}$) and $C_{L,avg}$ = ½ ($C_{L,XX}$+$C_{L,YY}$). The contribution of the ORs' damping to the lubricated system damping is nearly 10% at r = 0.05c and 0.10c. However, the ratio C_{OR}/C_L, also decreases considerably, and reaches only 3% of the whole system damping as $r \rightarrow$ 0.45c.

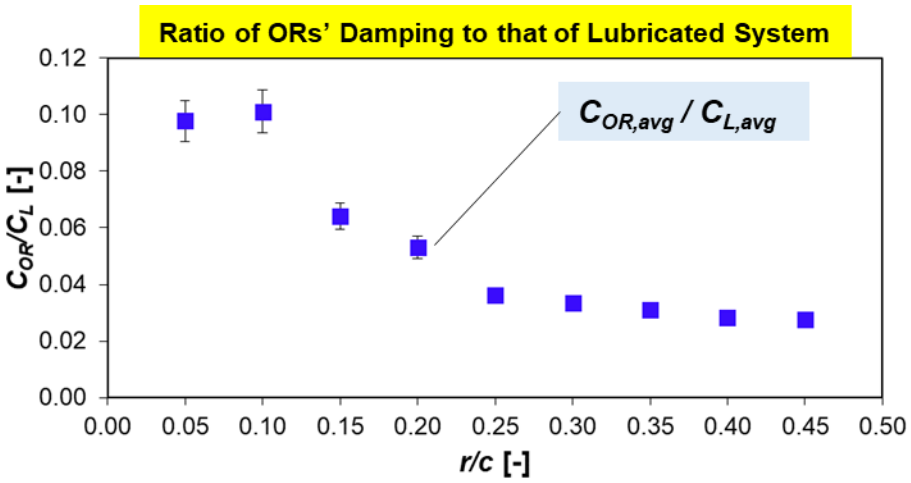

Figure 19. Ratio of ORs' damping to lubricated system damping vs. orbit radius (*r/c*). Lubricated test system supplied with P_S = 0.69 bar(g). Experimentally estimated parameters from CCOs and frequency range ω = 10 – 40 Hz.

Comparison of experimental force coefficients to an orbit analysis physics model

An orbit analysis physics model [47][8], predicts squeeze film added mass and damping coefficients. The model solves the modified Reynolds equation for the squeeze film and calculates instantaneous reaction forces at a specified orbit amplitude for multiple instances during a complete orbit of the journal center. Then, the computer program repeats this process over the same range of whirl frequencies, to produce a matrix of complex stiffnesses $\mathbf{H}_{SFD.}$ Just as in the experiments, the prediction model delivers force coefficients over the frequency range as

$$\mathbf{H}_{SFD} \rightarrow \left[\mathbf{K}_{SFD} - \omega^2 \mathbf{M}_{SFD} + i\ \omega\ \mathbf{C}_{SFD} \right] \tag{13}$$

Note the predictions using the orbit model deliver identical force coefficients, that is, C_{XX}=C_{YY} and M_{XX} = M_{YY}. Additionally, the physical model assumes a fully sealed damper. Figure 20 depicts the experimentally derived normalized damping ($\underline{C}$=C_{SFD}/C^*) and added mass coefficients ($\underline{M}$=M_{SFD}/M^*), along with the predicted added damping ($\underline{C}_{SFD}$) and mass terms ($\underline{M}_{SFD}$) vs. orbit

[8] Present results procured by Dr. Bonjin Koo based on Ref [47]

radius. Additionally, Fig. 20 depicts prior experimental force coefficients reported by San Andrés and Koo in Ref. [45] and San Andrés and Rodríguez in Ref. [46].

The predicted damping coefficients agree very well with the experimental ones in almost all cases. For small orbit amplitudes ($r \leq 0.25c$), the physics model shows a mean difference of 10% between the experimental results and the predictions. For $r \geq 0.25c$, Fig. 20 shows as the predictions barely reach the upper bound of the experimental uncertainty in the damping coefficients and show a mean difference of 13%. With respect to the added mass coefficients the predictions show a mean difference of 4% for $r \leq 0.25c$. For $0.25c \leq r \leq 0.45c$, the predicted mass terms are on average, 5% larger than the experiments, and at $r = 0.45c$, $M_{SFD} \sim 0.85\underline{\underline{M}}_{SFD}$. Only for ($r = 0.45c$), the model overpredicts the experimental added masses by 15%. It is worth recalling both the experimental identification and the orbit simulation span a reduced frequency range for the estimation of force coefficients, ω =10 to 40 Hz.

The current experimental findings agree with prior results presented by San Andrés and Rodríguez in Ref. [46]. Refs. [45, 46] state the ORs' damping accounts for 10% of the lubricated system for whirl orbit amplitudes up to r=0.20c. Nevertheless, the results depicted in Fig. 20 show the contribution of damping in the ORs to the system only represents ~10% of the system damping at $r = 0.05c$ and $0.10c$, and later decreases as the orbit radius increases.

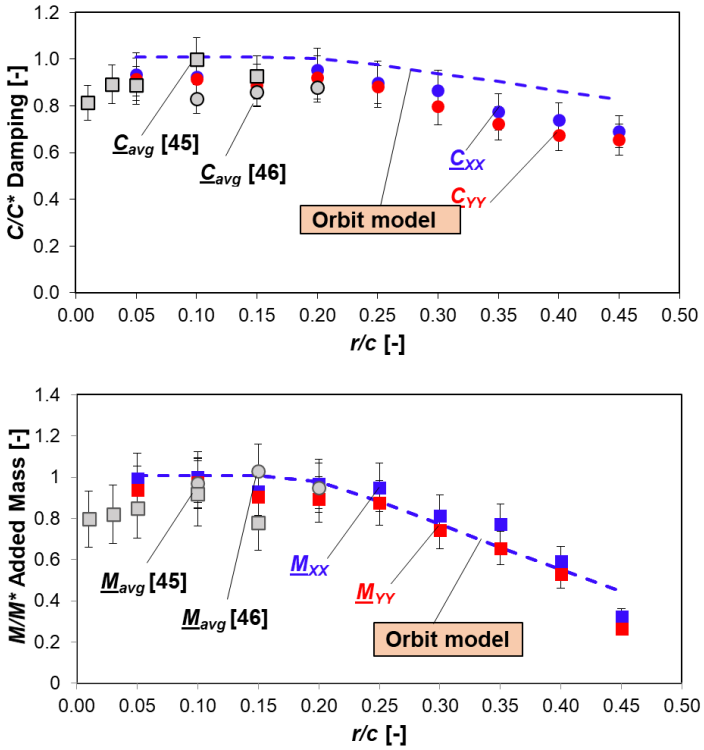

Figure 20. Normalized experimental damping ($\underline{C}_{SFD}$) and inertia ($\underline{M}_{SFD}$) coefficients vs. orbit radius (r/c). P_S = 0.69 bar(g). Experiments from CCOs and frequency range ω = 10 – 40 Hz. Comparison with experimental results in Refs. [45, 46] and results from predictive model in Ref. [47]

The test results reported in Ref. [45] employ ORs with similar characteristics as the current ones. The tests span orbit amplitudes r=0.01c to 0.15c. The damper used in Ref. [45] operates with a single feedhole, slenderness ratio L/D= 0.2 and ISO VG 2 lubricant at P_S= 0.69 bar(g). However, for the OR-SFD in Ref. [45], c = 0.373 mm. In Ref. [46], the authors perform dynamic load tests with amplitudes r=0.10c - 0.20c and employ an OR-SFD identical in geometry to the present one; supplied with ISO VG 2 oil at P_S= 0.69 bar(g). As seen in Fig. 20, prior and current experimental results correlate well. The normalized damping (C_{SFD}) and added mass (M_{SFD}) shown in Ref. [45] both vary in average by 10% with respect to the current results and are within the uncertainty range of the force coefficients (U_C=8.0%, U_M=11.1%; see Appendix C). Regarding the estimated

parameters from Ref. [46], C_{SFD} and M_{SFD} only differ on average by 5% and 6%, respectively with respect to the current magnitudes.

CHAPTER VIII
PRESSURE MEASUREMENTS IN O-RINGS SEALED SFD

This chapter presents measurements of the dynamic pressure generated in the squeeze film land while the damper operates under periodic whirl orbits, plus amplitude of peak-to-peak dynamic pressures, both in the film land and in the upstream plenum. Recall the piezoelectric pressure transducer recording the pressure is located 225^o away from the X axis, and at z = 0, whereas the transducer measuring the plenum pressure sits atop the journal sleeve, see Fig. 3. Prior to the dynamic load experiments, a lubricant pressurization test into the damper film land, up to P_S~7 bar, verifies the O-rings do not allow for any leakage under a static condition (no bearing motion). Additionally, a pressurization air test with the journal uninstalled from its pedestal shows the mechanical check valve does not allow for backflow under static pressure conditions.

Measurements of dynamic pressure in the damper film land and plenum

Figures 21, 23 and 25 show recorded pressure profiles in the film land (θ=225^o, z= 0) for tests corresponding to data for circular centered orbits with r = 0.05c to 0.45c, and whirl frequencies ω = 50, 55 and 70 Hz, respectively (v_s=4 mm/s to 55 mm/s). Each figure depicts a cascade plot showing film dynamic pressures (P) at either ω = 50, 55 or 70 Hz, and for orbit amplitudes from r=0.05c to 0.45c during three whirl periods of motion (T=2π/ω). Note Diaz, in Refs. [54-57] first presented squeeze film dynamic pressures in this form. The cascade plots in Figs. 21, 23 and 25 also depict measurements of film thickness (h) and film time rate of change ($-\partial h/\partial t$) at the location of the pressure measurements for operation r=0.45c. Figures 22, 24 and 26 (a) depict contour plots of the corresponding film dynamic pressure measurements. Do note the graphs depict magnitudes of gauge pressure (not absolute). Figs. 22, 24 and 26 (b) show average peak-to-peak (pk-pk)

pressures for three periods of motion vs. orbit radius (r/c) for the pressure measurements depicted in Figs. 21, 23 and 25, along with error bars that denote the variability in the measurements.

Figure 21 (a) depicts continuous pressure profiles at $\omega = 50$ Hz for small amplitudes of motion ($r < 0.25c$, v_s=22 mm/s), discarding the occurrence of either air ingestion or gaseous cavitation. Seen in Figs. 21, 23 and 25 (b), the film thickness increases (producing a positive squeeze), as the film generates a positive pressure and reaches a maximum magnitude (P_{max}) just as the film rate of change reaches a minimum ($\partial h/\partial t \rightarrow$ min.). Then, as the film thickness increases, or a negative squeeze is produced, the film pressure decreases. On the other hand, the dynamic pressures reach a minimum approximately as the film time rate of change reaches its largest magnitude ($\partial h/\partial t > 0$).

For larger orbit amplitudes, the pressure profiles begin to distort and present high frequency spikes. The quick pressure surges, marked by red circles in Fig. 21 (a) likely show the collapse of air bubbles inside the film land when a negative squeeze action occurs, hence evidencing the presence of air in the film land.

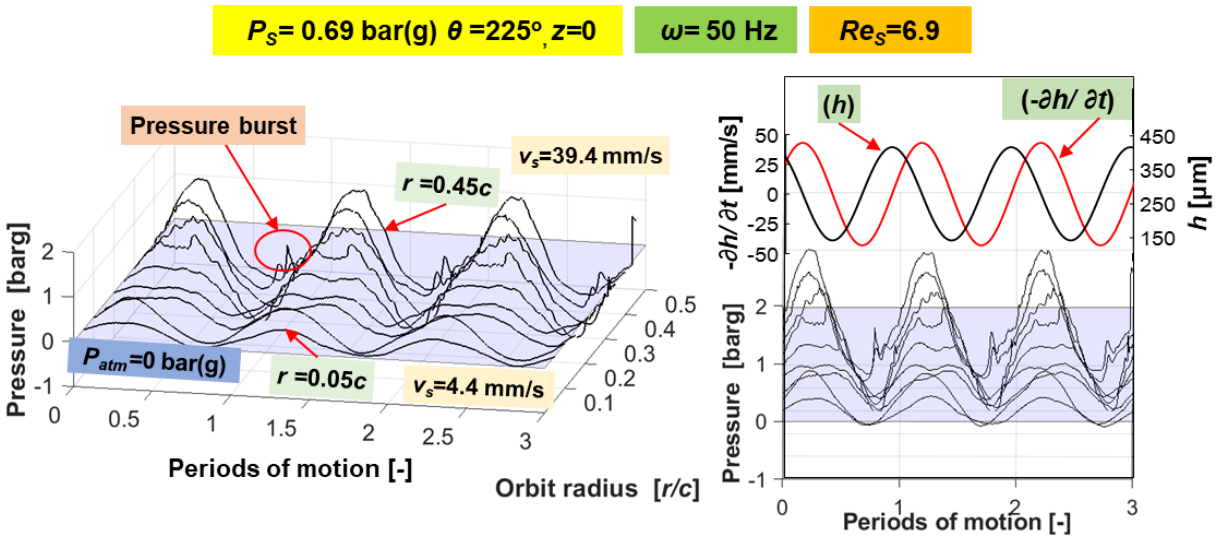

(a) Cascade plot of dynamic pressures for ω=50 Hz: isometric view

(b) Cascade plot of dynamic pressures, film thickness (h) and film rate of change $(-\partial h/\partial t)$ for r=0.45c and ω=50 Hz

Figure 21. Cascade plot of squeeze film dynamic pressure measurements. Dynamic pressure (P) vs. orbit radius (r/c) for three whirl periods of motion: (a) isometric view and (b) front view. Circular whirl orbits with frequency ω = 50 Hz and orbit radius r = 0.05c to 0.45c.

The contour plot in Fig. 22 (a) shows the peak-peak pressures steadily increase with orbit radius and, similarly, Fig. 22 (b) depicts the pressure amplitudes grow as the orbit radius increases. For r > 0.30c, the maximum dynamic pressures P_{max} ~ 1 bar(g), and the minimum magnitudes extend below ambient P_{min}~-1 bar(g).

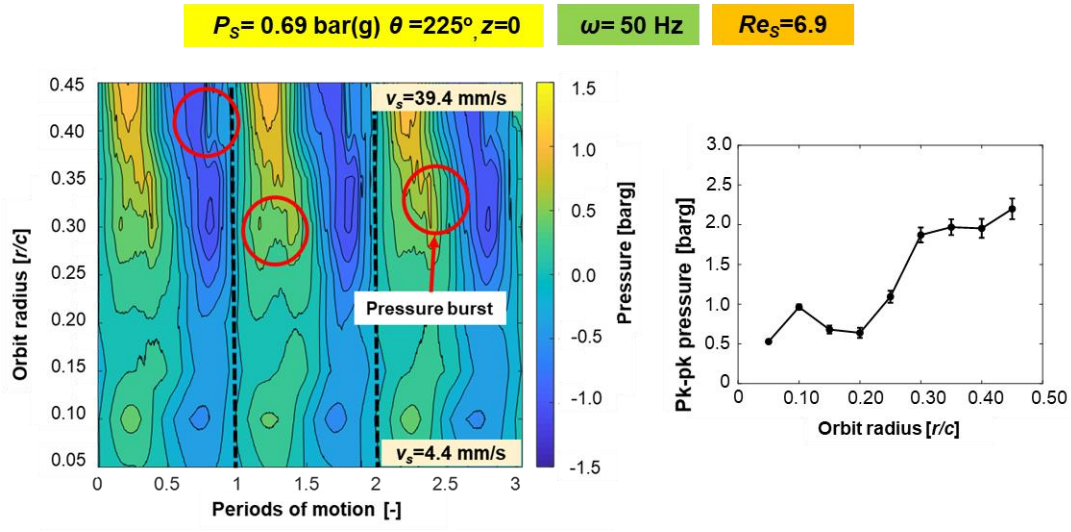

(a) Contour plot of dynamic pressures

(b) Average peak-peak pressures vs. orbit radius (*r/c*)

Figure 22. Squeeze film dynamic pressure measurements. (a) Contour plot of film dynamic pressures (*P*) vs. orbit radius (*r/c*) for three whirl periods of motion. (b)Average peak-peak film pressures vs. (*r*/c). Circular whirl orbits with frequency *ω* = 50 Hz and orbit radius *r* = 0.05*c* to 0.45*c*.

Regarding the pressure measurements depicted in Fig. 23 and obtained at ω = 55 Hz, the incidence of pressure bursts for $r > 0.25c$ ($v_s > 24$ mm/s) occurs as the film thickness increases (during a negative squeeze film action). In addition, the shapes of the pressure profiles in Fig. 23 continue to distort as the orbit radius increases beyond r=0.35c. Additionally, the nearly flat pressure zone, visible in Fig. 23 (a) and for r =0.45c, evolves around the location of maximum film thickness and occurring on each half-period of negative squeeze motion. The behavior is common in open ended SFDs operating at large orbit amplitudes, reported in Refs. [55-57], a flat zone in the dynamic pressure indicates lubricant vaporization, whereas a sudden pressure increases occurs due to the collapse of (ingested) air bubbles.

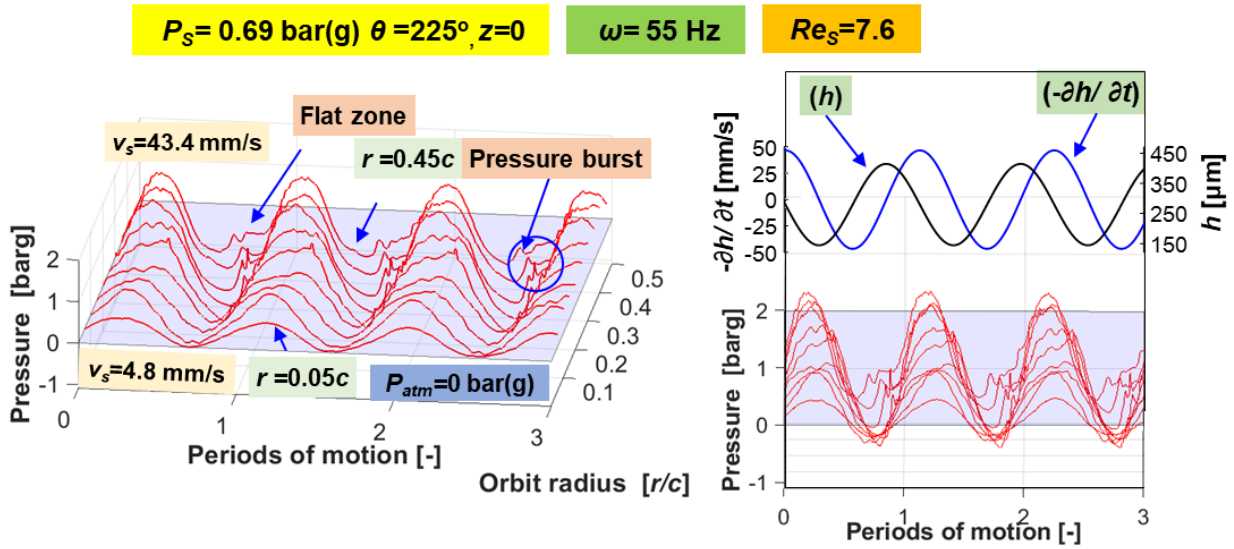

(a) Cascade plot of dynamic pressures for ω=55 Hz: isometric view

(b) Cascade plot of dynamic pressures, film thickness (h) and film rate of change $(-\partial h/\partial t)$ for r=0.45c and ω=55 Hz

Figure 23. Cascade plot of squeeze film dynamic pressure measurements. Dynamic pressure (P) vs. orbit radius (r/c) for three whirl periods of motion: (a) isometric view and (b) front view. Circular whirl orbits with frequency ω = 55 Hz and orbit radius r = 0.05c to 0.45c.

Incidentally, the contour plot in Fig. 24 (a) shows the location of the pressure bursts occur at pressure magnitudes below ambient pressure. The measurements in Fig. 24 (b) depict an increase in peak-to-peak pressure amplitudes as the squeeze velocity grows for amplitudes lower than r = 0.25c. Nonetheless, this increase stagnates at r=0.40c (v_s=39 mm/s), as seen in Fig. 22 (b), showing the increasing gas content in the film prevents the generation of a dynamic pressure proportional to the squeeze velocity for r=0.45c (v_s=43 mm/s).

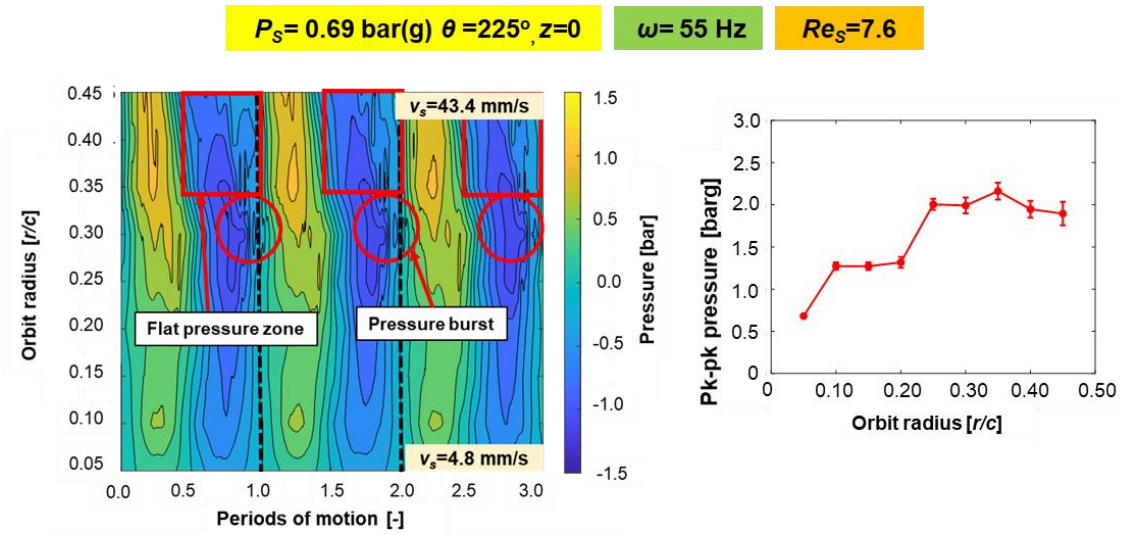

(a) Contour plot of dynamic pressures

(b) Average peak-peak pressures vs. orbit radius (*r/c*)

Figure 24. Squeeze film dynamic pressure measurements. (a) Contour plot of film dynamic pressures (*P*) vs. orbit radius (*r/c*) for three whirl periods of motion. (b)Average peak-peak film pressures vs. (*r/c*). Circular whirl orbits with frequency ω = 55 Hz and orbit radius *r* = 0.05*c* to 0.45*c*.

Figure 25, depicting pressure profiles at ω=70 Hz and r = 0.05c to 0.45c (v_s=6 mm/s to 55 mm/s) shows similar features as those in Figs. 21 and 23. In particular, Fig. 25 depicts flat pressure zones as the film thickness reaches its largest amplitude for $r > 0.25c$, characteristic of lubricant vaporization. Figure 26 shows the peak-to-peak amplitudes in the profiles enlarge as v_s increases for $r \leq 0.30c$ ($v_s \leq$ 37 mm/s). For $r > 0.30c$ (v_s=37 mm/s), the peak-peak pressure amplitudes cease to increase, likely prevented by the gas content in the film land beyond v_s=37 mm/s.

While the elastomeric seals perfectly seal the damper under a static condition and low squeeze velocities (v_s<20 mm/s), the pressure measurements indicate the seals permit air through flow into the film land at squeeze velocities as low as v_s= 24.5 mm/s (Re_S= 9.8).

As indicated in the identification of O-rings' force coefficients, their stiffness and damping parameters substantially decrease for $r \geq 0.25c$, an orbit amplitude where air ingestion is evident.

The degradation of the ORs' restorative forces at moderately large orbit amplitudes, coupled with a low lubricant feed pressure can only set the appropriate conditions for air ingestion to occur.

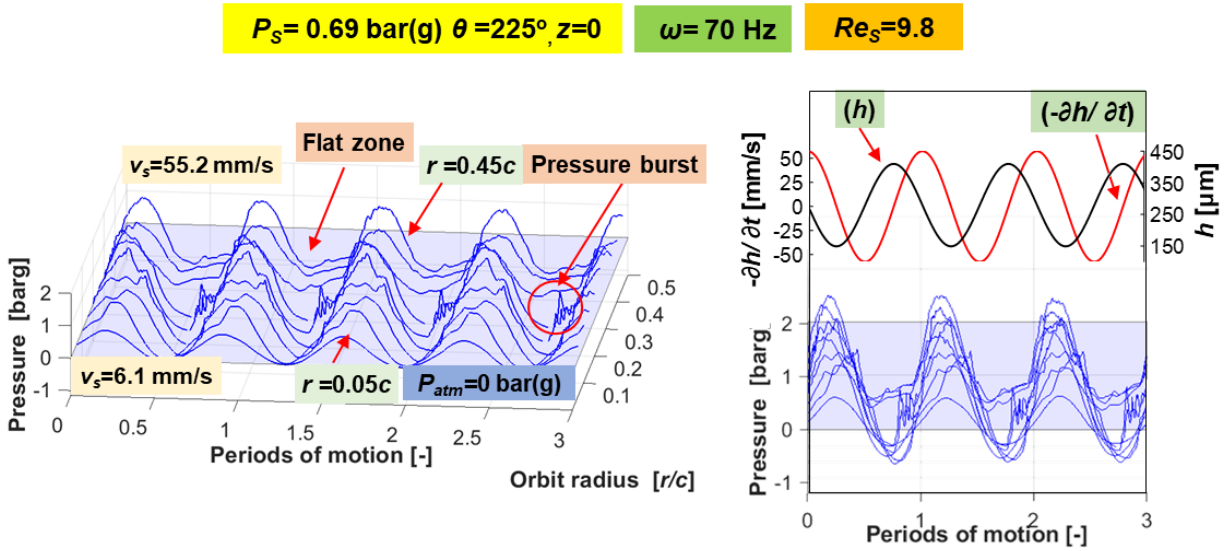

(a) Cascade plot of dynamic pressures for ω=70 Hz: isometric view

(b) Cascade plot of dynamic pressures, film thickness (h) and film rate of change (-$\partial h/\partial t$) for r=0.45c and ω=70 Hz

Figure 25. Cascade plot of squeeze film dynamic pressure measurements. Dynamic pressure (P) vs. orbit radius (r/c) for three whirl periods of motion: (a) isometric view and (b) front view. Circular whirl orbits with frequency ω = 70 Hz and orbit radius r = 0.05c to 0.45c.

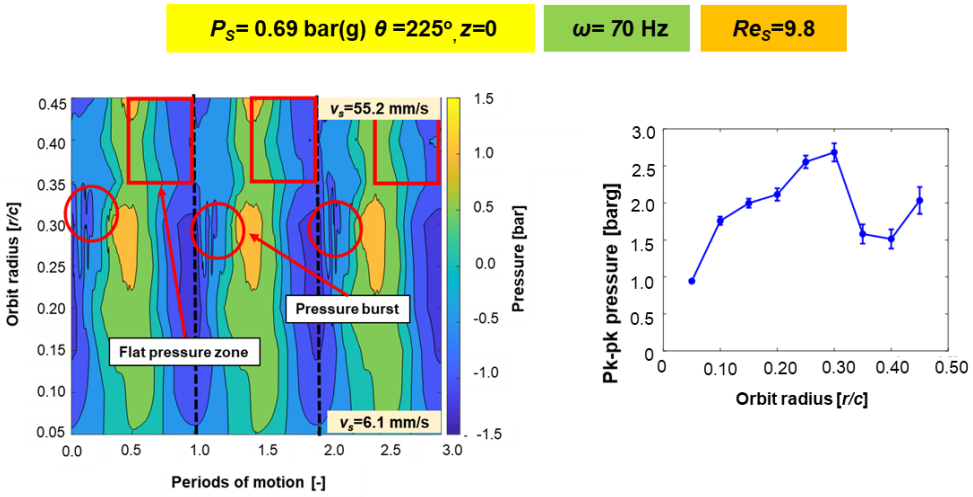

(a) Contour plot of dynamic pressures

(b) Average peak-peak pressures vs. orbit radius (*r/c*)

Figure 26. Squeeze film dynamic pressure measurements. (a) Contour plot of film dynamic pressures (*P*) vs. orbit radius (*r/c*) for three whirl periods of motion. (b)Average peak-peak film pressures vs. (*r*/c). Circular whirl orbits with frequency ω = 70 Hz and orbit radius *r* = 0.05*c* to 0.45*c*.

Figure 27 shows measurements of dynamic pressure inside the journal plenum for orbit amplitudes r=0.15c, 0.20c. 0.30c and 0.45c vs. increasing whirl frequency and over 0.2 seconds. For $\omega <$ 40 Hz, the pressures inside the plenum are nil. However, as $\omega \rightarrow$70 Hz, for all orbit amplitudes shown, the pressure amplitudes begin to increase, showing a periodic waveform, confirming the incidence of lubricant backflow even with a check valve installed. The amplitudes of dynamic pressure become so significant for ω=70 Hz that they reach a maximum pressure of ~0.2 psi(g), (see Figs. 27 c and d), although they are one order of magnitude lower than those in the film land. Incidentally, the plenum pressures also appear distorted as the whirl frequency increases (see Fig. 27 b), and exhibit pressure bursts likely denoting the presence of gas that migrated to the plenum and could also make the contents of the plenum compressible.

More importantly, the measurements show that for whirl frequencies larger than ω= 40 Hz, the pressure fluctuations defy the assumption that the lubricant feeding the squeeze film land through

the journal feedhole is a constant stream. Hence, for certain operating conditions, the location of the lubricant feedhole should also be considered as a contributor of a dynamic pressure in the film land.

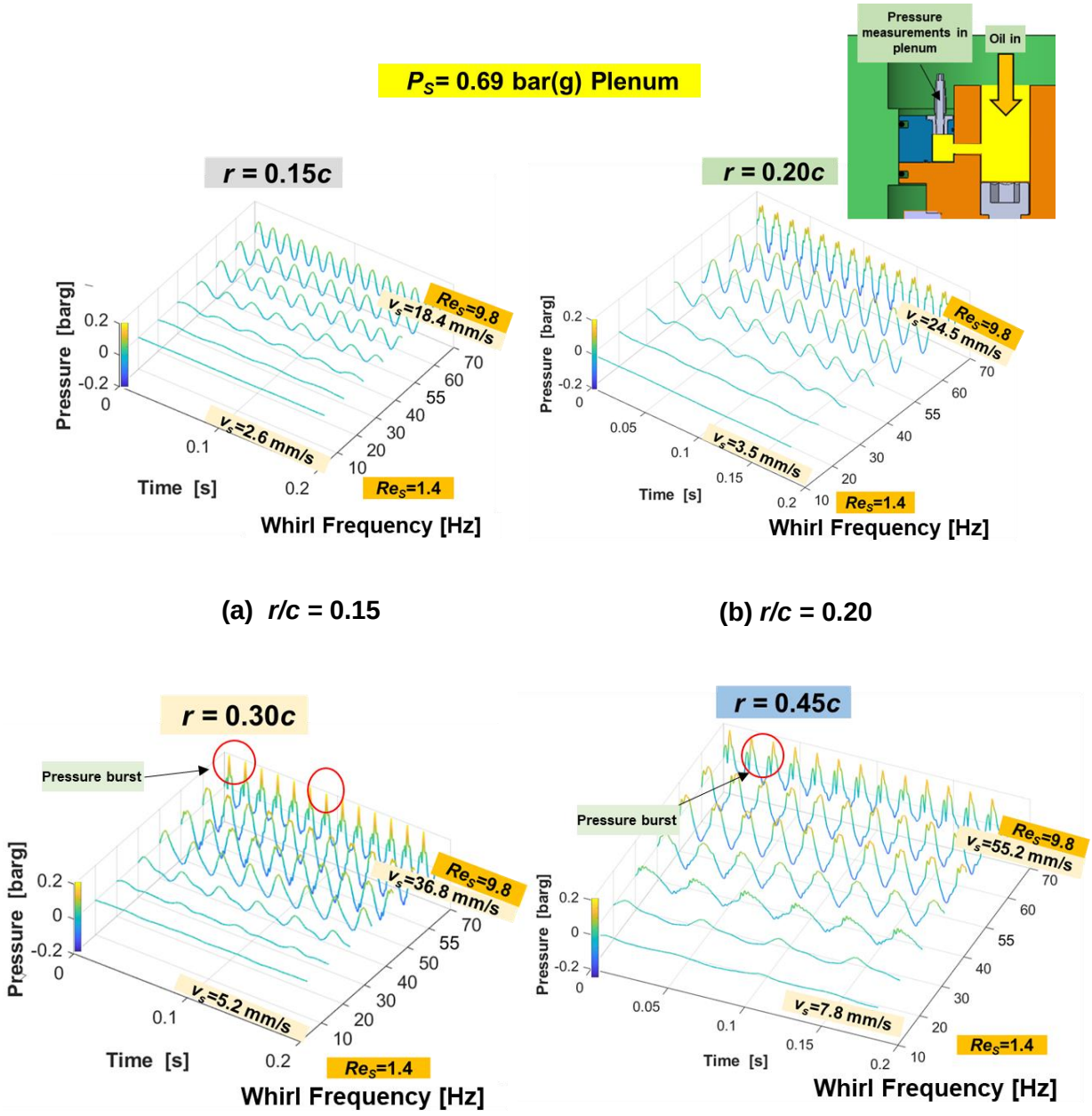

(a) *r/c* = 0.15 **(b) *r/c* = 0.20**

(c) *r/c* = 0.30 **(d) *r/c* = 0.45**

Figure 27. Measured dynamic pressures in upstream plenum vs. whirl frequency (*ω*) and time. (a) *r* =0.15*c*, (b) *r* =0.20*c*, (c) *r* =0.30*c* and (d) *r* =0.45*c*. CCOs with ω = 10 Hz to 70 Hz and *r* = 0.05*c* to 0.45*c*.

Peak-to-peak pressures in the damper film land and upstream plenum

Figure 28 displays the dynamic peak-peak pressures ($P_{pk\text{-}pk}$) in the film land at θ=225^o vs squeeze velocity (v_s). Figure 29 shows normalized peak-peak pressures (P^*) against v_s. A simple dimensional analysis of Reynolds equation [54] delivers

$$P^* = \frac{P_{pk-pk}}{\mu v_s}\left(\frac{c^2}{R}\right) \tag{15}$$

The measurements include error bars representing the variability in the dynamic pressures acquired over 0.25s, indicating every period of motion produces a unique pressure profile. The measured peak-peak pressures increase with frequency (ω) and with orbit radius (r/c) for orbit amplitudes lower than r=0.35c, as depicted on the left side of Fig. 28. Nonetheless, for r≥0.35c, the peak-peak pressures increase with squeeze velocity but remain nearly constant at ω=55 Hz (v_s>33 mm/s), and decrease at ω=70 Hz (v_s>43 mm/s). The peak pressures at the three largest orbit amplitudes (r=0.35c to 0.45c) and at ω = 50 Hz to 70 Hz (33 mm/s<v_s 55.2 mm/s), show the film does not produce a dynamic pressure proportional to squeeze velocity due to the presence of air and vapor cavitation in the film land. This effect is accompanied by the decrease in viscous damping forces at the same orbit amplitudes and frequencies, as depicted in Fig. 17.

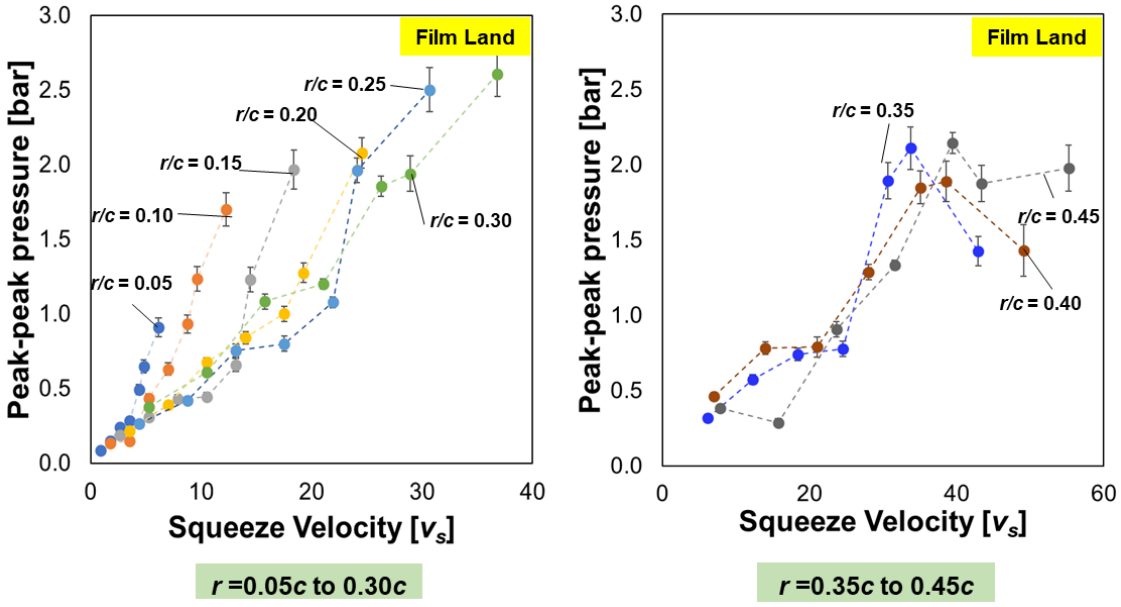

Figure 28. Peak-to-peak pressures ($P_{pk\text{-}pk}$) in squeeze film land vs. squeeze velocity (v_s). Measurements conducted at θ=225° and z=0. CCOs with ω = 10 Hz to 70 Hz and r = 0.05c to 0.45c.

Figure 29 reveals the largest normalized magnitudes of peak pressure occur at orbit amplitudes r=0.05c to 0.15c. For orbit amplitudes r<0.35c and for whirl frequencies ω<50 Hz (v_s<31 mm/s), the normalized peak pressures remain relatively constant. Incidentally, the normalized pressures show similar trends as $P_{pk\text{-}pk}$, and for 0.35c≤r≤0.45c, also show a downward trend with increasing whirl frequency.

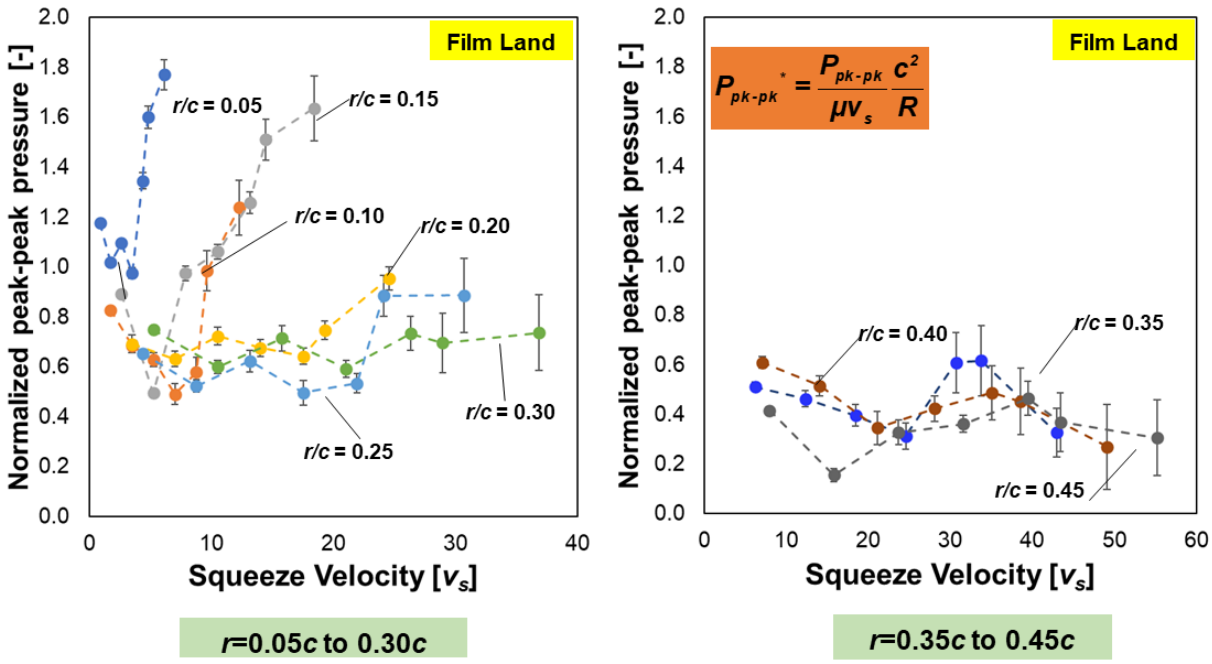

Figure 29. Normalized peak-to-peak pressures ($P^*_{pk\text{-}pk}$) in squeeze film land vs. squeeze velocity (v_s). Measurements conducted at θ=225° and z=0. CCOs with ω = 10 Hz to 70 Hz and r = 0.05c to 0.45c.

Figure 30 displays peak-peak dynamic pressure measurements ($P_{pk\text{-}pk}$) in the oil upstream plenum. The peak-peak dynamic pressures are practically nil at r= 0.05c to 0.15c throughout the entire range of squeeze velocities. Nonetheless, for 0.20c≤r≤0.30c, the peak-peak measurements depict an upward trend and represent nearly 15% to 25% of the pressure magnitudes recorded in the film land. Moreover, the peak-peak pressure amplitudes in the plenum increase so significantly, that they reach ~45% of the lubricant feed pressure as v_s→37mm/s (ω→70 Hz) for r= 0.30c. The plenum pressure measurements also attest for the incidence of lubricant backflow through the journal check valve. Additionally, for r=0.20c to 0.45c, Fig. 30, shows the peak-peak pressures in the plenum follow the same trend as in the measurements in the film land, shown in Fig. 28, also revealing the presence of gas in the plenum. Hence, causing a decline in pk-pk pressure for v_s > 40mm/s.

After finalizing the experiments, another set of pressure tests verifies the operation of both the O-ring seals and the mechanical check valve after the experiments with dynamic loads. Under a static condition, the elastomeric seals do not allow for lubricant side leakage and the check valve allows flow in one direction only.

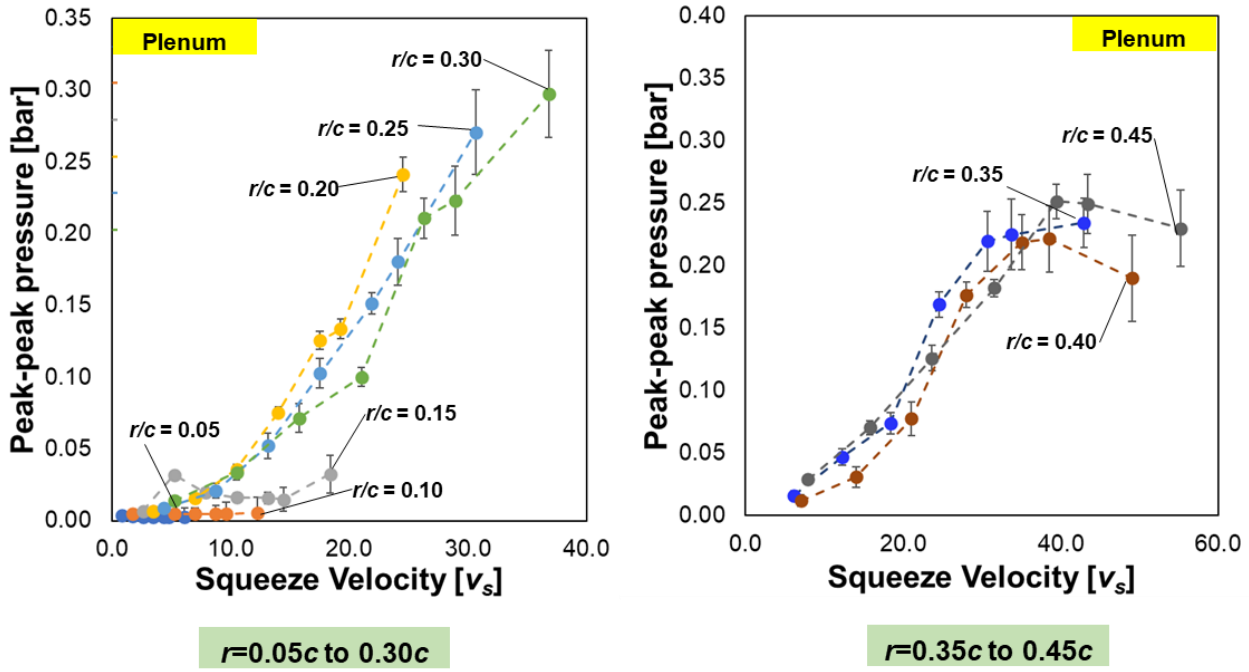

Figure 30. Peak-peak dynamic pressures in upstream plenum ($P_{pk\text{-}pk}$) vs. squeeze velocity (v_s). Measurements conducted at θ=225° and z=0. CCOs with ω = 10 Hz to 70 Hz and r = 0.05c to 0.45c.

CHAPTER IX

ESTIMATION OF GAS VOLUME FRACTION IN O-RINGS SEALED DAMPER

In a separate set of experiments, a series of videos and photographs record the operating test rig to identify the onset of air entrainment in the film land. The hyperlink https://youtu.be/R5WPD6t1fWs depicts the SFD test rig operating at r= 0.25c, 0.35c, 0.40c and 0.45c, at ω = 70 Hz. Originally yellow in color, the lubricant is dyed blue to visualize air bubbles more easily. Additionally, a ball valve installed 315^o away from the X axis, L = 0 (midplane) and diameter ϕ_{out}=4.50 mm allows to bleed lubricant from the damper film land. While a direct view of the damper film land is not possible, the video graphic records depict the damper discharge line and the top sealed end at multiple operating conditions.

Figure 31 depicts the lubricated system operating at r = 0.20c and ω = 70 Hz, corresponding to v_s=24.5 mm/s and a squeeze Reynolds number Re_S=9.8. During the operation of the damper at $v_s \leq$ 24.5 mm/s, the top journal sealed end shows no lubricant side leakage (through top and bottom ends), and the lubricant discharge line shows the returning oil has a bright blue color, just as in Fig. 32, indicative that a gas does not circulate in the system.

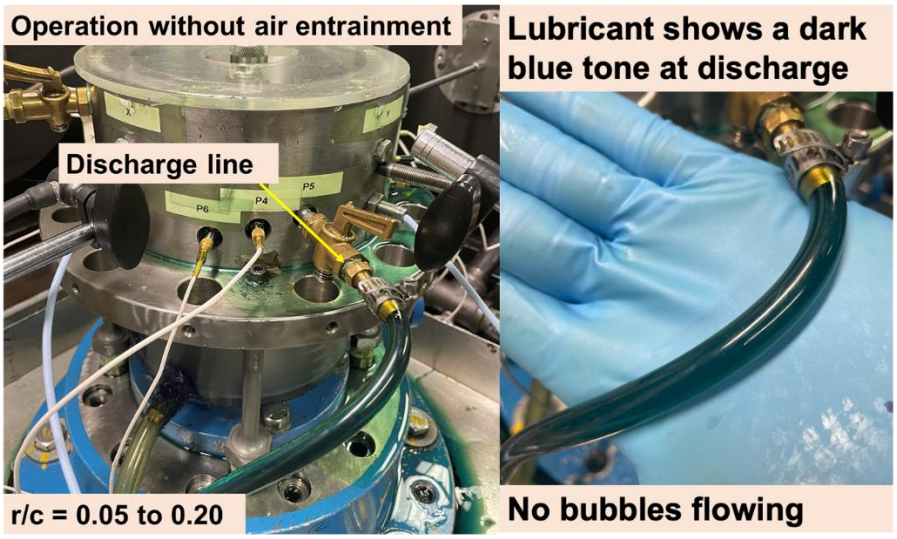

Figure 31. ORs sealed ends damper. Photographs depicting SFD operating at r =0.20c and P_S = 0.69 bar(g). Whirl frequency ω = 70 Hz, v_s=24.5 mm/s.

Figure 32 summarizes the video graphic evidence and shows pictures of the damper top journal end and lubricant discharge line while operating at v_s = 31, 43 and 55 mm/s. At v_s = 31 mm/s, when the damper operates at ω = 70 Hz and r/c = 0.25, small bubbles and a minute amount of oil leave through the top side of the journal. In addition, the discharge line shows oil colored light blue mixed with small air bubbles of air when returning to the reservoir; hence denoting the presence of air leaving the film land, see Fig. 32 (a). Additionally, the records in the embedded video (https://youtu.be/R5WPD6t1fWs?t=29) depict the SFD test rig at v_s = 31 mm/s and capture the incidence of air ingestion. This behavior only exacerbates as the squeeze velocity increases, for example at r = 0.35c and ω = 70 Hz (v_s= 43 mm/s).

With the system operating at v_s = 43 mm/s, shown in Fig. 32 (b), the bubbles leaving the top side of the journal are more numerous, and the bubbly oil exiting the damper appears lighter in color, see https://youtu.be/R5WPD6t1fWs?t=71. When the damper operates at v_s=55 mm/s, oil droplets and bubbles leave the top surface of the journal, and the return line presents a turquoise

lubricant gaseous mixture, see Fig. 33 (c) and https://youtu.be/R5WPD6t1fWs?t=124. Hence, at this condition the gas content in the squeeze film land is higher.

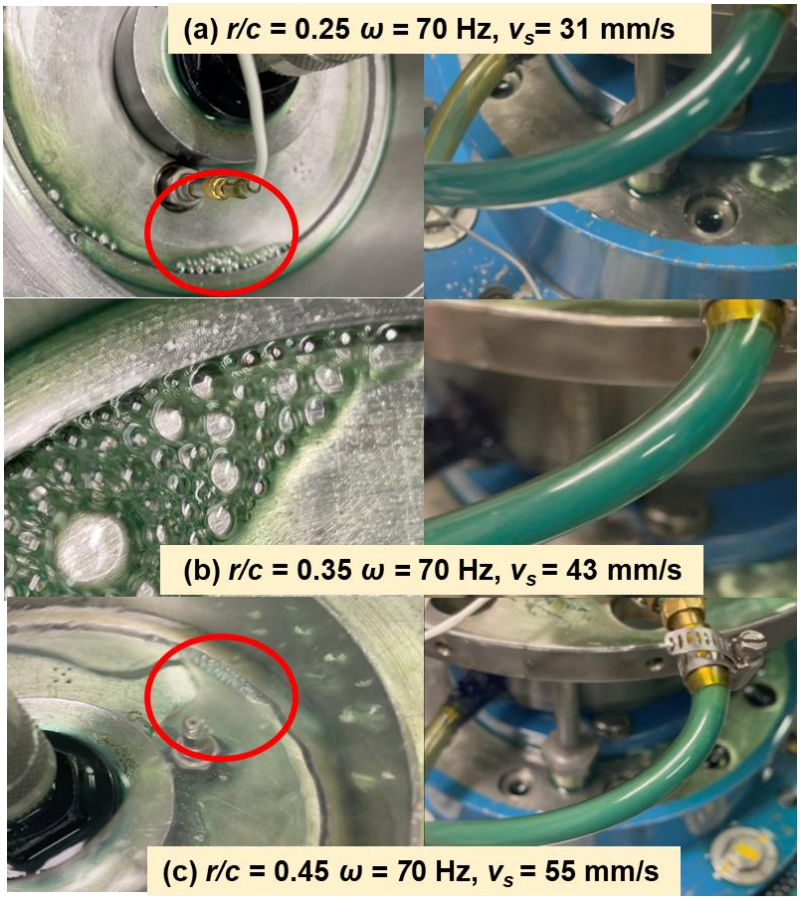

Figure 32. ORs sealed ends damper. Photographs depicting SFD operating at (a) *r/c*=0.25, (b) *r/c*=0.35 and (c) *r/c* = 0.45 and with P_S = 0.69 bar(g). Whirl frequency *ω* = 70 Hz.

The video graphical evidence in the embedded hyperlinks shows the test rig operating at increasing squeeze velocities (v_s) supports the likelihood of air ingestion for operation with $v_s \geq 31$ mm/s. This effect worsens as the squeeze velocity reaches 55 mm/s. Even though the video records do not quantify the volume of air drawn into the damper, they capture the operating conditions in which the O-rings cannot fully seal the damper clearance, i.e., the onset of air entrainment in an OR-SFD.

Another set of accompanying experiments follows to quantify the gas volume fraction (GVF) in the damper film land operating with air entrainment. Figure 33 depicts schematic views summarizing the process of estimating the GVF from a lubricant sample. The experiments consist in extracting a small volume of lubricant from the damper film land into an initially deflated balloon for approximately 10 s. Then, a scale determines the weight of the balloon holding the lubricant sample ($m_{balloon}=w_{\text{balloon}}/g$), which may contain air dissolved in it, and the volume of the sample assuming it solely contains lubricant is $V_{oil}=w_{balloon}/(\rho g)$. Next, the enclosed sample is fully submerged inside a cylindrical container partially filled with lubricant, the lubricant in the container rises a certain height (Δh), and the estimated volume of the sample is $V_{balloon}=(\Delta h \pi d^2/4)$. Where d is the inner diameter of the cylindrical container. Afterwards, the ratio between the volume of the sample assuming its mass is full of lubricant (V_{oil}) and the volume estimated by submerging the balloon in lubricant ($V_{balloon}$) is equivalent to the sample liquid volume fraction (LVF). Hence, the complement of the liquid volume fraction (1-LVF) is equivalent to the gas volume fraction (GVF=1-LVF), assumed to be the gas content in the damper film land.

Additionally, the system operates at a supply pressure P_S=0.73 bar(g), so the pressure drop caused by opening the additional valve sets the lubricant supply pressure at 0.69 bar(g). It is important to mention the measurements rely on the assumption that the open discharge line used to fill the balloon does not alter the damper dynamic pressure field.

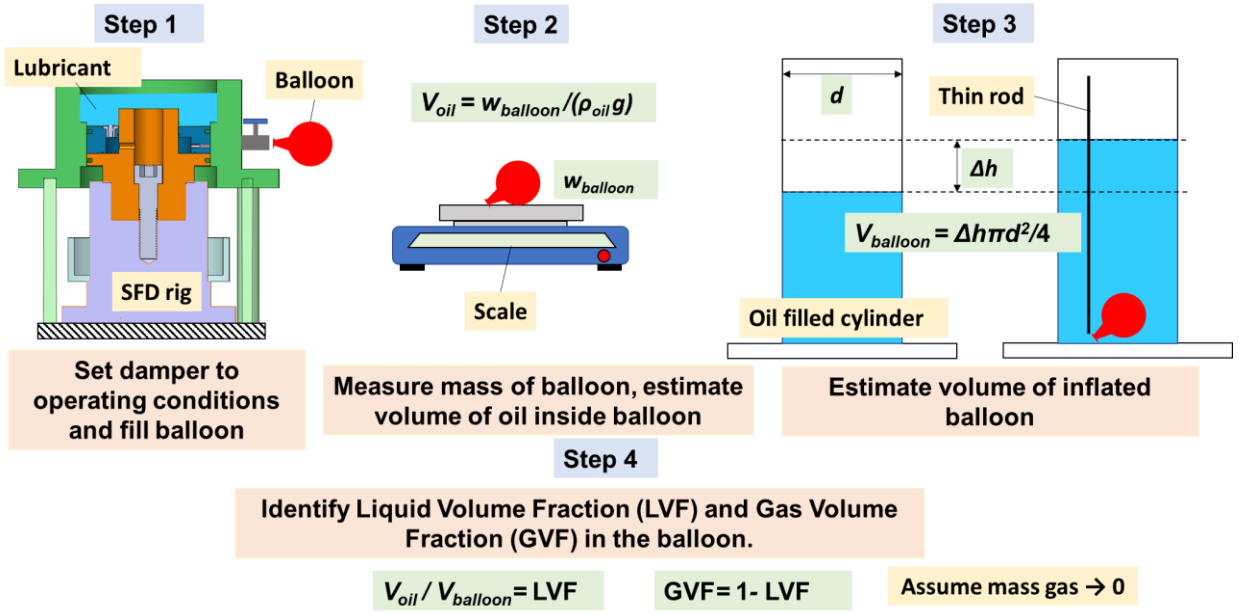

Figure 33. Schematic views depicting steps to estimate the GVF in the damper

The measurements estimating the damper GVF span orbit amplitudes from r/c = 0.15, to 0.45 and whirl frequencies ω= 55 and 70 Hz; operating conditions in which gas entrainment is more likely to happen. The video embedded in https://youtu.be/AtVBw5XMdcw summarizes the measurements, showcasing the experimental apparatus operating at r = 0.25c, 0.30c, 0.35c, 0.40c and 0.45c at ω = 70 Hz. First, operation under a static condition shows GVF~0, as seen in https://youtu.be/AtVBw5XMdcw?t=54. However, more gas content is present in the damper with increasing squeeze velocities, for example see https://youtu.be/AtVBw5XMdcw?t=104, showing the OR-SFD operating at v_s=24 mm/s.

Incidentally, the pigmentation of the lubricant appears lighter in tone as the squeeze velocity increases, see https://youtu.be/AtVBw5XMdcw?t=114, at v_s=31 mm/s, compared to https://youtu.be/AtVBw5XMdcw?t=196 at v_s=55 mm/s. Moreover, the contents filling the balloons show an increased amount of gas as the squeeze velocity rises; and in some instances, air coming out of solution inside the lubricant sample is visible, see https://youtu.be/AtVBw5XMdcw?t=151. Hence air entrainment becomes prominent at high

squeeze velocities (v_s>40 mm/s). During the experiments, the valve remains open for nearly the same amount of time, ~10s for all conditions. However, the balloons inflate to a notably larger volume at r = 0.35c, 0.40c and 0.45c, compared to r = 0.30c and 0.25c, indicating a larger GVF at larger squeeze velocities. Table 8 lists the hyperlinks to the videos showing air entrainment in the damper for quantifying the GVF in the film land.

Table 8. Summary of hyperlinks to OR-SFD videos

Hyperlink	Description	Squeeze Velocity [mm/s]	Orbit radius (r/c) [-]	Whirl Frequency (ω) [Hz]
https://youtu.be/R5WPD6t1fWs	OR-SFD showcasing air entrainment	[-]	[-]	[-]
https://youtu.be/R5WPD6t1fWs?t=29		31	0.25	70
https://youtu.be/R5WPD6t1fWs?t=71		43	0.35	70
https://youtu.be/R5WPD6t1fWs?t=124		55	0.45	70
https://youtu.be/AtVBw5XMdcw	Estimation of GVF	[-]	[-]	[-]
https://youtu.be/AtVBw5XMdcw?t=54		0	0	0
https://youtu.be/AtVBw5XMdcw?t=104		24	0.20	70
https://youtu.be/AtVBw5XMdcw?t=114		31	0.25	70
https://youtu.be/AtVBw5XMdcw?t=151		37	0.30	70
https://youtu.be/AtVBw5XMdcw?t=196		55	0.45	70

Figure 34 summarizes the estimated GVF, obtained as the average of three sets of measurements, shown vs. orbit radius vs. (a) whirl frequency and (b) squeeze velocity. Depicted in Fig. 35, the estimated gas content in the damper is GVF~7%, at v_s < 30 mm/s, which corresponds to orbit amplitudes $r \leq 0.20c$ and up to ω= 70 Hz. Even so, the GVF increases to ~25% at 34 mm/s $\leq v_s \leq$ 43 mm/s, and then it jumps to GVF~45% at v_s~ 44 mm/s. At the largest experimental squeeze

velocity (v_s= 55.2 mm/s), corresponding to r/c = 0.45 and ω = 70 Hz, the gas content surpasses oil, with GVF~58%.

The experiments estimating the GVF in the damper illustrate the increasing gas content in the OR-SFD as v_s > 30 mm/s. Nonetheless, the results presented in Fig. 34 show a sizeable variability, particularly when identifying a low GVF. Each measurement is conducted three times, to determine a coefficient of variability (CV):

$$\mathrm{CV} = \frac{\sigma}{\bar{x}} \tag{14}$$

Where σ is standard deviation in each measurement and $\bar{x}$ the mean value of the three estimations. The GVF show a coefficient of variability (CV) less than 10% at $r/c \geq 0.40$ and $\omega \geq$ 55 Hz ($v_s \geq$ 39 mm/s), indicated by the results above the horizontal green plane in Fig. 34. On the other hand, the results below the blue inset plane in Fig. 34 are less reliable, corresponding to measurements at $r \leq 0.35c$ and $\omega \leq 50$ Hz show a coefficient of variability larger than 20%.

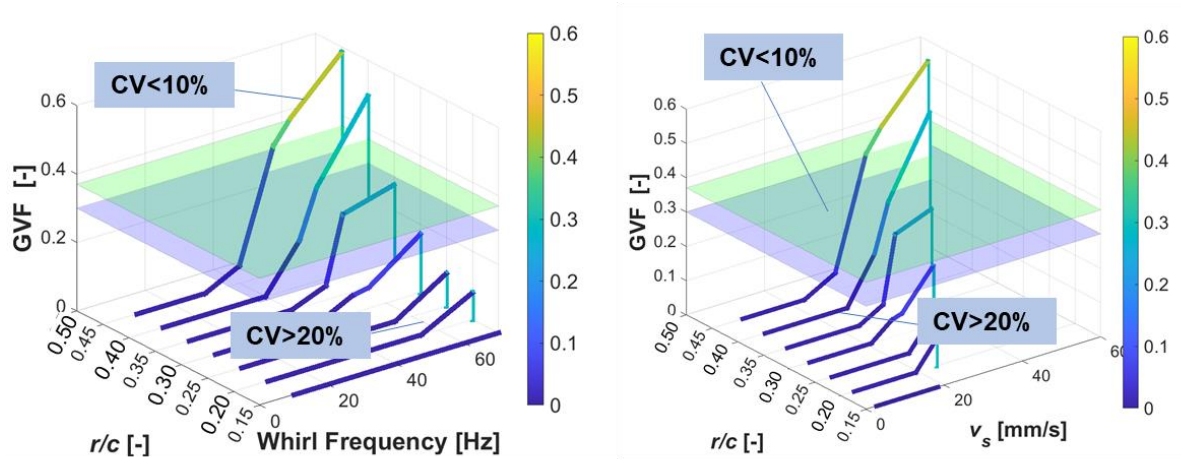

(a) Estimated GVF vs. whirl frequency and vs. Orbit radius (r/c)

(b) Estimated GVF vs squeeze velocity (v_s) and vs orbit radius (r/c)

Figure 34. (a) Estimated GVF vs. orbit radius (r/c) and whirl frequency (ω) for OR sealed SFD. (b) Estimated GVF vs. (r/c) and squeeze velocity (v_s).

The measured dynamic stiffnesses shown in Fig. 17 show that the film viscous damping forces significantly decrease at v_s>43 mm/s, an operating condition that also shows air ingestion in the videos and an approximate GVF > 40%. Presently, the measurements show air ingestion occurs in an O-rings sealed SFD and which degrade its dynamic forced performance, seen as a reduction in $\mathrm{Im}(H_{SFD})_{XX,YY}$ and increase in $\mathrm{Re}(H_{SFD})_{XX,YY}$.

CHAPTER X
CONCLUSIONS AND RECOMMENDATIONS

This report presents measurements of the dynamic forced performance of an O-rings (ORs) sealed squeeze film damper (SFD) supplied with ISO VG 2 lubricant at P_S=0.69 barg (10 psig). The lubricant fills an upstream plenum and flows through a mechanical check valve into the squeeze film land through a single feedhole located halfway between the top and bottom O-rings. Experiments with single-frequency (ω) circular centered orbit (CCOs) motions (ω =10 Hz to 70 Hz) and increasing amplitude (r=0.05c to 0.45c), serve to identify the ORs and SFD force coefficients at squeeze velocities (v_s=$r\omega$) 1 mm/s< v_s<55 mm/s.

No prior art details the effects of orbit size on the dynamic performance of elastomeric seals undergoing the range of motions hereby reported. A parameter identification method delivers ORs' force coefficients representative over a frequency range from ω = 10 to 130 Hz (v_s=102 mm/s max.). The ORs stiffnesses (K_{OR}) remain nearly invariant over the whirl frequency range. At r = 0.05c K_{OR} rises to ~2 times the stiffness ($K_{OR,static}$) identified from static load tests. For increasing orbit amplitudes, K_{OR} decays, and as $r \rightarrow$0.45c, K_{OR} only adds up to 40% the magnitude of $K_{OR,static}$. A quadrature stiffness ($K_{\perp}$) in the ORs, indicative of structural-like damping, produces a significant loss factor $\eta = K_{\perp}/K_{OR}$ = 0.60 for r = 0.45c. The ORs equivalent viscous damping coefficients (C_{OR}) represent ~10% of the damping in the lubricated system for r=0.05c and 0.10c. However, the contribution of the ORs to the lubricated system damping decreases to just 3% for orbits larger than r= 0.25c.

The measurements with a lubricated system from ω = 10 to 70 Hz produce complex dynamic stiffnesses (H_L) to identify SFD force coefficients over a smaller frequency range. The test derived added mass coefficients (M_{SFD}) remain constant for $r \leq 0.25c$, nearly equivalent to the theoretical

added mass coefficient, M^*; alas, M_{SFD} plunges as $r \rightarrow 0.45c$ to ~$0.3M^*$. The film damping coefficients (C_{SFD}) depict nearly constant magnitudes, $C_{SFD} \sim 0.9C^*$, as $r \rightarrow 0.25c$. Nonetheless, C_{SFD} reduces with increasing orbit amplitudes, reaching $C_{SFD} \sim 0.6C^*$ as $r \rightarrow 0.45c$.

A CCO model described in Ref. [47] delivers SFD added mass and damping coefficients by simulating the journal kinematics. Overall, the predictions agree well with the experiments. As $r \rightarrow 0.40c$, the model overpredicts the added mass terms by 5%, and for $r = 0.45c$, the difference amounts to ~15%. For damping coefficients, the predicted damping magnitudes are 8% larger than the experiments for $r \leq 0.25c$, and for larger whirl orbit amplitudes, the difference also increases to ~15%.

The film pressure measurements reveal distorted pressure profiles, unique in shape, along with pressure spikes denoting gas bubbles collapsing. Thus, attesting for air ingestion for $r > 0.30c$ and $\omega > 50$ Hz ($v_s > 26$ mm/s). Moreover, a flat pressure zone, indicative of lubricant vaporous cavitation, is evident at $v_S > 39$ mm/s, both becoming significant contributors to the degradation of the OR-SFD dynamic performance.

The film peak-peak pressures increase with ω and r for $r \leq 0.35c$, however, for larger orbit amplitudes and beyond ω=50 Hz (v_s>31 mm/s), the peak-peak pressures decline. Thus, showing both air ingestion and oil vapor cavitation prevent the generation of film pressures proportional to v_s. Peak pressure measurements are significant in magnitude inside the oil delivery plenum and reach ~45% of the supply pressure (P_S) depicting the same trend as in the film land pressures. Consequently, the plenum pk-pk pressures exhibit the incidence of lubricant backflow despite having a check valve in place.

Video records of the operating test rig show the incidence of air entrainment for $r \geq 0.25c$ ($v_s \geq 31$ mm/s). Additionally, a set of accompanying experiments estimates the gas volume fraction

(GVF) in the damper film land operating with air entrainment. The measurements show a GVF~ 25% for 34 mm/s $\leq v_s \leq$ 43 mm/s, and GVF~45% for v_s~ 44 mm/s. At the largest experimental squeeze velocity (v_s= 55 mm/s), corresponding to r = 0.45c and ω = 70 Hz, the gas content surpasses oil, with GVF~58%.

The analysis thus quantifies the contribution of the elastomeric seals to the dynamic forced response of a OR-SFD throughout the entire range of test conditions. Additionally, it is the first time the GVF in a SFD is estimated using a simple empirical method. The current research demonstrates the amplitude dependence of the ORs dynamic forced response. Most notably, this research distinguishes the onset of air entrainment and the decay it causes on the forced performance of a sealed damper.

Recommendations for Future Work

The current experimental facility should undergo modifications to further investigate a broad range of squeeze velocities and inlet/outlet lubricant feed pressures in sealed damper configurations. A parametric study identifying the dynamic response of different OR seal geometries and OR grooves could complement this research effort.

To continue producing experiments with the OR-SFD, a new pair of electromagnetic shakers with a larger load capacity should be acquired. The shakers could produce broader orbit amplitudes and whirl frequencies. A new BC design should include a transparent window to visualize the squeeze film to visualize gaseous phenomena, such as air ingestion or lubricant (vapor and gaseous) cavitation.

REFERENCES

[1] San Andrés, L., 2010, *Modern Lubrication Theory,* "Squeeze Film Dampers," Notes 13, Texas A&M University Digital Libraries, [Jun 16, 2021], http://oaktrust.library.tamu.edu/handle/1969.1/93253.

[2] Miyachi, T., Hoshiya, S., Sofue, Y., Matsuki, M., and Torisaki, T., 1979 , "Oil Squeeze Film Dampers for Reducing Vibration of Aircraft Gas Turbine Engines," ASME Paper No. 79-GT-133, https://doi.org/10.1115/79-GT-133.

[3] Parker O-ring Handbook ORD 5700, Parker Hannifin Corporation, Lexington, KY, USA, [Sep 30th, 2020] https://www.parker.com/Literature/O-Ring%20Division%20Literature/ORD%205700.pdf.

[4] Gehannin, J., and Arghir, M., 2010, "Complete Squeeze-Film Damper Analysis Based on the "Bulk Flow" Equations," Tribol. Trans., **53**(1), pp. 84–96, https://doi.org/10.1080/10402000903226382 .

[5] Edney, S. L., Nicholas, J. C., 1999, "Retrofitting a Large Steam Turbine With a Mechanically Centered Squeeze Film Damper," Proc. 27th Turbomachinery Symposium, Houston, TX, pp. 29–40, https://doi.org/10.21423/R1X660.

[6] Bansal, P. N., and Hibner, D. H., 1978, "Experimental and Analytical Investigation of Squeeze Film Bearing Damper Forces Induced by Offset Circular Whirl Orbits," ASME J. Mech. Design, **100**(3), pp. 549-557, https://doi.org/10.1115/1.3453967.

[7] San Andrés, L., 2010, *Mechanical Vibrations,* "Experimental Identification of Bearing Force Coefficients," Notes 15, Texas A&M University Digital Libraries, [Jun 16, 2021], https://hdl.handle.net/1969.1/93280.

[8] Marmol, R.A, Vance, J.M., 1978 "Squeeze Film Damper Characteristics for Gas Turbine Engines," ASME J. Mech. Design, **100**(1), pp. 139-146, https://doi.org/10.1115/1.3453878.

[9] Leader, M. E., Whalen, J. K., Grey, G. G., and Hess, T.D., 1995, "The Design and Application of a Squeeze Film Damper Bearing to a Flexible Steam Turbine Rotor," Proc. 24th Turbomachinery Symposium, Houston, TX, pp. 49–58, https://doi.org/10.21423/R1R36D.

[10] Li, W., Braman, C., Hantz, B., Thorat, M., and Pettinato, B., 2020, "Squeeze Film Damper Bearing with Double-Ended Beam Springs: Part I – Design and Analysis," ASME Paper No. GT2020-16329, https://doi.org/10.1115/GT2020-16329.

[11] Li, W., Braman, C., Hantz, B., Thorat, M., and Pettinato, B., 2020, "Squeeze Film Damper Bearing with Double-Ended Beam Springs: Part II – Experimental Validation," ASME Paper No. GT2020-15491, https://doi.org/10.1115/GT2020-15491.

[12] Belforte, G., Colombo, F., Raparelli, T., and Viktorov, V., 2008, "High-Speed Rotor with Air Bearings Mounted on Flexible Supports: Test Bench and Experimental Results," ASME J. Tribol., **130**(2), p. 021103, https://doi.org/10.1115/1.2908905.

[13] Waumans, T., Peirs, J., Al-Bender, F., and Reynaerts, D., 2011, "Aerodynamic Journal Bearing with a Flexible, Damped Support Operating at 7.2 Million DN," J. Micromech. Microeng., **21**, p. 104014, https://iopscience.iop.org/article/10.1088/0960-1317/21/10/104014.

[14] Cunningham, C., Ransom, D., Wilkes, J., Bishop, J., and White, B., 2018, "Mechanical Design Features of a Small Gas Turbine for Power Generation in Unmanned Aerial Vehicles," ASME Paper No. GT2015-43491, https://doi.org/10.1115/GT2015-43491.

[15] Nashif, A.D., Jones, D.I.G., and Henderson, J.P., 1985, *Vibration Damping*, John Wiley & Sons, Inc., pp. 67-84.

[16] Sun, C.T., and Lu, Y.P., 1995, *Vibration Damping of Structural Elements*, Prentice Hall PTR, Englewood Cliffs, NJ, pp. 26-44.

[17] Ginsberg, J.H., 2001, *Mechanical and Structural Vibration,* John Wiley & Sons, Inc., pp. 133-140.

[18] Smalley, A., Darlow, M., and Mehta, R., 1978, "The Dynamic Characteristics of O-Rings," ASME J. Mech. Design, **100**(1), pp. 132–138, https://doi.org/10.1115/1.3453877.

[19] Green, I., and Etsion, I., 1986, "Pressure and Squeeze Effects on the Dynamic Characteristics of Elastomer O-Rings Under Small Reciprocating Motion," ASME J. Tribol., **108**(3), pp. 439-444, https://doi.org/10.1115/1.3261231.

[20] N. Aktrük, and R. Gohar, 1994, "Damping the Vibrations of a Rigid Shaft Supported by Ball Bearings by Means of External Elastomeric O-Rings Dampers," Proc. Instn. Mech. Engrs **208**(3), pp. 183-190.

[21] The World's Best O-ring Handbook, NewDeal Seals, Warmenhuizen, Nederland, [Jun 30th, 2021] https://newdealseals.com/app/uploads/2020/04/NewDealSeals-O-Ring-Handbook-2014.pdf

[22] Dichtomatik O-ring Handbook, Dichtomatik O-Rings, Plymout, MI, USA, [Jun 30th, 2021] http://www.allsealsinc.com/dichtomatik/dichtomatik_oring_handbook.pdf.

[23] Belforte, G., Raparelli, T., Viktorov, V., and Colombo, F., 2008, "High-Speed Rotor with Air Bearings Mounted on Flexible Supports: Test Bench and Experimental Results," J. Tribol, **130**(2), p. 021103, https://doi.org/10.1115/1.2908905.

[24] Tomioka, J., Miyanaga, N., 2008, "Measurements of Dynamic Properties of O-rings and Stability Threshold of Flexibly Supported Herringbone Grooved Aerodynamic Journal Bearings," Tribology Online, **3**(7), pp. 366-369, https://doi.org/10.2474/trol.3.366.

[25] Al-Bender, F., Colombo, F., Reynaerts, D., Villavicencio, R., and Waumans, T., 2017, "Dynamic Characterization of Rubber O-rings: Squeeze and Size Effects," Advances in Tribology, **2017**, p. 2509879, https://doi.org/10.1155/2017/2509879.

[26] Shoyama, T., and, Fujimoto, K., 2018, "Calculation of High-Frequency Dynamic Properties of Squeezed O-ring for Bearing Support," Mechanical Engineering Journal., p. 17-004444, https://doi.org/10.1299/mej.17-00444.

[27] Battig, P., and Schiffman, J., 2019, "Data-Driven Model for the Dynamic Characteristics of O-Rings for Gas Bearing Supported Rotors," J. Appl. Mech., **86**(8), p. 081003, https://doi.org/10.1115/1.4043473.

[28] Parsons, C.A., and Stoney, G.G., 1906, "The Steam Turbine," Proc. Ins, Civil Eng. **163**, pp. 167-198, https://doi.org/10.1680/imotp.1906.16610.

[29] Birmann, R., 1930, US Patent 1,926,225 "Turbo Compressor".

[30] Birmann, R., 1946, US Patent 2,403,489, "Bearing Construction for Turbines or the like".

[31] Cooper, S., 1963, "Preliminary Investigation of Oil Films for Control of Vibration," Proc. Lubrication and Wear Convention, Inst. Mech. Eng., pp. 305–315.

[32] Della Pietra, L., and Adiletta, G., 2002, "The Squeeze Film Damper over Four Decades of Investigations. Part I: Characteristics and Operating Features," The Shock and Vibration Digest, **34**(1), pp. 3-26.

[33] Della Pietra, L., and Adiletta, G., 2002, "The Squeeze Film Damper over Four Decades of Investigations Part II: Rotordynamic Analyses with Rigid and Flexible Rotors," The Shock and Vibration Digest, **34**(2), pp. 97-126.3.

[34] San Andrés, L., Jeung, S.-H., Den, S., and Savela, G., 2016, "Squeeze Film Dampers: An Experimental Appraisal of Their Dynamic Performance," Proc. 2016 Asia Turbomachinery & Pump Symposium, Marina Bay Sands, Singapore, Feb. 22–25, pp. 1–23, https://doi.org/10.21423/R12Q4N.

[35] Vance, J., and Kirton, A., 1974, "Preliminary Investigation of the Dynamic Force Response Coefficients for Squeeze Film Bearing Dampers," Research Report to the US Army Research Office – Durham, AD/A-004 020, University of Florida, Gainesville, https://apps.dtic.mil/sti/pdfs/ADA004020.pdf.

[36] Feder, E., Bansal, P. N., and Blanco, A., 1978, "Investigation of Squeeze Film Damper Forces produced by Circular Centered Orbits," ASME J. Eng. Gas Turb. Power, **100**(1), pp. 15-21, https://doi.org/10.1115/1.3446313.

[37] Kuzdzal, M. J., and Hustak, J. F., 1996, "Squeeze Film Damper Bearing Experimental Vs Analytical Results for Various Damper Configurations," Proceedings of the 25th Turbomachinery Symposium, Houston, TX, Sept. 17-19, pp. 57-70, https://doi.org/10.21423/R1V36B.

[38] Zeidan, F., San Andrés L., and Vance, J., 1996, "Design and Application of Squeeze Film Dampers in Rotating Machinery," 25th Turbomachinery Symposium, Houston, TX, Sept. 17-19, pp. 169-188, https://doi.org/10.21423/R1694R.

[39] Jei. Y.G., Kim, J.S., Hong S.W., and Jung S.Y., 1999, "A New Lateral Vibration Damper Using Leaf Springs," ASME J. Vib. Acoust., **121**(3), pp. 343-350, https://doi.org/10.1115/1.2893986.

[40] Kanki, H., Adachi, K., Takahashi, T., Nozaki, N., Asano, Y., 2006, "An Experimental Investigation of Brake Squeal Suppression of Air Brake Systems for Electric Passenger Trains Using Oil Damper", ASME Paper No. IMECE2006-13653, https://doi.org/10.1115/IMECE2006-13653.

[41] Kim, K.J., Lee, C.W., and Koo, J.H., 2008, "Design and Modeling of Semi-Active Squeeze Film Dampers Using Magneto-Rheological Fluids," J. Smart Mater. Struct., **17**(3), p. 035006, http://dx.doi.org/10.1088/0964-1726/17/3/035006.

[42] Memmott, E.A., 2010, "Application of Squeeze Film Dampers to a Large Centrifugal Compressor," ASME Paper No. GT2010-23553, https://doi.org/10.1115/GT2010-23553.

[43] Shoyama, T., and Fujimoto, K., 2018, "Dynamic Properties of Water-Lubricated Double Clearance Squeeze Film Damper Supported by O-Rings," ASME paper No. GT2018-76404, https://doi.org/10.1115/GT2018-76404.

[44] San Andrés, L., and Koo, B., 2018, "Effect of Lubricant Supply Pressure on SFD Performance: Ends Sealed With O-Rings and Piston Rings," Proc. of the IFToMM Conference on Rotor Dynamics, Río de Janeiro, Brazil, Sept. 23-27, Paper No. IFTOMM2018-0181, https://doi.org/10.1007/978-3-319-99262-4_26.

[45] San Andrés, L., Koo, B., and Jeung, S.-H., 2019 "Experimental Force Coefficients for Two Sealed Ends Squeeze Film Dampers (Piston Rings and O-Rings), An Assessment of Their Similarities and Differences," ASME J. Eng. Gas Turb. Power, **141**(2)**,** p. 021024, https://doi.org/10.1115/1.4040902.

[46] San Andrés, L., and Rodríguez, B., 2021, "On the Experimental Dynamic Force Performance of a Squeeze Film Damper Supplied Through a Check Valve and Sealed with O-Rings", ASME J. Eng. Gas Turb. Power, **143**(11), p. 111011 https://doi.org/10.1115/1.4051964.

[47] San Andrés, L., and Jeung, S.-H., 2016, "Orbit-Model Force Coefficients for Fluid Film Bearings: A Step Beyond Linearization," ASME J. Eng. Gas Turbines Power, **138**(2), p.022502, https://doi.org/10.1115/1.4031237.

[48] San Andrés, L., 2008, *Mechanical Vibrations,* "Dynamic Response of Continuum Systems," Notes 14, Texas A&M University Digital Libraries, [Aug 26, 2021], https://hdl.handle.net/1969.1/93279.

[49] Payne, A.R., 1962, "The Dynamic Properties of Carbon Black-Loaded Natural Rubber Vulcanizates. Part I," J. App Pol Sci **6**(19), pp. 57-63.

[50] García, M.J., Kari, L., Vinolas, J., and Negrete, N.G., 2007, "Frequency and Amplitude Dependence of the Axial and Radial Stiffness of Carbon-Black Filled Rubber Bushings," Polymer Testing, **26**(5), pp. 629-638, https://doi.org/10.1016/j.polymertesting.2007.03.011.

[51] Rendek, M., and Lion, A., "Amplitude Dependence of Filler-Reinforced Rubber: Experiments, Constitutive Modeling and FEM – Implementation," Int. J. Solid Struc., **47**(21), pp. 2918-2936, https://doi.org/10.1016/j.ijsolstr.2010.06.021.

[52] Kareaga, Z., 2016. "Dynamic Stiffness and Damping Prediction on Rubber Materials, FEA and Experimental Correlation," Ph.D. Dissertation, London Metropolitan University, UK, https://core.ac.uk/download/pdf/76979813.pdf.

[53] San Andrés, L., 1985, "Effect of Fluid Inertia Effect on Squeeze Film Damper Force Response," Ph.D. Dissertation, Texas A&M University, College Station, TX, https://hdl.handle.net/1969.1/DISSERTATIONS-428234.

[54] Díaz, S., and San Andrés, L., 2001 "Air Entrainment Versus Lubricant Vaporization in Squeeze Film Dampers: An Experimental Assessment of Their Fundamental Differences,", ASME J. Eng. Gas Turbines Power, **123**(4), pp. 871-877, https://doi.org/10.1115/1.1383258 .

[55] Díaz, S., and San Andrés, L., 1999, "Reduction of the Dynamic Load Capacity in a Squeeze Film Damper Operating with a Bubbly Lubricant," ASME J. Eng. Gas Turbines Power, **121**(4), pp. 703-709 https://doi.org/10.1115/1.2818530.

[56] Díaz, S., and San Andrés, L., 2002, "Pressure Measurements and Flow Visualization in a Squeeze Film Damper Operating with a Bubbly Mixture," ASME J. Trib. **124**(4), pp. 346-350. https://doi.org/10.1115/1.1402133.

[57] San Andrés and Díaz, S., L., 2003, "Flow Visualization and Forces from a Squeeze Film Damper Operating with Natural Air Entrainment," ASME J. Tribol., **125**(2), pp. 325-333 https://doi.org/10.1115/1.1510878.

[58] "Mobil Velocite™ No 3 (ISO VG 2) Manufacturer specification sheet,", Hydraulic oils Typical Properties, Mobil, Accessed February 2021. https://www.mobil.ca/en-CA/lubricants/industrial/lubricants/products/products/mobil-velocite-oil-no-3

[59] Ng, W.S., Levesley, M. C., and Priest, M., 2005, "Effects of Bubble on the Viscosity Properties of Lubricants," ASME Paper No. WTC2005-64114, https://doi.org/10.1115/WTC2005-64114.

[60] Roelands, C.J.A, Vlugter, J.C., and Waterman, H.I., 1963, "The Viscosity-Temperature-Pressure Relationship of Lubricating Oils and its Correlation With Chemical Constitution" J. Basic Eng., **85**(4), pp. 601-607, https://doi.org/10.1115/1.3656919.

[61] San Andrés, L., 2019, *Measurements of Sounds and Vibration*, "Sensor calibration & uncertainty in measurements and engineering analysis," Texas A&M University, https://rotorlab.tamu.edu/me459/NOTES%205%20Sensors%20and%20Uncertainty%20Analysis.pdf [March 23rd, 2021].

[62] "NI 9215 Datasheet," Datasheet for NI 9215 analog input module, National Instruments, 2016, https://www.ni.com/pdf/manuals/373779a_02.pdf.

[63] “NI cDAQ -917x User Manual,” User manual for NI compact DAQ 9171/9174/9178 USB Chassis, National Instruments, July, 2011, https://www.ni.com/pdf/manuals/372780k.pdf.

[64] “353B33 PCB™ Product Datasheet” Product specification sheet for 353B33 piezoelectric accelerometer, PCB Piezotronics ™, July, 2007, https://www.pcb.com/products?model=353b33.

[65] Fornasini, P., 2008, *The Uncertainty in Physical Measurements,* Springer, New York, pp. 184-189.

[66] Coleman, H. W., and Steele, G. W., 1998, *Experimentation and Uncertainty Analysis for Engineers*, John Wiley & Sons, New York.

[67] Beckwith, T., Marangoni, R., and Lienhard., J., 1993, “Mechanical Measurements,” Prentice Hall. 5th edition, pp. 82.

[68] “PTFE Liquid Flow Sensor Manufacturer Specification Sheet,” FPR1501 Series Flow Sensor, Omega, Accessed April 27th, 2020, https://www.omega.co.uk/pptst/FPR1500.html

APPENDIX A

MEASUREMENTS OF LUBRICANT VISCOSITY

A viscometer (BROOKFIELD DVI^{TM}) identifies the oil viscosity versus temperature to compare against manufacturer specifications. The viscometer consists of a spindle, a cup to contain a sample of oil, and a water bath device to control the lubricant temperature. At a prescribed spindle speed and temperature, the viscometer uses a calibrated spring to measure the reaction torque opposed by the sample of lubricant and estimate its viscosity. Table A1 displays the lubricant properties provided by the manufacturer.

Table A1. Mobil Velocite ™ No. 3 (ISO VG 2) Manufacturer specifications [58]

Mobil Velocite Oil^{TM} No. 3 (ISO VG 2)	
cSt @ 40 ºC	2.1 (1.68 mPa-s)
cSt @ 100 [ºC]	0.95 (0.76 mPa-s)
Pour Point [ºC]	-36
Flash Point [ºC]	84
Density @ 15 ºC, kg/L	0.802

The water bath device heats the oil sample to a prescribed temperature and the viscometer estimates viscosity magnitudes at a spindle speed of 30rpm in increments of 5 ºC from 25 ºC to 95 ºC. Figure A1 displays three viscosity measurements in colored dots along with the viscosity curve specified by the manufacturer in dotted lines.

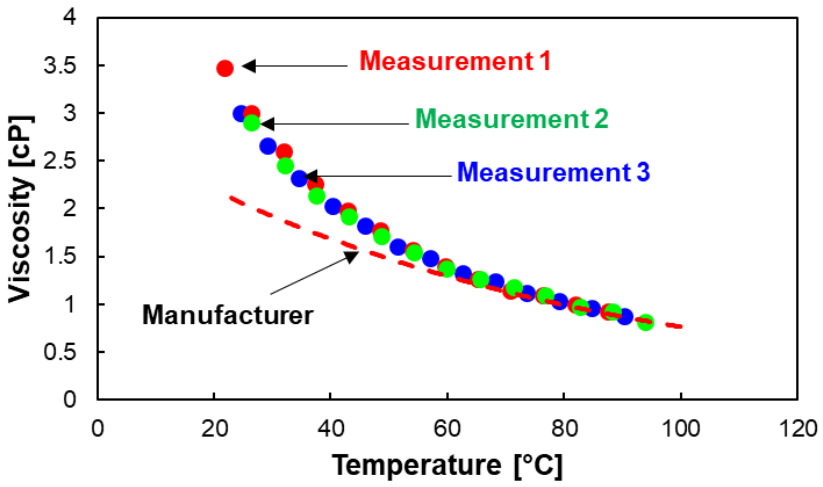

Figure A1. Oil viscosity vs. temperature.

Measurements of the lubricant mass in a known volume oil determines its density at room temperature of 20 ºC. The oil density is ρ = 0.800 kg/l, is almost identical to the manufacturer specification (see Table A1) This minuscule difference discards air entrainment in the lubricant, another cause of viscosity increment [59].

Roelands et al. [60] establish the relationship between oil viscosity and temperature:

$$\mu = \mu_R e^{-a_v (T - T_R)} \tag{A.1}$$

where μ is the predicted viscosity at temperature T in ºC. The measurements show the average viscosity at room temperature (T_R = 25 ºC) is μ_R= 2.81 mPa-s, and μ_2= 0.76 mPa-s at T_2 = 95ºC. Hence, the oil temperature to viscosity coefficient, a_v for the oil used in the experiments is:

$$a_v = \frac{-ln\frac{\mu_2}{\mu_R}}{T_2 - T_R} = 0.018 \frac{1}{^{o}\mathrm{C}} \tag{A.2}$$

The measurements indicate an average dynamic viscosity of 2.12 mPa-s at 40 ºC and 0.69 mPa-s at 100ºC. However, the manufacturer specifies a dynamic viscosity of 1.68 mPa-s at 40ºC and 0.76 mPa at 100ºC, showing an absolute average difference of ~15%. The differences are

likely due to the mix of multiple oil batches in the experimental facility oil reservoir over the span of multiple years of experiments, in addition to particulate gathering that could further alter the oil viscosity.

APPENDIX B

IDENTIFICATION OF JOURNAL RADIAL CLEARANCE

This section shows the process to estimate the radial clearance of the test damper. The SFD radial clearance is:

$$c = \tfrac{1}{2}\,(D_{BC,ID} - D_{J,OD}) \tag{B.1}$$

where $D_{BC,ID}$ is the bearing cartridge inner diameter and $D_{J,OD}$ is the journal outer diameter. A dial bore gauge determines with an uncertainty of 1.27 µm (0.05 mil) the BC inner diameter (ID). Figure B1 shows the schematic and cross section view of the BC and measurement planes to determine $D_{BC,ID}$. The annular gap between the interior surface of the bearing cartridge and the journal outer surface of the journal hosts a lubricant film with uniform axial thickness. One set of nine measurements along three different axial planes and three radial planes in the BC surface determine the average BC inner diameter ($D_{BC,ID}$).

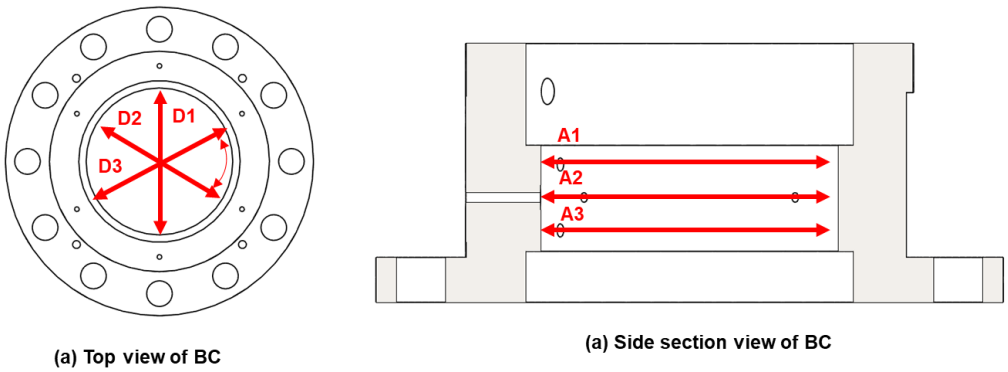

Figure B1. Bearing cartridge (a) top view, and (b) cross sectional view.

Similarly, measurements of the journal outer diameter (OD) along the top, middle, and bottom plane and three circumferential angles determine the average journal outer diameter ($D_{J,OD}$). Figure B2 displays the journal measurement locations. An OD micrometer, with an uncertainty of ±1.78 µm (± 0.07 mil), determines $D_{J,OD}$. Table B1 lists measurements of $D_{BC,ID}$ and $D_{J,OD}$.

Table B2 lists the average $D_{BC,OD}$ and $D_{J,OD}$ for each measurement plane measurement, and the average clearance c. From measurements in nine different locations, the total average radial clearance c, is 0.279 mm.

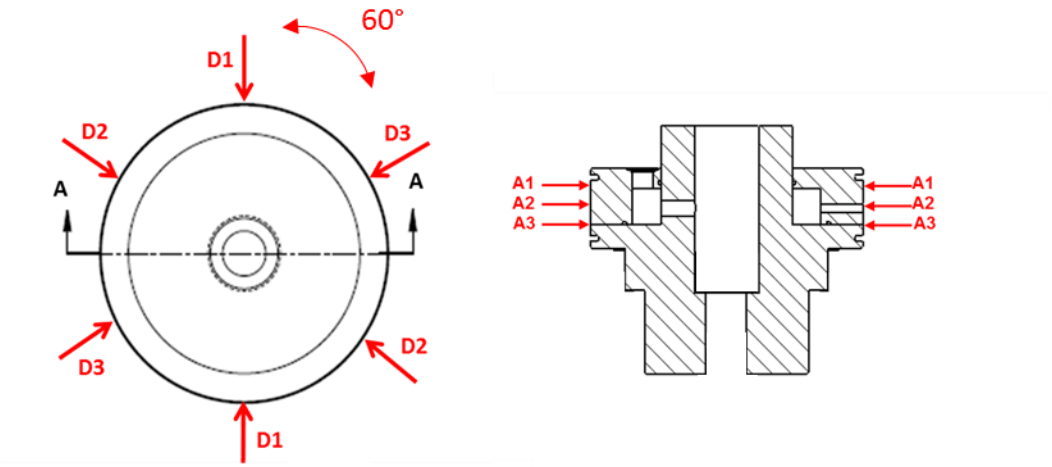

(a) Top view of journal (b) Cross sectional view of journal

Figure B2. Journal (a) top view, and (b) cross sectional view.

Table B1. Measurements of BC and journal outer diameter

Measurement angle	Measurement plane	Journal OD [mm (in)]	BC ID [mm (in)]
D1	A1	127.19 (5.0074)	126.62 (4.9850)
	A2	127.20 (5.0077)	126.64 (4.9860)
	A3	127.17 (5.0065)	126.62 (4.9850)
D2	A1	127.17 (5.0067)	126.62 (4.9850)
	A2	127.20(5.0080)	126.64 (4.9860)
	A3	127.18 (5.0070)	126.62 (4.9850)
D3	A1	127.19 (5.0075)	126.62 (4.9850)
	A2	127.20 (5.0078)	126.64 (4.9860)
	A3	127.19 (5.0075)	126.62 (4.9850)

Table B2. Average clearance measurement along three axial planes

Plane	Average $D_{BC,OD}$ [mm (in)]	Average $D_{J,OD}$ [mm (in)]	c [mm (in)]
A1	127.18 (5.0072)	126.62 (4.9850)	0.282 (0.0111)
A2	127.20 (5.0078)	126.64 (4.9860)	0.277 (0.0109)
A3	127.18 (5.0070)	126.62 (4.9850)	0.279 (0.0110)
Total Average	127.19 ± 0.0050 (5.007 ± 0.0002)	126.64± 0.0040 (4.985± 0.0002)	**0.279 ± 0.0060** (0.0110 ± 0.0002)

APPENDIX C

UNCERTAINTY OF IDENTIFIED PARAMETERS

This section presents the calculation of the uncertainty in the identified SFD, O-rings and structure force coefficients. The total uncertainty of the estimated force coefficients comprises a precision uncertainty (U_P) and measurement variability (U_V).,

Precision uncertainty (U_P)

Precision uncertainty is related to the estimation of the force coefficients in the physical model curve fit. Circular centered orbit motions over a range of selected frequencies estimate the complex dynamic stiffness of the system to identify their force coefficients. Curve fits of the physical model [Re(H) = ($K-\omega^2 M$, Im(H) = ($K_\perp+\omega C$)] estimate the structure, O-rings, and film force coefficients. The coefficient of determination (R^2) defines the goodness of fit between the physical model and the measurements for both curve fits [65] in the real and imaginary parts of $H_{XX,YY}$. R^2 is also defined as the ratio of the sum of squared regression SSR, divided over the total variation, SST:

$$R^2 = \frac{SSR}{SST} = \frac{\sum_{i=1}^{N}(y_i - f_i)^2}{\sum_{i=1}^{N}(y_i - \bar{y}_i)^2} \tag{C.5}$$

Where y_i denotes each measurement value of Re(H) and Im(H), from 1 to N frequency measurements, while $\bar{y}$ is the mean of the y_i measurements. Then, f_i is the physical model value corresponding in Re(H) and Im(H)to each y_i measurement. Coleman [66] presents the confidence bounds for the coefficients estimated by the curve fit of the physical model:

$$\psi_{fit} = \pm t_d \sqrt{S} \tag{C.6}$$

Where t_d is the inverse Student's t cumulative distribution function, given a 95% confidence level. S is a vector of the diagonal elements from the estimated covariance matrix of the coefficient

estimates, $(\mathbf{A}^{\mathrm{T}}\mathbf{A})^{-1}SSR^2$. Where the matrix **A** represents the Jacobian of the measured values in $\mathrm{Im}(H)_{XX,YY}$ and $\mathrm{Re}(H)_{XX,YY}$ with respect to the curve fits of the physical model, [$\mathrm{Re}(H) = (K-\omega^2 M)$ $\mathrm{Im}(H) = (C\omega + K_{\perp})$] The matrix $\mathbf{A}^{\mathrm{T}}$ is the transpose of **A**, and *SSR* is the sum of squared regression, as noted in Eq. C.5. Note ψ_{fit} are confidence intervals for the force coefficients as related to the precision uncertainty.

Measurement variability (U_V)

The measurement variability is related with the repeatability of measurements. The test sets have a standard deviation that demonstrates the variability in the measurements, hence producing confidence intervals [67]:

$$\psi_V = t_V S_V \tag{C.7}$$

Where t_V denotes the *t* Student's value for a single tail 95% confidence interval, and S_V is the standard deviation in the N=3 test sets:

$$S_x = \sqrt{\frac{1}{(N-1)}\sum_{i=1}^{N}(x_i - \overline{x})^2} \tag{C.8}$$

Where *x* represents the estimated force coefficients, $\overline{x}$, the average of all the measured data and *i* is the index number.

Uncertainty in dynamic force coefficients (*U*)

The total uncertainty for each parameter is the Euclidean norm of the measurement variability (U_V) and precision uncertainty (U_P). The ranges of uncertainty for the force coefficients follow from the repeated experimental results under a dry, dry +ORs and lubricated conditions using Eqs. (C6) to (C.8). Then, for each experimental condition, the ratio between uncertainty and its corresponding parameter delivers uncertainty magnitudes as a percentage. Finally, the average of the percentage uncertainties for each orbit radius renders the total uncertainty for the dry (unlubricated) system + ORs (U_{st+ORs}) and the lubricated system (U_L).

The experiments were performed a total of two times to assess variability. Table C1 shows two sets of identified force coefficients for the structure alone, Table C2 shows force coefficients for a dry (unlubricated) system with ORs installed and Table C3 for the lubricated system +ORs installed, all under the prescribed range of whirl amplitudes (r=0.05c to 0.45c)

Table C4 presents confidence intervals produced from the average force coefficients shown in Tables C1-C3 and Eqs. (C.5-C.8). First, Eqs. (C.5) and (C.6) produce confidence intervals related to precision uncertainty, then, Eqs.(C.7) and (C.8) produce confidence intervals reflecting the measurement variability. Finally, the Euclidean norm of both intervals equals to the total range of uncertainty, shown in Table C4.

Table C5 shows the total percentage uncertainty in the measurements as the ratio of the confidence intervals for each test condition to the nominal force coefficients shown in Tables C4. Next, the arithmetic mean of the confidence intervals for each condition is the total uncertainty in the force coefficients.

Table C1. Nominal force coefficients (*K, C, M)* identified by repeating experiments for dry (unlubricated) structure alone. Frequency range from 10 Hz to 130 Hz.

Condition	Test #	K_{XX} [MN/m]	K_{YY} [MN/m]	C_{XX} [kN-s/m]	C_{YY} [kN-s/m]	M_{XX} [kg]	M_{YY} [kg]
Structure alone, r=0.05c	1	6.2	6.3	0.2	0.3-	1.7	1.9
	2	5.5	5.9	0.3	0.2	0.9	0.5
	3	6.2	6.1	0.2	0.2	1.7	1.5
	Nominal	6.0		0.2		1.4	

Table C2. Nominal force coefficients (*K, C, M)* identified by repeating experiments for dry (unlubricated) + ORs system. Frequency range from 10 Hz to 130 Hz.

Orbit radius [*r/c*]	Test #	K_{XX} [MN/m]	K_{YY} [MN/m]	$K_{\perp XX}$ [MN/m]	$K_{\perp YY}$ [MN/m]	C_{XX} [kN-s/m]	C_{YY} [kN-s/m]
	1	16.8	17.3	3.5	3.2	3.8	2.7
r=0.05c	2	16.0	15.8	3.7	3.4	3.5	2.9
	Nominal	16.5		3.4		3.2	
	1	14.3	15.1	3.3	3.7	3.5	2.9
r=0.05c	2	14.2	14.7	3.7	3.6	2.9	3
	Nominal	14.5		3.5		3.0	
	1	13.1	12.8	3.3	3.3	2.1	1.8
r=0.15c	2	13.3	12	3.1	3.7	1.4	1.9
	Nominal	12.6		3.3		1.6	
	1	12.1	11.8	2.4	2.8	1.4	1.9
r=0.20c	2	11.5	12.2	2.4	2.4	1.2	1.6
	Nominal	11.9		2.5		1.5	
	1	11.1	10.8	2.5	2.3	1	1.1
r=0.25c	2	11.5	11	2.4	2.2	0.8	1.2
	Nominal	11.1		2.3		1.0	
	1	10.5	10.1	2	2	0.9	0.9
r=0.30c	2	11.2	11.5	2.4	2.2	1.0	1.2
	Nominal	10.8		2.1		1.0	
	1	9.7	10.1	1.8	1.8	0.7	0.8
r=0.35c	2	9.6	10.2	2	1.6	0.6	0.8
	Nominal	9.9		1.8		0.7	
	1	9.3	9.7	1.6	1.6	0.6	0.7
r=0.40c	2	9.5	9.9	1.5	1.7	0.8	0.9
	Nominal	9.6		1.6		0.7	
	1	9.1	9.5	1.6	1.5	0.6	0.6
r=0.45c	2	9.5	9.8	1.6	1.3	0.5	0.7
	Nominal	9.4		1.5		0.6	

Table C3. Nominal force coefficients (*K, C, M)* identified by repeating experiments for lubricated system. Frequency range from 10 Hz to 40 Hz.

Orbit radius [*r/c*]	Test #	C_{XX} [kN-s /m]	C_{YY} [kN-s/m]	M_{XX} [kg]	M_{YY} [kg]
	1	29.4	28.8	57.6	54.4
r=0.05*c*	2	29.8	30.2	62.0	59.0
	Nominal	29.5		58.2	
	1	29.0	28.7	58.0	56.5
r=0.10*c*	2	31.0	30.9	57.0	51.0
	Nominal	29.9		55.6	
	1	28.9	27.9	54.0	52.5
r=0.15*c*	2	29.0	25.5	50.0	58.0
	Nominal	27.8		53.6	
	1	29.9	28.9	56.2	51.8
r=0.20*c*	2	31.0	31.2	53.0	56.4
	Nominal	30.2		54.3	
	1	28.3	27.7	55.1	50.7
r=0.25*c*	2	28.5	29.3	58.4	47.4
	Nominal	28.4		52.9	
	1	27.2	25.1	47.1	43.2
r=0.30*c*	2	26.9	24.8	49.2	47.4
	Nominal	26.6		46.7	
	1	22.1	20.3	49.2	42.3
r=0.35*c*	2	23.0	25.1	40.2	34.2
	Nominal	22.6		41.5	
	1	23.2	21.2	34.3	30.6
r=0.40*c*	2	21.5	22.7	37.5	34.2
	Nominal	22.1		34.1	
	1	21.7	20.6	18.7	15.3
r=0.45*c*	2	23.5	22.0	20.3	17.0
	Nominal	21.9		17.8	

Table C4. Nominal force coefficients (*K, C, M*) and confidence intervals. Intervals produced for dry (unlubricated), dry + ORs and lubricated systems.

Condition	Orbit radius [*r/c*]	*K* [MN/m]	$K_{\perp}$ [MN/m]	*C* [kN-s/m]	*M* [kg]
Structure alone	*r*=0.05*c*	6.0 ± 0.3	N/A	0.2 ± 0.1	1.4 ± 0.6
Unlubricated + ORs	*r*=0.05*c*	16.5 ± 1.1	3.4 ± 0.3	3.2 ± 0.4	N/A
	r=0.10*c*	14.5 ± 0.9	3.5 ± 0.2	3.0 ± 0.4	
	r=0.15*c*	12.6 ± 1.3	3.3 ± 0.4	1.6 ± 0.3	
	r=0.20*c*	11.9 ± 0.8	2.5 ± 0.4	1.5 ± 0.3	
	r=0.25*c*	11.1 ± 0.4	2.3 ± 0.2	1.0 ± 0.2	
	r=0.30*c*	10.8 ± 1.8	2.1 ± 0.3	1.0 ± 0.2	
	r=0.35*c*	9.9 ± 0.8	1.8 ± 0.2	0.7 ± 0.1	
	r=0.40*c*	9.6 ± 0.7	1.6 ± 0.1	0.7 ± 0.1	
	r=0.45*c*	9.4 ± 0.6	1.5 ± 0.1	0.6 ± 0.1	
Lubricated system (ORs installed)	*r*=0.05*c*	N/A		29.2 ± 2.2	57.4 ± 6.1
	r=0.10*c*			29.4 ± 2.2	58.2 ± 6.3
	r=0.15*c*			28.0 ± 2.2	60.0 ± 6.0
	r=0.20*c*			29.4 ± 2.2	54.0 ± 6.1
	r=0.25*c*			27.6 ± 1.9	53.0 ± 5.3
	r=0.30*c*			26.5 ± 1.9	45.4 ± 5.0
	r=0.35*c*			22.9 ± 2.7	41.5 ± 4.8
	r=0.40*c*			22.2 ± 2.2	32.3 ± 4.2
	r=0.45*c*			21.6 ± 2.8	18.5 ± 2.9

Table C5. Total uncertainty (%) of dynamic force coefficients. Confidence intervals produced for dry (unlubricated), dry + ORs and lubricated systems.

Condition	Orbit radius [*r*/*c*]	*K*	$K_{\perp}$	*C*	*M*
Structure alone	r=0.05c	**5.0 %**	N/A	**50.0 %**	**42.5 %**
Unlubricated + ORs	r=0.05c	6.7%	8.8%	12.5%	N/A
	r=0.10c	6.2%	5.7%	13.3%	
	r=0.15c	10.3%	12.1%	18.8%	
	r=0.20c	6.7%	16.0%	20.0%	
	r=0.25c	3.6%	8.7%	20.0%	
	r=0.30c	16.7%	14.3%	20.0%	
	r=0.35c	8.1%	11.1%	14.3%	
	r=0.40c	7.3%	6.3%	14.3%	
	r=0.45c	6.4%	6.7%	16.7%	
	Average uncertainty	**7.2%**	**10.0%**	**16.6%**	
Lubricated system (ORs installed)	r=0.05c	N/A		6.4%	10.5%
	r=0.10c			7.4%	11.2%
	r=0.15c			7.9%	12.1%
	r=0.20c			5.3%	10.1%
	r=0.25c			4.2%	11.7%
	r=0.30c			6.9%	9.9%
	r=0.35c			13.3%	13.3%
	r=0.40c			8.6%	9.1%
	r=0.45c			12.3%	12.4%
	Average uncertainty			**8.0%**	**11.1%**

Uncertainty in static load measurements

The identification of static stiffness coefficients of the dry (unlubricated) test structure involves a series of static loads imposed by the hydraulic piston between the reference axes *X* and *Y*. The static loader pulls the BC relative to the fixed journal, and the orthogonally positioned eddy current sensors identify the BC displacement at (20) discrete load points. The load and displacement

sensors are recorded manually, and a linear regression curve fit identifies the static load coefficients with and without ORs installed. Since the measurements are recorded manually, the bias uncertainty is disregarded.

Three sets of measurements to the test structure without seals installed identify the uncertainty due to variability (U_V). Table C6 shows the structure identified static stiffness coefficients ($K_{st,static}$), estimated over a load range from 0 – 900 N.

Table C6. Identified test structure static stiffness coefficient ($K_{st,static}$) without ORs installed. Static loads range from 0 N to 900 N.

Test #	$K_{st,static}$ [MN/m]
1	6.4
2	6.6
3	6.8

Eqs. C.8 and C.8 establish the uncertainty in the static stiffness coefficients:

$$U_{K_{static}} = \frac{\psi_{K_{static}}}{K_{static}} = 3.6\% \tag{C.9}$$

Total Uncertainty in force coefficients

Table C7 summarizes the uncertainty in the force coefficients. Note the uncertainty in the dynamic force coefficients, specifically for the structure + ORs and the lubricated system, is the arithmetic mean of the confidence intervals reported Table C5.

Table C7. Total uncertainty in static and dynamic force coefficients.

Condition	U_K	$U_{K\perp}$	U_C	U_M
Structure alone (U_{st})	5.0 %	N/A	50.0 %	42.5 %
Structure + ORs (U_{st+OR})	7.2%	10.0%	16.6%	N/A
Lubricated (U_L)	N/A		8.0%	11.1%
Static (U_{static})	3.6%		N/A	

APPENDIX D

CROSS-COUPLED COMPLEX DYNAMIC STIFFNESSES

Figures D1 and D2 show the real and imaginary parts of the cross-coupled dynamic complex stiffnesses $(H_{st+OR})_{XY,YX}$ for dynamic load test with a dry (unlubricated) system and ORs installed. Figure D1 (a) shows contour plots of $\mathrm{Re}(H_{st+OR})_{XY,YX}$ vs. whirl frequency and (b) $\mathrm{Re}(H_{st+OR})_{XY,YX,}$ vs. squeeze velocity (v_s) and orbit radius (r/c). Similarly, D2 (a) shows a contour plot of $\mathrm{Im}(H_{st+OR})_{XY,YX}$ vs. ω and (b) $\mathrm{Im}(H_{st+OR})_{XY,YX}$ vs. v_s and r/c. The magnitudes of $(H_{st+OR})_{XY,YX}$ span a frequency range over 10 to 130 Hz and whirl orbit radii from r/c = 0.05, 0.10, …, to 0.45. Both the real and imaginary parts of the cross-coupled complex stiffnesses depicted in Figs. D1 and D2 represent a fraction of their direct counter parts. Moreover, the measurements tend to a nil magnitude, that is $(H_{st+OR})_{XY,YX} \rightarrow 0$ (both real and imaginary), as the orbit radius increases and remain mostly constant as the whirl frequency grows. However, the measurements at the smallest orbit radii. span magnitudes down to -0.5 MN/m, which is at least an order of magnitude lower than their corresponding direct parts.

Figures D3 and D4 show the real and imaginary parts of the cross-coupled dynamic complex stiffnesses $(H_L)_{XY,YX}$ obtained from dynamic loads with a lubricated system and ORs installed. Figure D3 shows (a) contour plots of $\mathrm{Re}(H_L)_{XY,YX}$ vs. ω and (b) $\mathrm{Re}(H_L)_{XY,YX}$ vs. ω and r/c. Figure D4 shows the cross-coupled magnitudes of $\mathrm{Im}(H_L)$ in the form of (a) contour plots and (b) three-dimensional plots shown against v_s and r/c. The measurements in Fig. D3 and D4 span a whirl frequency range ω = 10 to 70 Hz and orbit radii from r/c = 0.05 to 0.45. Similarly to $(H_{st+OR})_{XY,YX}$, there is a significant difference between the direct and cross-coupled parts of $\mathbf{H}_L$, as most of the largest magnitudes of $(H_L)_{XY,YX}$ amount to nearly 1 MN/m, nearly ten times lower than $(H_L)_{XY,YX}$. Additionally, Figures D5 and D6 present cross-coupled magnitudes of $\mathrm{Re}(H_L)_{XY,YX}$ and $\mathrm{Im}(H_L)_{XY,YX}$ along with the physical model [$\mathrm{Re}(H_L)=K-\omega^2 M$ and $\mathrm{Im}(H_L)= \omega C$], and the correlation factor R^2.

However, as it is expected, the measurements in D5 and D6 mostly depict a poor fit to the physical model, that is R^2<<0.90.

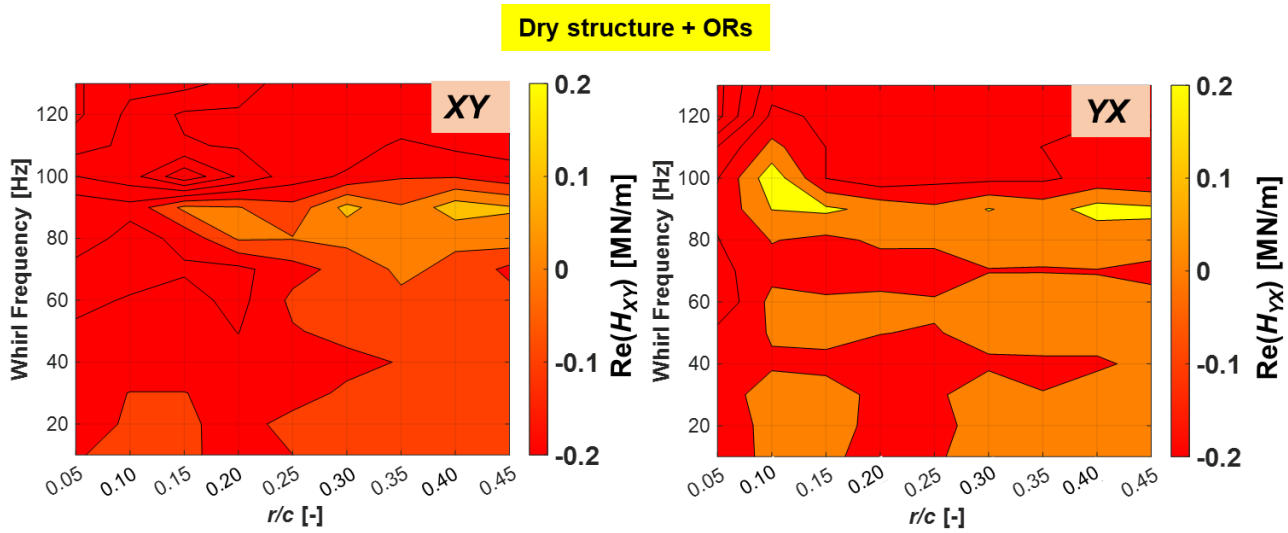

(a) Re(H_{st+OR})$_{XY,YX}$ vs. orbit radius (r/c) and whirl frequency (ω)

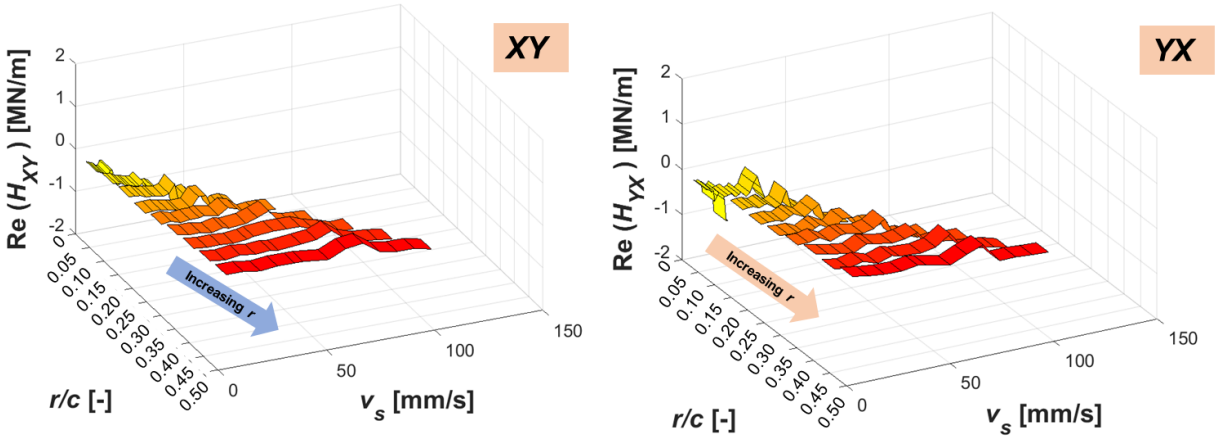

(b) Re(H_{st+OR})$_{XY,YX}$ vs. orbit radius (r/c) and squeeze velocity (v_s)

Figure D1. Dry structure + ORs. (a) Contour plots of (H_{st+OR})$_{XY,YX}$ vs. whirl frequency (ω) and orbit radius (r/c). (b) Re(H_{st+OR})$_{XY,YX}$ vs. squeeze velocity (v_s) and r/c. CCOs with radius r = 0.05c to 0.45c. Frequency range ω = 10 Hz to 130 Hz. P_S=0.0 bar(g).

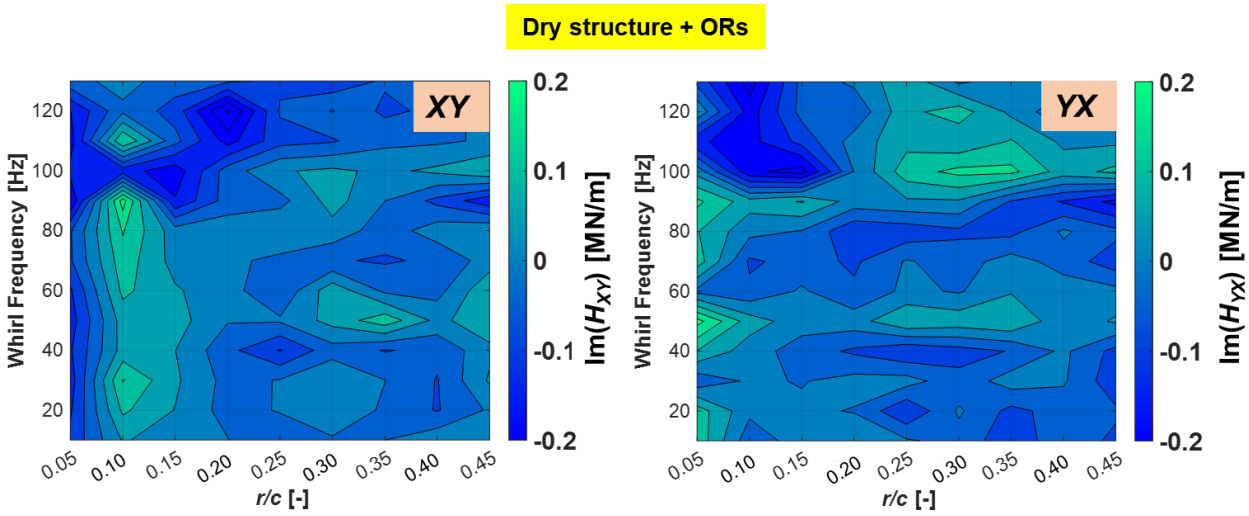

(a) Im(H_{st+OR})$_{XY,YX}$ vs. orbit radius (r/c) and whirl frequency (ω)

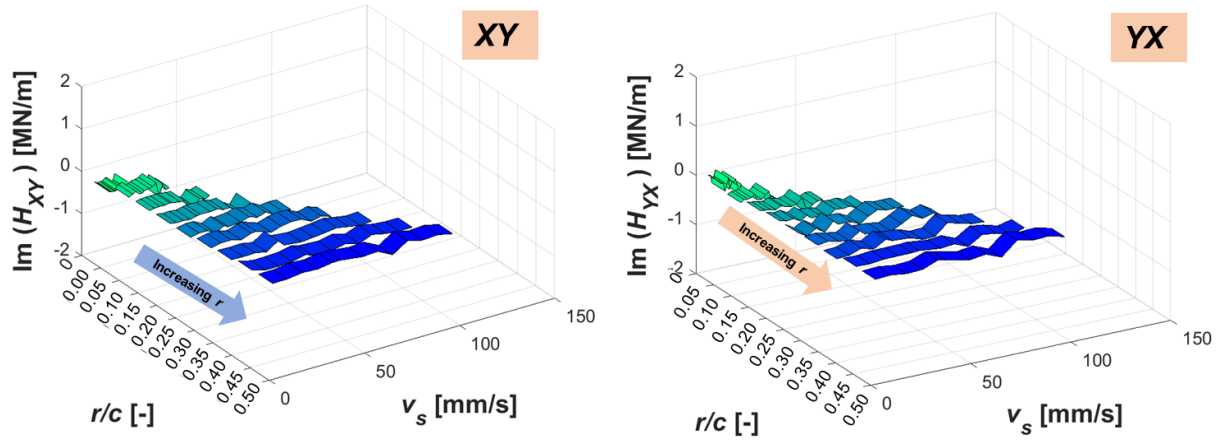

(c) Im(H_{st+OR})$_{XY,YX}$ vs. orbit radius (r/c) and squeeze velocity (v_s)

Figure D2. Dry structure + ORs. (a) Contour plots of (H_{st+OR})$_{XY,YX}$ vs. whirl frequency (ω) and orbit radius (r/c). (b) Im(H_{st+OR})$_{XY,YX}$, vs. squeeze velocity (v_s) and r/c. CCOs with radius r = 0.05c to 0.45c. Frequency range ω = 10 Hz to 130 Hz. P_S=0.0 bar(g).

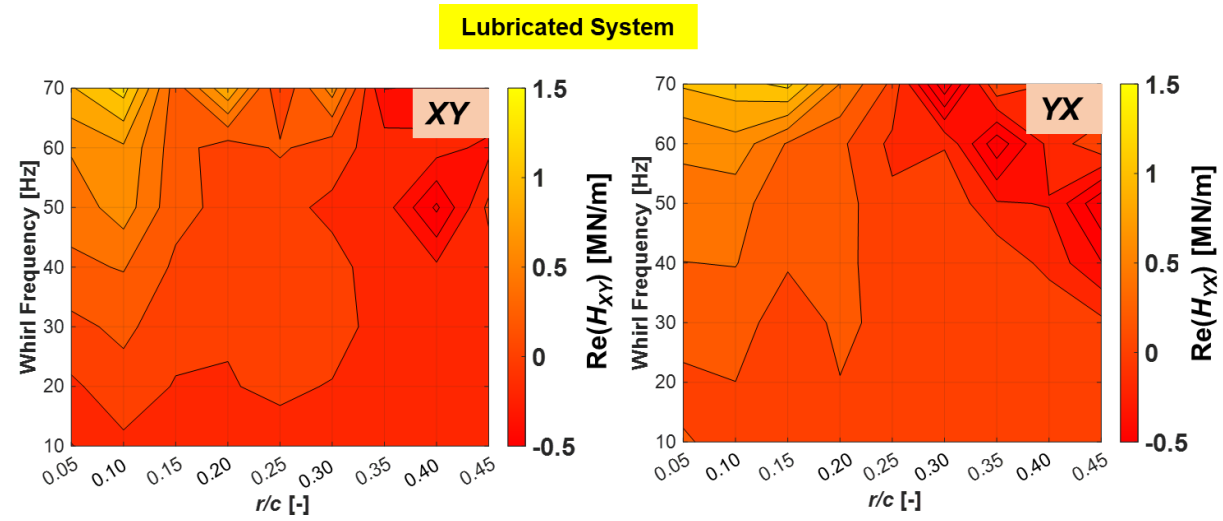

(a) Re(H_L)$_{XY,YX}$ vs. orbit radius (r/c) and whirl frequency (ω)

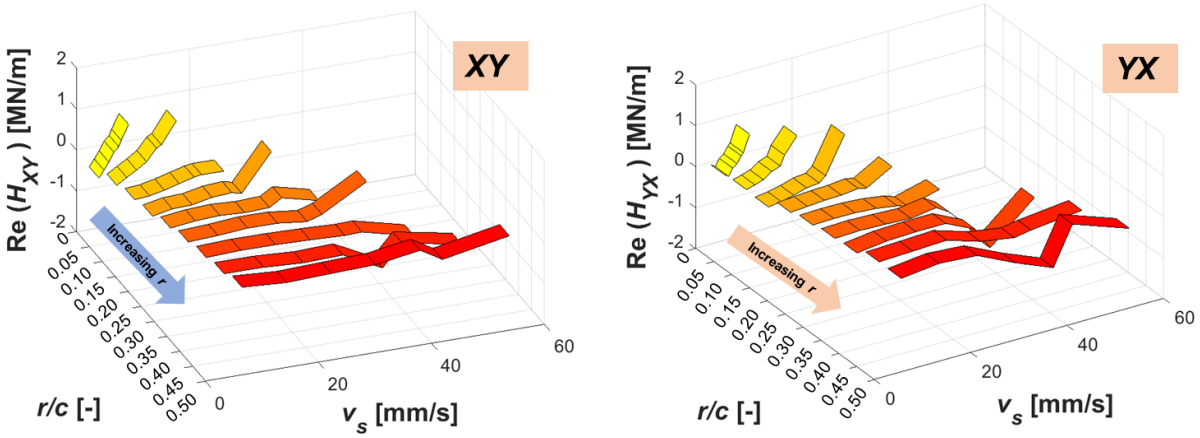

(b) Re (H_L) $_{XY,YX}$ vs. orbit radius (r/c) and squeeze velocity (v_s)

Figure D3. Lubricated structure + ORs. (a) Contour plots of (H_L)$_{XY,YX}$ vs. whirl frequency (ω) and orbit radius (r/c). (b) Re(H_L)$_{XY,YX}$ vs. squeeze velocity (v_s) and r/c. CCOs with radius r = 0.05c to 0.45c. Frequency range ω = 10 Hz to 70 Hz. P_S=0.69 bar(g).

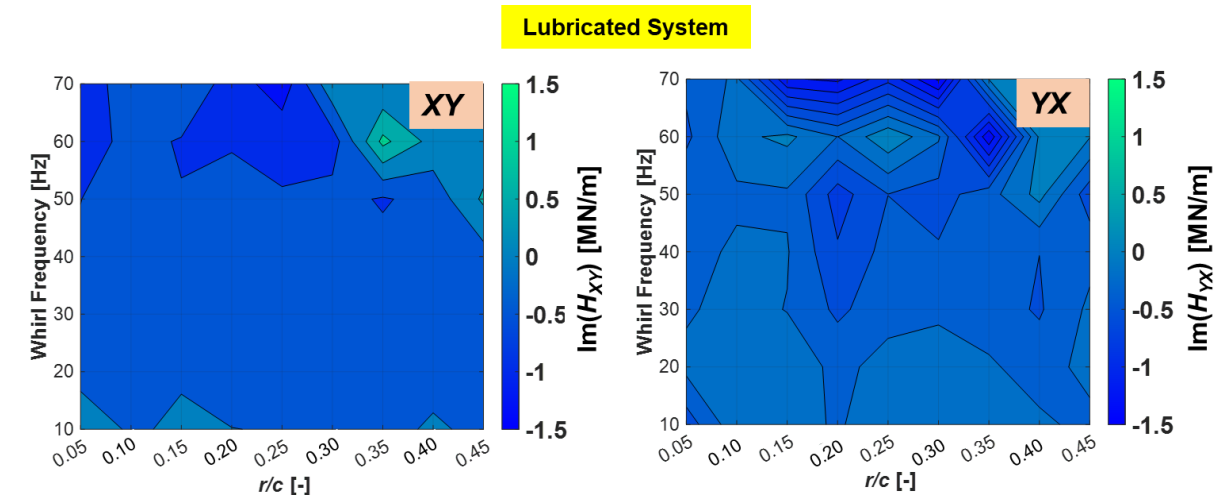

(a) Im(H_L)$_{XY,YX}$ vs. orbit radius (r/c) and whirl frequency (ω)

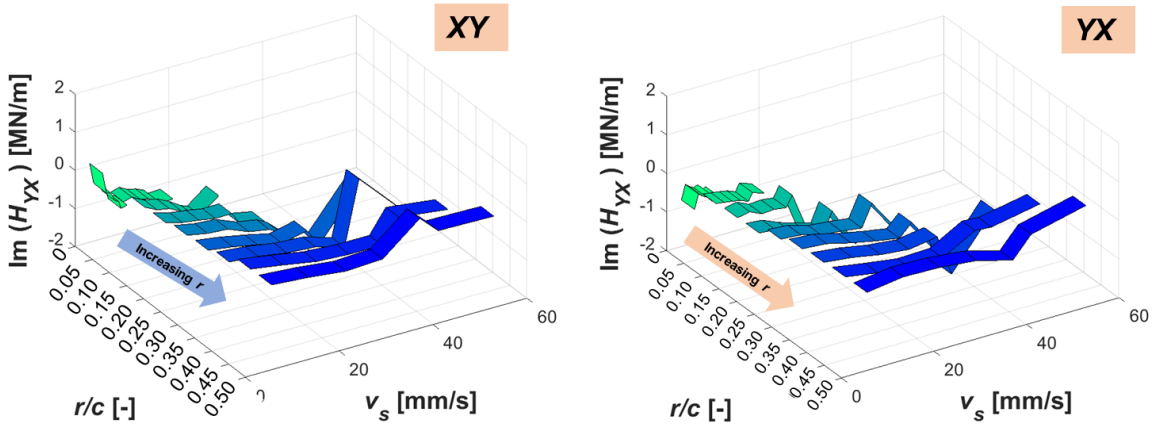

(b) Im(H_L)$_{XY,YX}$ vs. orbit radius (r/c) and squeeze velocity (v_s)

Figure D4. Lubricated structure + ORs. (a) Contour plots of (H_L)$_{XY,YX}$ vs. whirl frequency (ω) and orbit radius (r/c). (b) Im(H_L)$_{XY,YX}$ vs. squeeze velocity (v_s) and r/c. CCOs with radius r = 0.05c to 0.45c. Frequency range ω = 10 Hz to 70 Hz. P_S=0.69 bar(g)

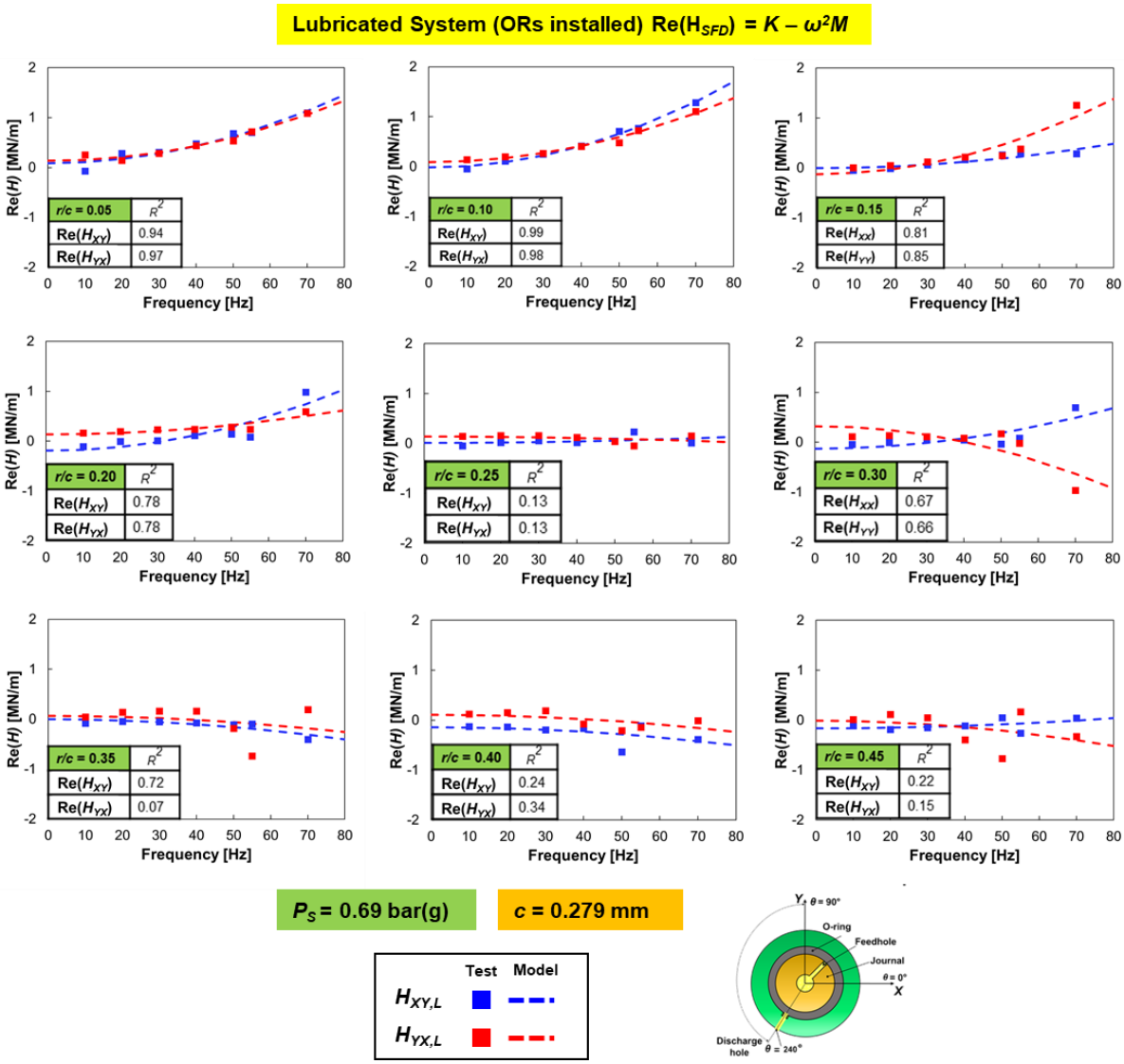

Figure D5. Lubricated system. Real parts of system cross-coupled complex dynamic stiffnesses vs. whirl frequency. CCOs with radius $r = 0.05c$ to $0.45c$. Frequency range ω =10 Hz to 70 Hz.

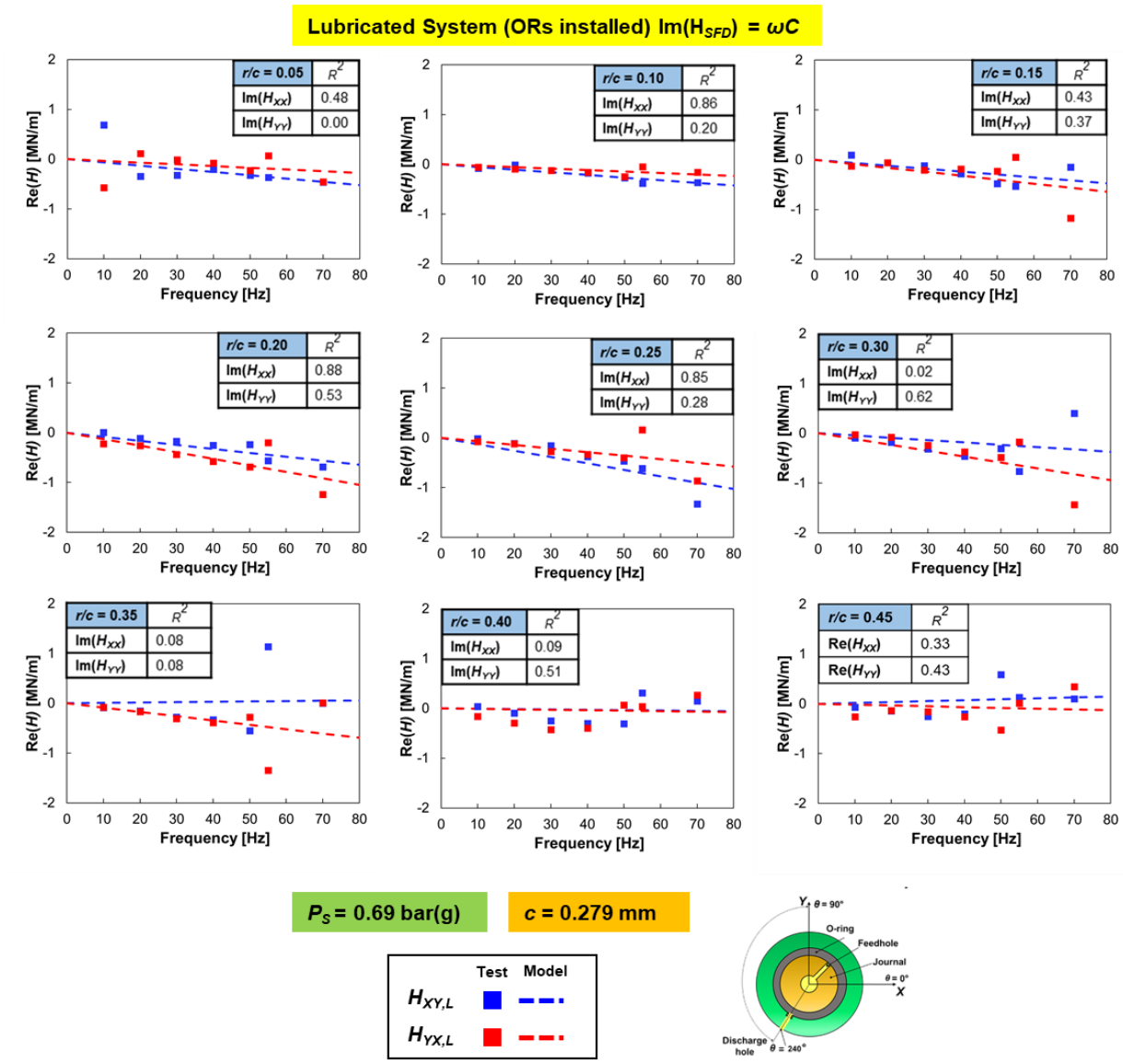

Figure D6. Lubricated system. Imaginary parts of system cross-coupled complex dynamic stiffnesses vs. whirl frequency. CCOs with radius r = 0.05c to 0.45c and static eccentricity e_s/c = 0.0. Frequency range over 10 Hz to 70 Hz.

APPENDIX E

STATIC LOAD MEASUREMENTS TO IDENTIFY O-RINGS STIFFNESSES

This section presents an assessment of the OR reaction forces and BC tilt to determine that it is valid to assume that each elastomeric seal (top and bottom) have equal force coefficients. A series of static load measurements follow with only the top or bottom ring installed at a time. Figure E1 presents a schematic cross section view of the SFD test rig depicting measurement locations for static load tests with a displacement idealization diagram to estimate bearing cartridge (BC) displacement at different axial locations. A pneumatic piston applies a static load F by pulling the BC along the film lands middle plane, 45^o away from the BC orthogonal axes X and Y. Two orthogonally positioned eddy current sensors measure BC displacements due to static loads (x_0), and relative to the journal along its midplane. For this analysis, the journal midplane denotes the start of the local coordinate z_0=0. Simultaneously, another pair of eddy current sensors, atop the first pair (z_1=53.3 mm), measure the BC displacement (x_1) in that location.

Five sets of static load measurements in the load range from 0 to ~1000 N (230 lbf) determine the BC relative displacement at the two axial locations (z_0=0, z_1=53.3 mm). The experiments include static loads with the structure alone (no ORs), with the rig with two O-rings (two ORs) installed, and two experiments with only one OR installed, top (TOP OR) and bottom (BTM OR). Note the O-rings used are the same as the ones employed in Chapters VI-IX.

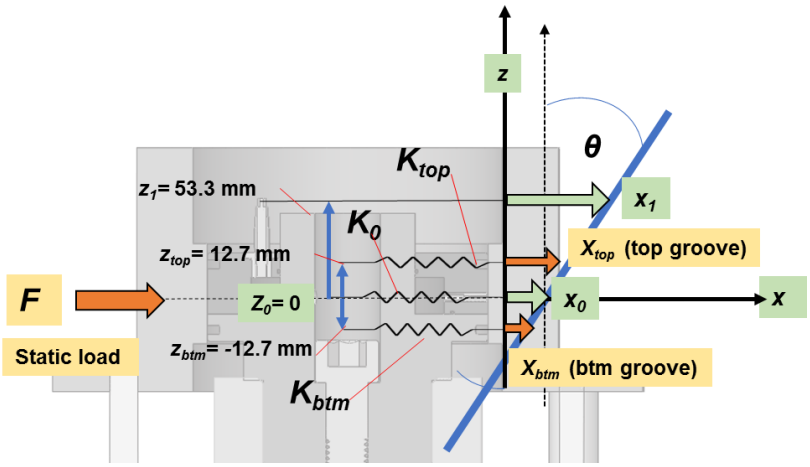

Figure E1. Idealization of BC displacement to a static load.

Figure E2 shows displacement measurements at four end seal conditions, and two axial locations x_0 and x_1. Linear regression curve fits to the measurements identify equivalent static stiffness coefficients with either one or two seals installed, as well as a rig structural stiffness coefficient ($K_{st,static}$) identified with no ORs in place.

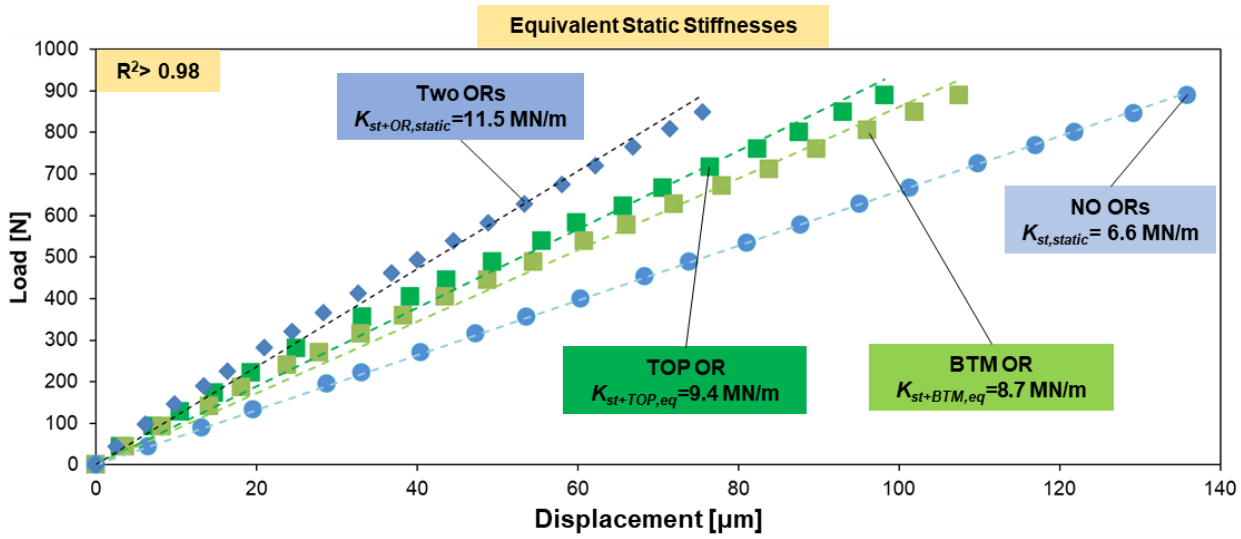

Figure E2. Measurements of displacement versus static load. Test conditions include: no ORs, top OR, bottom OR, and two ORs installed. Displacements measured at z_0 and z_1

Measurements of x_1 and x_0 with one OR installed estimate x_{btm} and x_{top} at the bottom and top journal ring groove locations, z_{btm} and z_{top}, respectively. Assuming a linear displacement of the BC:

$$x_{top} = x_0 + \delta_{top} z_{top} \quad ; x_{btm} = x_0 + \delta_{btm} z_{btm} \quad ; z_{btm} < 0 < z_{top} \tag{E.1}$$

where δ is the BC tilt. The relative displacement constant a relates δ with x_0, given z_1=53.3 mm and the BC relative displacement x_1 (see Fig. E1).

$$\delta = \frac{(x_1 - x_0)}{z_1} \cong \frac{x_0}{a} \tag{E.2}$$

Note, in a linear displacement range, a is the inverse of the slope of δ/x_0. Since the rate δ/x_0 is assumed constant, x_{top} and x_{btm} follow:

$$x_{top} = x_0\left(1+\frac{z_{top}}{a}\right); \quad x_{btm} = x_0\left(1+\frac{z_{btm}}{a}\right) \tag{E.3}$$

Figure E3 displays magnitudes of δ vs. x_0 for load measurements with a single OR installed. Figure E3 shows δ vs. x_0 increase at a constant rate, and thus x_{top} and x_{btm} become linear functions of x_0, z_1 and a.

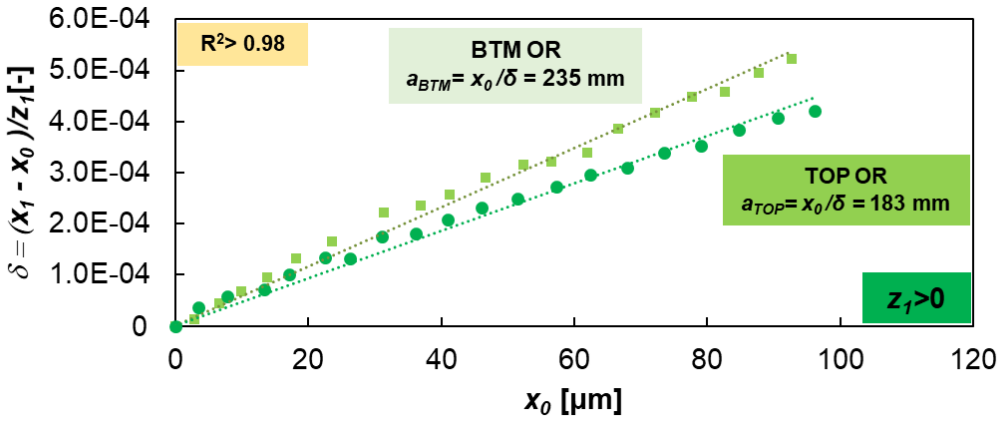

Figure E3. Static load measurements with one OR installed. $\delta = (x_1-x_0)/z_1$ versus x_0

The equivalent stiffnesses $K_{st+TOP,eq}$, $K_{st+BTM,eq}$ with either the top or bottom O-ring using strain energy relationships are:

$$K_{st+TOP,eq} = K_{st} + K_{TOP,OR}\left(1+\frac{z_{top}}{a}\right)^2;\ K_{st+BTM,eq} = K_{st} + K_{BTM,OR}\left(1+\frac{z_{btm}}{a}\right)^2 \quad \text{(E.4)}$$

Where $K_{TOP,OR}$ and $K_{BTM,OR}$ are OR static stiffness coefficients. Similarly, an equivalent stiffness coefficient including both rings ($K_{2ORs,eq}$) is:

$$K_{2ORs,eq} = K_{st,static} + K_{TOP,OR}\left(1+\frac{z_{top}}{a}\right)^2 + K_{BTM,OR}\left(1+\frac{z_{btm}}{a}\right)^2 \quad \text{(E.5)}$$

Table E1 shows the identified static stiffness coefficients: top and bottom OR coefficients ($K_{TOP,OR}$, $K_{BTM,OR}$) using Eqs. E.3-E.5 and the test structure stiffness coefficient ($K_{st,static}$) from curve fits to measurements of load versus displacement, as seen in Fig. E2. Additionally, Table 1 shows the magnitude of ($K_{eq,2ORs}$=11.5MN/m) using Eq. E.5. Note $K_{st+OR,static}$= 11.5 MN/m refers to the OR + structure static stiffness identified with two O-rings in place, and by measuring the BC displacement at z=0

The measurements with a single OR installed, along with strain-energy relationships show the static stiffness coefficient for the individual ORs are nearly equal. Hence, each OR produces virtually an identical stiffness. Additionally, note the displacement measurements show the order of magnitude of δ~5x10^{-4}, shown in Fig. E3 is so small, that the BC tilt may be disregarded. Hence showing it is valid to assume the test system is a 2DOF mechanical system and the loads applied to it are evenly distributed between the two ORs.

Table E1. Estimated OR stiffnesses obtained from curve fits to static load tests and strain energy relationships. Parameters identified from static load tests with one and no ORs installed.

$K_{st,static}$ [MN/m]	6.6	
1 OR		
	BTM	TOP
$a=x_0/\delta$ [mm]	183	235
$K_{st+TOP,eq}$, $K_{st+BTM,eq}$ [MN/m]	8.7	9.4
$K_{TOP,OR}$, $K_{BTM,OR}$ [MN/m]	2.5	2.4
2 ORs		
$K_{st+OR,static}$ (static loads, 2 ORs installed) [MN/m]	11.5	
$K_{2ORs,eq}$ (single OR static loads, Eqs. E1-E3) [MN/m]	11.5	

APPENDIX F

FLOW MEASUREMENTS IN O-RINGS SEALED AND OPEN ENDS SFD

Figure F1 displays measurements of the lubricant flow rate (Q_S) vs. supply pressure (P_S) into the ORs sealed damper and open to ambient (no ORs) measured under a static condition. The oil enters through a feedhole in the journal located at θ = 45° and at the midplane of the journal (z = 0). A flow meter records $Q_{S.,}$ from 0.05 to ~2 lpm with an accuracy of $\pm$3% within the full range (0.05-4.5 lpm) [68].

The measurements are recorded under a static condition and the ORs perfectly seal the journal ends, thus, no lubricant side leakage is observed. Incidentally, Fig. F1 shows that the open-ended damper requires substantially larger lubricant flow rates than the sealed damper as the supply pressure increases. For instance, the sealed damper shows a lubricant flow rate Q_S = 2.5 lpm and supply pressure P_S =3.5 bar(g), however, the open ends damper lubricant flowrate is 1.8 times larger (Q_S =4.5 lpm) for P_S=3.5 bar(g). Thus showing a substantial increase in flow resistance when installing the ORs. The flow measurements not only serve to identify the large difference in lubricant flow rate between a sealed and open ends damper to reach a certain supply pressure but are also useful to verify the ORs adequately seal the damper under a static condition. That is, for the range of lubricant supply pressures P_S= 0.0 – 5.8 bar(g) depicted in Fig. F1, the ORs do not allow for lubricant side leakage from the damper film land (through the ORs).

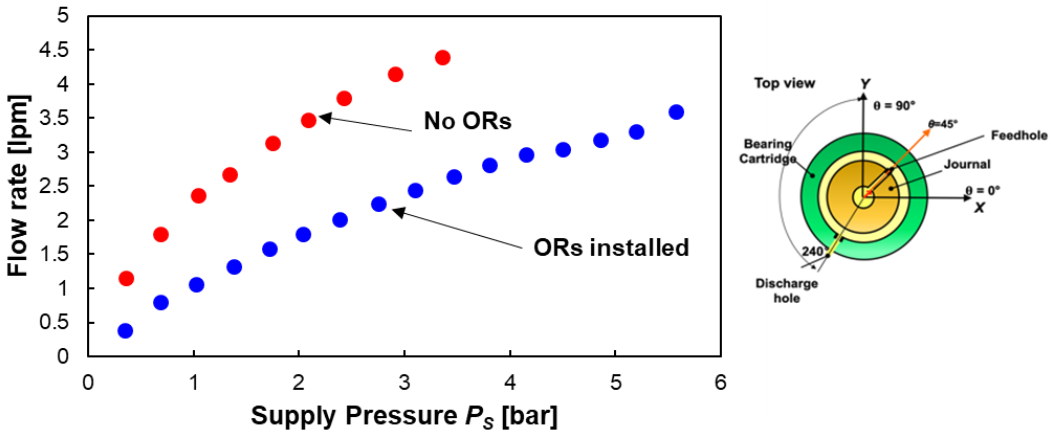

Figure F1. Lubricant flowrate (Q_S) vs. inlet supply pressure (P_S) for ORs sealed and open ends damper. Lubricant inlet through feedhole at θ = 45° at mid-plane, z = 0, and lubricant discharge through hole (θ = 240° and z =1/4L).